

DEVELOPMENT OF A TSUNAMI FORECAST MODEL FOR HALEIWA, HAWAII (DRAFT)

Yong Wei

September, 2013

Abstract

As part of NOAA's tsunami forecast system, this study addresses the development, validation, and stability tests of a tsunami forecast model for Haleiwa, Hawaii based on the Method of Splitting Tsunami (MOST). The ocean scale modeling is provided by an A grid covering Hawaiian Islands at a grid resolution of two arc min ($\sim 3,700$ m). The near-shore tsunami dynamics is computed in a B grid covering the Island of Oahu at a grid resolution of 18 arc sec (~ 540 m). The tsunami inundation is computed in a C grid employing a mixture of three different grid resolutions: 1 arc sec (~ 30 m), 2/3 arc sec (~ 20 m) and 1/3 arc sec (~ 10 m), where the latter two mainly focus on the Haleiwa Harbor. This setup requires more CPU time (~ 20 min) than a to complete 4-hour simulation of wave inundation onto dry land. In this study, a reference inundation model is also developed using finer grids than the forecast model at all levels. In particular, the reference model uses a grid resolution of 1/3 arc sec throughout the entire C grid to provide model references for the forecast models. The developed models are evaluated using three historical tsunami events: June 10, 1996 Andreanov, October 28, 2012 haida Gwaii, and February 6, 2013 Solomon Islands. The model validation shows good agreement between model results and observations at the Haleiwa tide station. Model stability is further evaluated based on 21 synthetic scenarios generated in the major subduction zones around the Pacific Rim at magnitudes of M_w 9.3, M_w 7.5 and M_w 6.4. The results obtained from forecast and reference models are agreeable with an average error of 12% for the maximum wave amplitude at the tide gage location.

1. Background and Objectives

The National Oceanic and Atmospheric Administration (NOAA) Center for Tsunami, Research (NCTR) at the NOAA Pacific Marine Environmental Laboratory (PMEL) has developed a tsunami forecasting capability for operational use by NOAA's two Tsunami Warning Centers located in Hawaii and Alaska (Titov *et al.*, 2005a). The system is designed to efficiently provide basin-wide warning of approaching tsunami waves accurately and quickly. The system, termed Short-term Inundation Forecast of Tsunamis (SIFT), combines real-time tsunami event data with numerical models to produce estimates of tsunami wave arrival times and amplitudes at a coastal community of interest. The SIFT system integrates several key components: deep-ocean observations of tsunamis in real time, a basin-wide pre-computed propagation database of water level and flow velocities based on potential seismic unit sources, an inversion algorithm to refine the tsunami source based on deep-ocean observations during an event, and high-resolution tsunami forecast models.

The objective of this present work is to develop an operational forecast model to be used in near real time to protect the community of Haleiwa, Hawaii, from the potential impact posed by a tsunami. Haleiwa is a small tourist town located on the northshore of the Island of Oahu, Hawaii. According to Census 2010, the total population in Haleiwa is 3,970, an increase of 1,745 from 2,225 in Census 2000. In 1984, Haleiwa became a State Historic, Culture and Scenic District in Hawaii. The town has a small harbor and boat ramp as well as low lying area particularly near the Anahulu stream which empties into Pacific near the marina. The north shore of Oahu is world renown for surfing and Haleiwa caters to this attraction, as well as numerous beaches and year-round pleasant weather. There are about 20,000 permanent residents along the north shore and an estimated 2.4 million visitors each year. The historical records show that Haleiwa is vulnerable to major tsunamis generated from the Pacific Rim, especially in the subduction zones of Aleutian-Alaska, Kuril-Kamchatka, and Peru-Chile (Table 1). The development of a tsunami forecast model is an urgent need in Haleiwa, Hawaii for more effective and efficient warning and protection from catastrophic tsunami in the future.

2. Forecast Methodology

A high-resolution inundation model was used as the basis for development of a tsunami forecast model to operationally provide an estimate of wave arrival time, wave height, and inundation at Haleiwa, Hawaii following tsunami generation. All tsunami forecast models are run in real time while a tsunami is propagating across the open ocean. The Haleiwa model was designed and tested to perform under stringent time constraints given that time is generally the single limiting factor in saving lives and property. The goal of this work is to maximize the length of time that the community of Haleiwa has to react to a tsunami threat by providing accurate information quickly to emergency managers and other officials responsible for the community and infrastructure.

The general tsunami forecast model, based on the Method of Splitting Tsunami (MOST), is used in the tsunami inundation and forecasting system to provide real-time tsunami forecasts at selected coastal communities. The model runs in minutes while employing high-resolution grids constructed by the National Geophysical Data Center (NGDC). MOST is a suite of numerical simulation codes capable of simulating three processes of tsunami evolution: earthquake, transoceanic propagation, and inundation of dry land. The MOST model has been extensively tested against a number of laboratory experiments and benchmarks (Synolakis *et al.*, 2008) and was successfully used for simulations of many historical tsunami events. The main objective of a forecast model is to provide an accurate, yet rapid, estimate of wave arrival time, wave height, and inundation in the minutes following a tsunami event. Titov and González (1997) describe the technical aspects of forecast model development, stability, testing, and robustness, and Tang *et al.* (2009) provide detailed forecast methodology.

A basin-wide database of pre-computed water elevations and flow velocities for unit sources covering worldwide subduction zones has been generated to expedite forecasts (Gica *et al.*, 2008). As the tsunami wave propagates across the ocean and successively reaches tsunami meter observation sites, recorded sea level is ingested into the tsunami forecast application in near real-time and incorporated into an inversion algorithm to

produce an improved estimate of the tsunami source. A linear combination of the pre-computed database is then performed based on this tsunami source, reflecting the transfer of energy to the fluid body, to produce synthetic boundary conditions of water elevation and flow velocities to initiate the forecast model computation.

Accurate forecasting of the tsunami impact on a coastal community largely relies on the accuracies of bathymetry and topography and the numerical computation. The high spatial and temporal grid resolution necessary for modeling accuracy poses a challenge in the run-time requirement for real-time forecasts. Each forecast model consists of three telescoped grids with increasing spatial resolution in the finest grid, and temporal resolution for simulation of wave inundation onto dry land. The forecast model utilizes the most recent bathymetry and topography available to reproduce the correct wave dynamics during the inundation computation. Forecast models, including the Haleiwa model, are constructed for at-risk populous coastal communities in the Pacific and Atlantic Oceans. Previous and present development of forecast models in the Pacific (Titov *et al.*, 2005a; Titov, 2009; Tang *et al.*, 2008; Wei *et al.*, 2008; Tang *et al.*, 2012; Wei *et al.*, 2013) have validated the accuracy and efficiency of each forecast model currently implemented in the real-time tsunami forecast system. Models are tested when the opportunity arises and are used for scientific research.

3. Model development

The general methodology for modeling at-risk coastal communities is to develop a set of three nested grids, referred to as A, B, and C-grids, each of which becomes successively finer in resolution as they telescope into the population and economic center of the community of interest. The offshore area is covered by the largest, yet lowest resolution, A-grid while the near-shore details are resolved within the finest scale C-grid to the point that tide gauge observations recorded during historical tsunamis are resolved within expected accuracy limits. The procedure is to begin development with large spatial extent merged bathymetric and topographic grids at high resolution, and then optimize these grids by sub sampling to coarsen the resolution and shrink the overall grid dimensions to achieve a 4 to 10 hr simulation of modeled tsunami waves within the required time period of 10 min of wall-clock time. The basis for these grids is a high-resolution digital elevation model constructed by the NGDC and NCTR using all available bathymetric, topographic, and shoreline data. For each community, data are compiled from a variety of sources to produce a digital elevation model referenced to Mean High Water in the vertical and to the World Geodetic System 1984 in the horizontal (<http://ngdc.noaa.gov/mgg/inundation/tsunami/inundation.html>). From these digital elevation models, a set of three high-resolution, “reference” elevation grids is constructed for development of a high-resolution reference model. An ‘optimized’ model is constructed to run in an operationally specified period of time. The operationally developed model is referred to as the optimized tsunami forecast model or forecast model for brevity.

3.1 Forecast area

Being the largest surf town on the north shore of Oahu Island, Hawaii, Haleiwa is a popular destination for tourists from all over the world. A two-lane highway that more

than two million visitors use each year connect the town with the neighboring communities of Waialui and Pupukea. Haleiwa has a residential population of about 4,000 people.

The Haleiwa coastline is dominated by the embayments associated with the confluence of the Kiikii and Paukaula streams and the Anahulu River (Figure 1a). A long and narrow beach, bordered in many places by deteriorated seawalls and revetments, extends from Mokuleia to Kaiaka Bay. Rocky outcrops of limestone compose both Kaiaka and Puaena points. The northwest coast of Oahu extends from Kahuku Pt. to Haleiwa, and is characterized by massive winter surf, long sandy beaches, rocky points, and patches of exposed beach rock. The beach rock is particularly exposed in the winter, when foreshore slopes steepen, and large quantities of sand are moved by high surf from the waters edge toward the back of the beach. Sand at the shoreline is mostly coarse grained and calcareous, a signature of the high energy waves that impact this coast in the winter.

To the northeast, the coast toward Kawaihoa Beach consists mostly of interspersed sand beaches and one-to-two-meter rocky escarpments of basalt or limestone. Broad wave abrasion platforms extend offshore of Mokuleia Beach, but narrow toward Kawaihoa Beach. This is a high wave-energy coastline that receives some of the largest breaking waves in the state. Wave heights as high as 15 m were recorded offshore of Haleiwa in 1996. It is also a low-sloping coast, and near the stream mouths wetlands and ponds are found. The only boat harbors along the entire North Shore of Oahu are found inside Kaiaka and Waialua Bays.

Historically, there have been two water level gauges at the Haleiwa boat harbor. The National Ocean Service installed a temporary gauge in Waialua Bay at (21.01°N, 158.0018°W) from October 7, 1983 until December 1, 1983. Another tide gauge, at the west end of the parking dock inside Haleiwa harbor (Figure 1b and 1c), was deployed and maintained by the Pacific Tsunami Warning Center (PTWC) as part of the Hawaii Civil Defense local water level upgrade that happened before the 1996 Andreanov tsunami. This gauge is a 2-minute float gauge that has a phone link to the PTWC and must be accessed manually after an event. Some of the event data are archived at the University of Hawaii Sea Level Center and some at the PTWC.

3.2 Historical tsunami events and data

The tsunami runup database at the National Geophysical Data Center (NGDC) has documented a total of 18 historical tsunami events for Haleiwa and its vicinity (Table 1). The most significant tsunami impact along Haleiwa's coastline came from the major tsunamis during the 1940s to 1960s, including the 1946 Unimak, 1952 Kamchatka, 1957 Alaska, 1960 Chile and 1964 Alaska. The runup height at Haleiwa resulted from these tsunami reached 5.2 m above mean sea level during the 1957 Alaska event, and a minimum of 3 m during the 1964 Alaskan tsunami. Figure 2 shows a snapshot of Haleiwa bear the entrance of Anahulu Stream after 1946 Unimak tsunami. It indicates light damage, but the debris reached up to 3 m on land. Figure 3 shows an aerial view of Kaiaka Bay near Haleiwa when the fourth wave was climbing up the beach toward the beach houses during the 1957 Kamchatka tsunami, and it also shows the extent of

inundation from previous waves.

Since 1960s, Haleiwa coastlines have experienced less severe damages from a few small tsunamis with water level mostly less than 0.6 m until the March 11, 2011 Japan tsunami occurred. Although the Haleiwa tide gage was not functioning during this tsunami, online footages (<http://www.youtube.com/watch?v=oJL6R9UvM5s>) and report (DePledge, 2011) have shown that about 1.8-m-high tsunami waves attacked Haleiwa harbor and caused damages to the harbor facilities and boats. DePledge (2011) reported that a series of small and powerful surges, as many as 20, pushed muddy water from the tsunami through the Haleiwa Boat Harbor early that morning. The most recent two tsunami events of 2012 Haida Gwaii and 2013 Solomon Islands (Figure 4) caused small tsunamis at Haleiwa, and the maximum water levels recorded at the tide gauge are 0.44 m, and 0.19 m, respectively.

3.3 Model setup

3.3.1 Grid boundary and resolution

The long distance from the Pacific Rim and steep bathymetric setting complicates the modeling of tsunami waves approaching the shorelines of Hawaii Islands. When a tsunami reaches shallow shelf and begins to shoal, it will slow down and increase in height while introducing model diffusion and dispersion. Burwell et al. (2007) studied the diffusion and dispersion characterization of MOST model, and concluded that the nature of the scheme, at all resolvable wave numbers, is diffusive and dispersive for $\beta = (gd)^{1/2} \Delta t / \Delta x \neq 1$, where Δt is the temporal step and Δx is the space step. Diffusive effects are stronger for poorly resolved waves (large space step compared to wave length). As β decreases, diffusive effects are reduced and dispersion continues to increase. Thus, numerical dispersion can be an issue closer to shore, but can be controlled through a careful choice of β , or in other words, the ratio between Δt and Δx . The tsunami propagation database (Gica et al., 2008) was developed at a grid spacing of 4-arc-minute (about 7.2 km at the equator) and saved at 16-arc-minute (about 28.8 km at the equator) resolution. This resolution may introduce large model diffusion effects if applied directly to the continental shelf, where the water depth is generally less than 100 m. The telescoped grids adopted in the MOST model are thus critical for wave transformation over the continental shelf, and for the inundation modeling at the coastline. Ideally, manipulation of β value will reduce the effects of diffusion and mimic the real-world dispersion through numerical dispersion.

3.3.2 Digital Elevation Model of Haleiwa, Hawaii

Love et al. (2010) at the National Geophysical Data Center (NGDC) developed a 1/3-arc-sec digital elevation model for entire Island of Oahu. The bathymetry was developed base on NGDC multibeam database in 2011, NOS/BAG hydrographic survey soundings between 2008 and 2009, and OCS navigation charts. The U.S. Army Corp of Engineers (USACE) Scanning Hydrographic Operational Airborne Lidar Survey (SHOALS) between 1999 and 2000 provided high resolution (1 to 5 m) coverage along Oahu's coastlines. The USGS National Elevation Dataset (NED) provides complete 1/3 –arc-sec

coverage of the Hawaiian Islands. Figure 5 shows the source data coverage in NGDC's 1/3-arc-sec DEM in the Oahu region. Love et al. (2010) indicated that all vertical datum were transformed to Mean High Water (MHW), and all horizontal datum were referenced to WGS 84 geographic or NAD 83 geographic datum.

Love et al. (2010) provided a detailed description of how these datasets were implemented in the DEM development for Haleiwa. The bathymetry and topography used in the development of this forecast model was based on a digital elevation model provided by the National Geophysical Data Center and the author considers it to be an adequate representation of the local topography/bathymetry. As new digital elevation models become available, forecast models will be updated and report updates will be posted at http://nctr.pmel.noaa.gov/forecast_reports/.

An inspection of the NGDC's Haleiwa DEM discovered that the breakwaters at the entrance of Haleiwa Harbor were not correctly accounted. The DEM needs to be modified to establish these critical structures in the harbor to obtain more accurate model forecast. Sargent et al. (1988) described the case history of U.S. Army Corps of Engineers (USACE) breakwater and jetty structures in Hawaii. Figure 6 (Sargent et al., 1988) shows the typical breakwater cross sections in Haleiwa Harbor. The crest of the 80-feet-long breakwater (west of the harbor entrance) has an elevation of 2.44 m above MLL, and 1.94 m above MHW (MHW is 0.499 m above the MLLW at Haleiwa <http://tidesandcurrents.noaa.gov/benchmarks/1612668.html#DatumsPage>). The 110-feet-long breakwater is crested 3.05 m above MLLW, which gives an elevation of 2.55 m above MHW. The crest widths of both breakwaters are both 3 m. These structures are added to the NGDC's DEM.

3.4.4 Development of model grids

Development of an optimized tsunami forecast model for Haleiwa began with the merged bathymetric/topographic grids shown in **Figure 7 to 8**. Grid dimension extension and additional information were updated as needed and appropriate. **Table 2** provides specific details of both reference and tsunami forecast model grids, including extents and complete input parameter information for the model runs is provided in **Appendix A**.

Figures 7 show the coverage of the reference model, where its A, B, and C grids have spatial resolutions of 36 arc seconds ($\sim 1,110$ m), 6 arc sec (~ 185 m) and 1/3 arc sec (~ 10 m), respectively. The reference model A grid covers the region between 161.0°W and 154.02°W in longitudinal direction, and between 18.0083°N and 22.9983°N in latitudinal direction. This grid covers all eight main islands in the Hawaii Islands chain, and generally the water depth at its boundaries exceeds 5,000 m (Figure 7a). This setup ensures the tsunami wave dynamics in the deep ocean are properly extended from the propagation database to the inundation models before they reach the shallow coastal regions. The reference model B grid covers the region between 158.497°W and 156.837°W in longitude, and between 20.46°N and 21.8667°N in latitude. With higher resolution than that in A grid, B grid provides computation of tsunami dynamics neashore, especially in the transition zone when water depth drops from 2,000 m to tens of meters, where the grid resolution cannot be too coarse to account the wave

transformation when approaching the shore. B grid covers the entire Island of Oahu, as well as most of the two islands, Molokai and Lanai, to the east of Oahu. The waterway between Oahu and these two islands is known as Penguin Bank, and its shallow water (less than 50 m) tends to generate rapid flow there and modify the water dynamics in the vicinity. Therefore, it is important to include the Penguin Bank in the computational domain to account for its interference with passing tsunami waves. The reference model C grid covers the region between 158.165°W and 158.085°W in longitude, and between 21.55°N and 21.625°N in latitude. The C grid covers the coastline between Mokulei and south of Kawaiola Beach accounting for most of the residential area along Haleiwa's coastline (Figure 1). With the implementation of SHOALS data, one can observe that the 1/3-arc-sec DEM includes detailed coral structures offshore of Haleiwa. However, the land topography is mostly below one meter above MHW, which was probably interpolated from a dataset different than the SHOALS data. The topography along Haleiwa's coastline, especially below 10-m elevation, needs to be updated when better lidar data becomes available as it may potentially result in overestimation of tsunami flooding during a tsunami forecast.

Figures 8 show the coverage of the forecast model, where its A and B grids have spatial resolutions of two arc min ($\sim 3,700 \text{ m}$), 18 arc sec ($\sim 555 \text{ m}$), respectively. Similar to the reference model, the forecast model A grid covers the region between 161.0°W and $154.03333^{\circ}\text{W}$ in longitude, and between 18.03167°N and 22.98333°N in latitude (Figure 8a). The forecast model B grid covers the region between 156.4967°W and 157.2317°W in longitude, and between 20.7217°N and 21.8667°N in latitude. Different than the coverage of A grid, the B grid covers the entire Island of Oahu, but with slightly less coverage in the west excluding the Islands of Molokai and Lanai to save computational time (Figure 8b). The forecast model C grid has the same coverage over the same region as in the C grid of reference model (Figure 8c). In general, the grid resolution implemented in the C grid of a forecast model is 1 to 3 arc sec (Tang et al., 2010). However, these grid sizes are still too coarse to render an accurate presentation of the harbor layout unless a grid finer than 1/3 arc sec ($\sim 10 \text{ m}$) is used. Therefore, a mixture of grid resolutions at 1 arc sec ($\sim 30 \text{ m}$), 2/3 arc sec ($\sim 20 \text{ m}$) and 1/3 arc sec ($\sim 10 \text{ m}$) is implemented, as shown in Figure 9. The 1/3-arc-sec grids mainly focus on the harbor area, while the 2/3-arc-sec grids are providing a smooth transition of computational results between the 1-arc-sec and 1/3-arc-sec grids. This grid setting provides an optimization between computational speed and accuracy.

4. Results and Discussion

4.1 Model validation

Although a number of historical tsunamis were documented along Haleiwa's coastline (Table 1), the time series of only three events was made available for model validation in the present study. These events include the 1996 Andreanov, the 2012 Haida Gwaii and the 2013 Solomon Islands.

The 1996 Andreanov tsunami was spawned by an earthquake of $M_w 7.9$ off the Andreanov Island 50 miles SW of Adak, Alaska on June 10, 1996 at 04:03:36 UTC. Data

from 127 separate tide gauge and bottom pressure stations during the initial earthquake and subsequent tsunami are reported by Eble et al. (1997). A tsunami source was inverted based on the bottom pressure data and used for model computation (Table 3) to validate the measurements at Haleiwa tide gauge. The recorded waveforms at the Haleiwa tide gauge indicates the maximum wave amplitude is about 26.1 cm, while the forecast model and reference model give 48.2 cm and 44.8 cm with an overestimation of the first wave by 85% and 72% (Table 4), respectively. The computed arrival time matches very well with the observations, so does the wave period. The models also well reproduce the wave decay four to five hours after the first wave. The computational results in Figure 10 (a-d) indicate there was no tsunami flooding along the coastline. The computed maximum water level was about 0.5 m with a maximum flow speed about 1 m/s. Based on the computational results, the tsunami waves probably had affected Kaiaka Bay more than the Haleiwa Harbor. The model results between the reference model and the forecast model are mostly comparable except the forecast model seems to sustain the large waves longer than the reference model with some phase shift in the late waves.

The 2012 Haida Gwaii tsunami triggered by an M_w 7.7 earthquake off the coast of Haida Gwaii, Canada was reported by a few deep-ocean tsunamieters with up to 6 cm peak. A real-time inversion using these deep-ocean measurements estimated an average slip of 2.8 m over a 200 km \times 100 km rupture area with a mix of reverse- and normal-fault ruptures. The model results using this source gave good comparison with the recorded data (Figure 11). At the Haleiwa tide gauge, both the reference and the forecast models predicted a slightly earlier arrival time than the observations, but produced agreeable wave amplitude at the second wave. Although both models underestimated the third wave, the maximum one, by 26% and 30% respectively, the matching of the following four waves indicates a reasonable estimation of the tsunami waves in the harbor.

The 2013 Solomon tsunami was generated by an M_w 8.0 earthquake (10.738°S 165.138°E), at 2013-02-06 01:12:27 UTC, 76 km West of Lata, Solomon Islands. The inversion based on deep-ocean tsunamieters indicated an average of 2.3 m slip mostly concentrated along a 150 km \times 50 km rupture area, which is consistent to the two large-slip patches derived by Lay et al. (2013) from iterative modeling of teleseismic broadband P waves and the deep-water tsunami recordings. Figure 12 shows the DART-constrained source provided a good estimation of the tsunami water levels at Haleiwa tide gage - the forecast model shows a slight overestimation (20.6 cm) of the recorded maximum water level (19.6 cm), while the forecast model underestimates (15.2 cm). With a time shift of +6 min, one can observe that the computed wave period is also close to the observations. The results from the forecast model and the reference model show some discrepancies in wave amplitude - the computational results obtained by the reference model are generally smaller, especially in the Kaiaka Bay. Figure 12e-f shows the model results start to deviate at the time of 3.5 hours after the tsunami arrived at Haleiwa tide gauge. This may be introduced by different grid configurations in the A grids.

The computational results from the forecast model and the reference model show consistency in wave amplitude, wave period, arrival time, and current speed, but also show some second-order discrepancies in the late waves. Using similar grid resolution

and coverage in the A grid may improve the agreement between the forecast model and the reference model, but will also increase the computing time. The forecast model is considered to be a balance between the model accuracy and model speed.

4.2 Model stability testing using synthetic scenarios

Model stability testing using synthetic scenarios provides important case studies to test the robustness, durability, and efficiency of the developed models from different perspectives:

1. Synthetic scenarios examine the developed models with mega tsunamis to guarantee model stability. These model tests ensure the efficiency of the forecast model during a catastrophic event.
2. Synthetic scenarios also examine the developed models with medium tsunamis to guarantee model stability under smaller wave conditions. These model tests ensure the efficiency of the forecast model during a moderate event.
3. Synthetic scenarios examine the developed models with negligible tsunami waves to guarantee the modeling results are not interfered by the numerical noises.

The synthetic scenarios were selected in such way that at least one from each potential tsunami source zone is tested. These cases are used to examine the reliability of the developed models in response to the directionality of tsunami waves.

Table 5 summarized all the synthetic scenarios (plotted in **Figure 13**) used in the present model testing. All scenarios are artificially constructed using a combination of the unit sources, shown as black boxes. Table 5 gives the details of unit source and the coefficients for a total of 21 scenarios, including 19 with magnitude 9.3, one with magnitude 7.5 and one micro-wave scenario. All scenarios were tested in forecast model for 24-hour model run, and reference model with 8-hour run. All tests were successful to maintain the model stability throughout the run.

Because Haleiwa's coastline is mostly featuring with large area of low ground level, less than 1 m (above MHW) (Figure 7 and 8), the testing results of every Mw 9.3 scenario in this study shows extensive flooding in Haleiwa between Mokuleia and Haleiwa Harbor (Figure 14 to 32). The subduction zones in the Northwest Pacific, such as Aleutian and Kamchatka, are the most catastrophic source regions that may cause tsunami flooding along Haleiwa's coastline.

Among all 21 scenarios, the M_w 9.3 synthetic scenario ACSZ 16-25 in the western Alaska-Aleutian subduction zone generates the most catastrophic tsunami waves to Haleiwa. Figure 19 shows ACSZ 16-25 produces significant flooding along the coastline of Haleiwa, and the maximum water level is more than 20 m above Mean High Water. The modeling results show that the flow speed exceeds 20 m/s when the wave front breaks at the reef crest offshore, and can still maintain at the level of 5 – 15 m/s when it propagates on land. Figure 19 e and 19f show that the water level at the Haleiwa tide gauge may reach 20 m above Mean High Water. The maximum level appears with the second wave, and the wave amplitude quickly decays to about half of the maximum on

the third wave. However, the water level does not decay to less than 1 m until four hours later. The maximum water level and flow speed obtained from both forecast model and reference model are generally consistent, and the forecast model produces slightly higher values at places. Similarly, the computed time series at the tide gauge location agree with each other between the forecast model and the reference model (Figure 19 e and f). However, the maximum water level computed from the reference model is about 19 m, while the forecast model gives about 16 m. The phases of the waves show some discrepancy between the two models.

Comparing to ACSZ 16-25, the KISZ 01-10 scenario poses >10 m water level to Haleiwa's coastal community with slightly less flooding (Figure 14). The flow speed is mostly between 5 to 10 m/s on land, which may still cause dramatic damages in Haleiwa. The computed maximum wave amplitude is about 10 m above MHW at Haleiwa tide gauge, with sustained large waves affecting the harbor until almost a day after the earthquake. Similar to the results shown in ACSZ 16-25, the forecast model gives agreeable results with the reference model for the first two waves, but starts to show discrepancies in wave amplitude and temporal phase in the late waves. We attribute these discrepancies to different grid coverage and grid resolution implemented in these two models.

In all tested scenarios, the tsunami impact from South America seems to be the least along Haleiwa's coastline. Most of the flooding happens only over the ground lower than one meter (Figure 23 to 26), and the flow speed is less than 1 m/s on land. It's worth pointing out that the southernmost source region (ASCZ 102-111) may cause greater impact than other South-America scenarios due to the fault alignment, which affects the radiation of the tsunami energy in the ocean basin along with the bathymetry (Titov et al., 2005b; Grilli et al., 2007). In all the CSSZ scenarios, one may see that the inundated areas computed by the forecast model are generally smaller than those computed from the reference model. Table 5 indicates that the computed maximum wave amplitude in the forecast model is generally about 5 to 38% smaller, and the low-lying ground is very sensitive to the variation of water level.

Other M_w 9.3 tsunami sources from Southern and Western Pacific, except for NGSZ 03-12 (Figure 30), floods Haleiwa's coastline with 2- to 3-m waves with tsunami flow of 2 to 3 m/s in the vicinity (Figure 27-29). NGSZ 03-12 is among the smallest sources affecting Haleiwa's coastline, with limited inundation in the areas between Mokuleia and Haleiwa harbor, focusing its impact on the Kaiaka Bay. The maximum wave amplitude at the Haleiwa Harbor tide gauge is less than 1 m (Figure 30).

The synthetic scenario of magnitude 7.5, NTSZ b36, introduces only up to 0.1 m wave amplitude along the shoreline of Haleiwa, mostly in the harbor and Kaiaka Bay, without any water penetration inland. The forecast model shows larger wave amplitude and flow speed than the reference model (Figure 33). The micro scenario EPSZ b19 is very useful in testing the model stability under the conditions of negligible wave. From the computed maximum wave amplitude in Figure 34, one can see that the water elevation at the oceanfront is only on the order of 10^{-4} to 10^{-3} m, and the computed time series from both models have reasonable match except the forecast model produces larger wave

amplitude. Similar to other scenarios, these discrepancies may originate from different grid coverage and resolution in the A and B grids. In addition, the two models show difference mostly over the reefing area, where the reference model describes many more local bathymetric and topographic features that may damp more wave energy.

5. Summary and conclusions

Haleiwa, Hawaii is a coastal community on the north shore of Oahu Island and is known of its vulnerability to potential tsunami hazards, which pose long-standing challenges for the coastal communities on how to protect their lives and properties. Tsunami forecast and hazard assessment in Haleiwa, however, remains significantly understudied, probably due to infrequent occurrence of tsunamis in Haleiwa's history.

A tsunami forecast model is presently developed for the community of Haleiwa, Hawaii. The developed model is being implemented into NOAA's Short-term Inundation Forecast of Tsunamis (SIFT) to provide real-time modeling forecasts of tsunami wave characteristics, runup and inundation along Haleiwa's coastline. Discussion of the details of each individual components of the forecast model, including the bathymetry and topography, the basic model setup, and the model parameters are provided in the report. The forecast model employs grids as fine as 1/3 arc sec (9 m) around the harbor area and 1 arc sec (~ 30 m) and 2/3 arc sec (~ 20 m) offshore. Due to the high-resolution computation, the forecast model accomplishes a four-hour simulation, after tsunami arrival, in about 20 minutes of computer CPU time. Parallelly, this study also developed a reference model of 1/3 arc sec (~ 9 m) throughout the C grid to provide reference results basis for performance evaluation of the forecast model. Model validation and tests indicate that forecast model and reference model show consistency in the modeling results, however forecast model shows up to 30% difference in the maximum wave amplitude. Forecast model also shows slight discrepancies in wave period and phase speed.

Haleiwa tide station has recorded several tsunamis. The 1996 Andreanov, 2012 Haida Gwaii, and 2013 Solomon Islands tsunamis were used for model validation. The models correctly predicted the arrival time and first few waves. The model over-predicted the maximum wave amplitude at the tide station for the 1996 Andreanov tsunami, but provides reasonable estimation of the tsunami waves for the other two events.

A total of 21 synthetic scenarios, including 19 synthetic events generated by an M_w 9.3 source, one synthetic event due to an M_w 7.5 source, and one micro-size tsunami, were used to examine the stability of the developed forecast model and reference model for Haleiwa. The synthetic scenarios were selected in such way that at least one from each of the major source zones in the Pacific is tested. Both the forecast models and reference model give stable results for all synthetic scenarios representing tsunami waves from different source locations and different directionalities. Other than testing the model stability, these synthetic scenarios are also useful to summarize some common the characteristics of tsunami waves generated from these source zones.

1. Most of the M_w 9.3 earthquake from the major subduction zones in the Pacific may cause catastrophic tsunami along Haleiwa's coastline. The modeling results show such a tsunami (ACSZ 16 to 25) would inundate the entire vicinity with waves as high as 20 m.
2. Other scenarios are unlikely to cause major flooding at the waterfront of Nikolski, They are less threatening, but the high seas and rapid flow may still cause damages to coasts along Umnak Bay in terms of fishing activity, ecology system, as well as coastal facilities.
3. Tsunami waves inside Haleiwa Harbor are featured with long-time wave oscillation, which may sustain the large waves for hours, even one day, before the tsunami warning ends.
4. All model results indicate that areas between Mokuleia and Haleiwa Harbor are vulnerable to tsunami hazards, especially the vicinity around Kaiaka Bay. Its location in turning point of north shore of Oahu is very effective to trap the tsunami energy.

All model validation and stability tests demonstrated that the developed tsunami forecast model and reference model for Haleiwa, Hawaii, are robust and efficient for their implementation into both the short-term real-time tsunami forecast system and long-term tsunami inundation investigations, although the models needs to be further updated when more accurate DEMs become available.

6. Acknowledgement

Funding for this publication and all work leading to development of a tsunami forecast model for Haleiwa, Hawaii was provided by the National Oceanic and Atmospheric Administration. This publication was partially funded by the Joint Institute for the Study of the Atmosphere and Ocean (JISAO) under NOAA Cooperative Agreement NO. NA17RJ1232, JISAO Contribution No. ****. This is PMEL Contribution No. ****.

References

- Burwell, D., E. Tolkova, and A. Chawla (2007), Diffusion and dispersion characterization of a numerical tsunami model, *Ocean Modeling*, 19, 10-30.
- DePledge, D. (2011). ‘Tsunami resistant’ dock breaks at Haleiwa harbor, Star Advertisement, posted on March 11, 2011.
- Eble, M.C., J. Newman, J. Wendland, B. Kilonsky, D. Luther, Y. Tanioka, M. Okada, and F.I. Gonzalez (1997): The 10 June 1996 Andreanov tsunami database. NOAA DR ERL PMEL-64 (PB98-130495), 101 pp.
- Gica, E., M. Spillane, V.V. Titov, C. Chamberlin, and J.C. Newman (2008), Development of the forecast propagation database for NOAA's Short-term Inundation Forecast for Tsunamis (SIFT). NOAA Tech. Memo. OAR PMEL-139, 89 pp.
- Grilli, S.T., M. Ioualalen, J. Asavanant, F.Y. Shi, J.T. Kirby, and P. Watts (2007). Source constraint and model simulation of the December 26, 2004, Indian Ocean tsunami, *J. Waterway Port Coastal Ocean Eng.*, 133(6), 414-428.
- Lay T., L. Ye, H. Kanamori, Y. Yamazaki, K.F. Cheung, and C.J. Ammon (2013): The February 6, 2013 M_w 8.0 Santa Cruz Islands earthquake and tsunami, *Tectonophysics*,
- Love, M.R., D.Z. Friday, P.R. Grothe, E. Lim, K.S. Carignan, B.W. Eakins, and L.A. Taylor, 2011. Digital Elevation Model of Oahu, Hawaii: Procedures, Data Sources and Analysis, NOAA National Geophysical Data Center technical report, Boulder, CO, 15 pp.
- Sargent, F.E., Markle, D.G., Grace, P.J. (1988). Case histories of Corps breakwater and jetty structures, *Technical Report REMR-CO-3, Report 4*, Pacific Ocean Division, Department of Army, Waterways Experiment Station, Corps of Engineers, Vicksburg, Mississippi, p. 46.
- Synolakis, C.E., E.N. Bernard, V.V. Titov, U. Kanoğlu, and F.I. González (2008): Validation and verification of tsunami numerical models. *Pure Appl. Geophys.*, 165(11– 12), 2197–2228.
- Tang, L., V.V. Titov, E. Bernard, Y. Wei, C. Chamberlin, J.C. Newman, H. Mofjeld, D. Arcas, M. Eble, C. Moore, B. Uslu, C. Pells, M.C. Spillane, L.M. Wright, and E. Gica (2012): Direct energy estimation of the 2011 Japan tsunami using deep-ocean pressure measurements. *J. Geophys. Res.*, 117, C08008, doi: 10.1029/2011JC007635.
- Tang, L., V. V. Titov, and C. D. Chamberlin (2009), Development, testing, and applications of site-specific tsunami inundation models for real-time forecasting, *J. Geophys. Res.*, 114, C12025, doi:10.1029/2009JC005476.
- Tang, L., V.V. Titov, Y. Wei, H.O. Mofjeld, M. Spillane, D. Arcas, E.N. Bernard, C. Chamberlin, E. Gica, and J. Newman (2008): Tsunami forecast analysis for the May 2006 Tonga tsunami. *J. Geophys. Res.*, 113, C12015, doi: 10.1029/2008JC004922.
- Titov, V.V. (2009): Tsunami forecasting. Chapter 12 in *The Sea, Volume 15: Tsunamis*, Harvard University Press, Cambridge, MA and London, England, 371–400.
- Titov, V., and F.I. González (1997): Implementation and testing of the Method of Splitting Tsunami (MOST) model. NOAA Tech. Memo. ERL PMEL-112 (PB98-122773), NOAA/Pacific Marine Environmental Laboratory, Seattle, WA, 11 pp.
- Titov, V.V., F.I. González, E.N. Bernard, M.C. Eble, H.O. Mofjeld, J.C. Newman, and A.J. Venturato (2005a): Real-time tsunami forecasting: Challenges and solutions. *Nat. Hazards*, 35(1), Special Issue, U.S. National Tsunami Hazard Mitigation

Program, 41–58.

Titov, V.V., A.B. Rabinovich, H.O. Mofjeld, R.E. Thomson, and F.I. González (2005b),
The global reach of the 26 December 2004 Sumatra Tsunami. *Science*. doi:
10.1126/science.1114576.

Wei, Y., E. Bernard, L. Tang, R. Weiss, V. Titov, C. Moore, M. Spillane, M. Hopkins,
and U. Kanoğlu (2008): Real-time experimental forecast of the Peruvian tsunami of
August 2007 for U.S. coastlines. *Geophys. Res. Lett.*, 35, L04609, doi:
10.1029/2007GL032250.

Wei, Y., C. Chamberlin, V.V. Titov, L. Tang, and E.N. Bernard (2013): Modeling of the
2011 Japan tsunami - Lessons for near-field forecast. *Pure Appl. Geophys.*, 170(6–8),
doi: 10.1007/s00024-012-0519-z, 1309–1331.

Tables

Table 1. Historical tsunami events that have affected Haleiwa, Hawaii

Table 2: MOST setup parameters for reference and forecast models for Haleiwa, Hawaii.

Table 3. Tsunami sources of historical events that were recorded at Haleiwa tide station and used for model validation.

Table 4. Computed maximum wave amplitude at Haleiwa tide station for historical events. The percentage in the parenthesis is the model error of the maximum wave amplitude at the Haleiwa tide gage, where the error = $(\eta_{\text{model}} - \eta_{\text{obs}}) / \eta_{\text{obs}} \times 100\%$. η_{model} is the computed maximum wave amplitude, and η_{obs} is the observed maximum wave amplitude.

Table 5. Synthetic tsunami events in the Pacific.

Table 6. Computed maximum wave amplitude at Haleiwa tide station for synthetic scenarios. The percentage in the parenthesis is the error of the maximum wave amplitude at the Haleiwa tide gage computed using the two forecast models in reference to the reference model, where the error = $(\eta_{\text{fm}} - \eta_{\text{rm}}) / \eta_{\text{rm}} \times 100\%$. η_{fm} is the computed maximum wave amplitude using the forecast models, and η_{rm} is the computed maximum wave amplitude using the reference model.

Table 1. Historical tsunami events that have affected Haleiwa, Hawaii

Event	Date, Time (UTC), Epicenter	Magnitude	Earthquake source area	Max water elev. at Haleiwa, HI
1878 Alaska	20 Jan	-	Aleutian Islands, Alaska	3 m
1923 Kamchatka	03 Feb. 16:01:41.0 54°N 161°E	8.3	Kamchatka, Russia	3.7 m
1946 Unimak	01 Apr 12:28:56.0 53.32°N, 163.19°W	8.1	Unimak Island, Alaska	2.4 - 3.4 m
1952 Kamchatka	04 Nov. 16:58:0.0 52.75°N 159.5°E	9.0	Kamchatka, Russia	4.6 m
1957 Alaska	09 Mar 14:22:31.9 51.292°N 175.629°W	8.6	Alaska	5.2 m
1958 Kuril Islands	06 Nov 22:58:8.6 44.53°N 148.54°E	8.3	Kuril Islands	0.1 m
1960 Chile	22 May 19:11:17.0 39.5°S 74.5°W	9.5	Chile	3.4 m
1963 Kuril Islands	13 Oct 05:17:53.4 44.77°N 149.798°E	8.5	Kuril Islands	0.3 m
1963 Kuril Islands	20 Oct 00:53:10.9 44.772°N 150.563°E	7.9	Kuril Islands	0.1 m
1964 Alaska	28 Mar 03:36:0.0 61.04°N 147.73°W	9.2	Alaska	3.0 – 4.6 m
1993 Kamchatka	08 Jun 13:03:36.4 51.218°N 157.829°E	7.5	Kamchatka, Russia	0.03
1993 Guam	08 Aug 08:34:24.9 12.982°N 144.801°E	7.8	Guam	0.07
1996 Andreanov	10 Jun 04:03:36 51.539°N 177.588°W	7.9	Andreanov Island, Alaska	0.26
1997 Kamchatka	05 Dec 11:26:54.6 54.841°N 162.035°E	7.8	Kamchatka, Russia	0.26
2006 Kuril	15 Nov 11:14:13.5 46.592°N 153.266°E	8.3	Kuril Islands	0.58
2011 Japan	11 Mar 05:46:24.1 38.297°N 142.373°E	9.0	Tohoku Island, Japan	-
2012 Haida Gwaii	28 Oct 03:04:39.2 52.47°N 132.13°W	7.7	Haida Gwaii, Canada	0.44 m
2013 Solomon Islands	06 Feb 01:13:11.29 10.686°S 164.59°W	7.9	Solomon Islands	0.19 m

Table 2: MOST setup parameters for reference and forecast models for Haleiwa, Hawaii.

		Reference Model				Forecast Models			
Grid	Region	Coverage Lat. [$^{\circ}$ N] Lon. [$^{\circ}$ W]	Cell Size [""]	nx x ny	Time Step [sec]	Coverage Lat. [$^{\circ}$ N] Lon. [$^{\circ}$ W]	Cell Size [""]	nx x ny	Time Step [sec]
A	Hawaiian Islands	18.0083 – 22.9983 161.0 – 154.02	36"	699 × 500	4.14	18.03167 - 22.98333 161.0 – 154.03333	2'	210 × 150	14.4
B	Island of Oahu	20.46 -21.8667 158.497 – 156.837	6"	997 × 845	0.54	20.7217 - 21.8667 156.4967 – 157.2317	18"	254 × 230	2.4
C	Haleiwa and its vicinity	21.55 – 21.625 158.165 - 158.085	1/3"	865 × 811	0.18	21.565 - 21.62 158.165 - 158.085	Mix of 1", 2/3" and 1/3"	331 × 239	0.4
Minimum offshore depth [m] 1.0 1.0 Water depth for dry land [m] 0.1 0.1 Friction coefficient [n^2] 0.0009 0.0009 CPU time for 4-hr simulation ~ 9.0 hours ~ 20 minutes Reference point at tide gage 158.10556W, 21.592962N (I = 233, J = 109, depth = 1.4 m in forecast model C grid; I = 643, J = 465, depth = -1.4 m in reference model C grid).									

Computations were performed on a single Intel Xeon processor at 3.6 GHz, Dell PowerEdge 1850.

Table 3. Tsunami sources of historical events that were recorded at Haleiwa tide station and used for model validation.

Event	Earthquake / Seismic			Model		
	USGS Date Time (UTC) Epicenter	CMT Date Time (UTC) Centroid	Magnitude Mw	Tsunami Magnitude ¹	Subduction Zone	Tsunami Source
1996 Andreanov	10 Jun 04:03:36 51.539°N 177.588°W	10 Jun 04:04:3.4 51.1°N 177.41°W	57.9	8.1	Alaska-Aleutian-Cascadia (ACSZ)	⁶ 3.4 × a15+0.8 × b16
2012 Haida Gwaii	28 Oct 03:04:09 52.742°N 132.131°W	28 Oct 03:04:39.2 52.47°N 132.13°W	57.7	8.8	Alaska-Aleutian-Cascadia (ACSZ)	⁶ 1.0 × a50 - 2.4 × b50 + 3.0 × a51 + 4.8 × b51
2013 Solomon Islands	06 Feb 01:12:27 10.738°S 165.138°E	06 Feb 01:13:11.29 10.686°S 164.59°W	58.0 (USGS) 7.9 (CMT)	8.0	New Britain-Solomons-Vanuatu (NVSZ)	⁶ 0.23 x b20 + 1.14 x a21 + 3.73 x b21 + 4.06 x b22

¹ Preliminary source – derived from source and deep-ocean observations

¹ López and Okal (2006)

³ United States Geological Survey (USGS)

⁴ Kanamori and Ciper (1974)

⁵ Centroid Moment Tensor

⁶ Tsunami source was obtained in real time and applied to the forecast

Table 4. Computed maximum wave amplitude at Haleiwa tide station for historical events. The percentage in the parenthesis is the model error of the maximum wave amplitude at the Haleiwa tide gage, where the error = $(\eta_{\text{model}} - \eta_{\text{obs}}) / \eta_{\text{obs}} \times 100\%$. η_{model} is the computed maximum wave amplitude, and η_{obs} is the observed maximum wave amplitude.

Historical Event	Obs. (cm)	Forecast model (cm)	Reference model (cm)
1996 Andreanov	26.1	48.2 (+ 84.7%)	44.8 (+ 71.6%)
2012 Haida Gwaii	43.8	32.4 (- 26.0%)	30.7 (- 29.9%)
2013 Solomon Islands	18.6	20.6 (+ 10.8%)	15.2 (- 18.3%)

Table 5. Synthetic tsunami events in the Pacific.

Sce No.	Scenario Name	Source Zone	Tsunami Source	α (m)
Mega-tsunami scenario				
1	KISZ 1-10	Kamchatka-Yap-Mariana-Izu-Bonin	A1-A10, B1-B10	25
2	KISZ 22-31	Kamchatka-Yap-Mariana-Izu-Bonin	A22-A31, B22-B31	25
3	KISZ 32-41	Kamchatka-Yap-Mariana-Izu-Bonin	A32-A41, B32-B41	25
4	KISZ 56-65	Kamchatka-Yap-Mariana-Izu-Bonin	A56-65, B56-65	25
5	ACSZ 6-15	Aleutian-Alaska-Cascadia	A6-A15, B6-B15	25
6	ACSZ 16-25	Aleutian-Alaska-Cascadia	A16-A25, B16-B25	25
7	ACSZ 22-31	Aleutian-Alaska-Cascadia	A22-A31, B22-B31	25
8	ACSZ 50-59	Aleutian-Alaska-Cascadia	A50-A59, B50-B59	25
9	ACSZ 56-65	Aleutian-Alaska-Cascadia	A56-A65, B56-B65	25
10	CSSZ 1-10	Central and South America	A1-A10, B1-B10	25
11	CSSZ 37-46	Central and South America	A37-A46, B37-B46	25
12	CSSZ 89-98	Central and South America	A89-A98, B89-B98	25
13	CSSZ 102 – 111	Central and South America	A102-A111, B102-B111	25
14	NTSZ 30-39	New Zealand-Kermadec-Tonga	A30-A39, B30-B39	25
15	NVSZ 28-37	New Britain-Solomons-Vanuatu	A28-A37, B28-B37	25
16	MOSZ 1-10	ManusOCB	A1-A10, B1-B10	25
17	NGSZ 3-12	North New Guinea	A3-A12, B3-B12	25
18	EPSZ 6-15	East Philippines	A6-A15, B6-B15	25
19	RNSZ 12-21	Ryukus-Kyushu-Nankai	A12-A21, B12-B21	25
Mw 7.5 Tsunami scenario				
20	NTSZ B36	New Zealand-Kermadec-Tonga	B36	1
Micro-tsunami scenario (select one)				
21	EPSZ B19	East Philippines	B19	0.01

Table 6. Computed maximum wave amplitude at Haleiwa tide station for synthetic scenarios. The percentage in the parenthesis is the error of the maximum wave amplitude at the Haleiwa tide gage computed using the two forecast models in reference to the reference model, where the error = $(\eta_{fm} - \eta_{rm}) / \eta_{rm} \times 100\%$. η_{fm} is the computed maximum wave amplitude using the forecast models, and η_{rm} is the computed maximum wave amplitude using the reference model.

Synthetic events	Forecast model 1 (m)	Reference model (m)
KISZ 01 to 10	10.21 (+ 4.5%)	9.78
KISZ 22 to 31	4.01 (+5.1%)	3.81
KISZ 32 to 41	4.49 (- 3.5%)	4.65
KISZ 56 to 65	2.12 (+ 17.1%)	1.81
ACSZ 06 to 15	2.93 (+ 0.7%)	2.92
ACSZ 16 to 25	16.40 (- 15.9%)	19.50
ACSZ 22 to 31	4.93 (+ 24.8%)	3.95
ACSZ 50 to 59	3.25 (+ 0.9%)	3.22
ACSZ 56 to 65	2.21 (- 3.7%)	2.29
CSSZ 01 to 10	1.06 (- 5.0%)	1.11
CSSZ 37 to 46	0.44 (- 37.7%)	0.70
CSSZ 89 to 98	1.05 (- 12.0%)	1.20
CSSZ 102 to 111	1.36 (- 12.2%)	1.55
NTSZ 30 to 39	2.36 (+ 9.8%)	2.15
NVSZ 28 to 37	2.48 (+ 5.1%)	2.36
MOSZ 01 to 10	2.95 (+ 4.3%)	2.83
NGSZ 03 to 12	0.70 (- 22.4%)	0.90
EPSZ 06 to 15	2.38 (+ 7.1%)	2.22
RNSZ 12 to 21	1.89 (+ 2.4%)	1.85
NTSZ B36	0.10 (+ 49.9%)	0.07

Figures:

Figure 1. (a) Aerial view of Haleiwa, Hawaii. (b) Aerial view of Haleiwa Harbor and the tide gauge location. (c) Close view of the tide gauge in Haleiwa Harbor.

Figure 2. Post-tsunami aerial photo of Haleiwa harbor after the April 1, 1946 Unimak, Alaska tsunami (Courtesy of NGDC).

Figure 3. Aerial view of Kaiaka Bay near Haleiwa on the north shore of Oahu during the 1957 Kamchatka Peninsula tsunami (Courtesy of George Curtis).

Figure 4. Historical tsunami events that have affected Haleiwa, Hawaii and are used for model validation in this study. The earthquake location are indicated by ●. The red boxes are the tsunami propagation unit sources (Gica et al., 2008). ▲ indicates the location of deep-ocean tsunamieters, where ▲ are the U.S. owned (also named DART), and ▲ are owned by foreign countries.

Figure 5. Bathymetric and topographic data sources used by NGDC to build the Oahu 1/3 arc sec DEM (courtesy of Love et al., 2011).

Figure 6. Typical breakwater cross sections in the Haleiwa Harbor (Courtesy of Sargent et al., 1988).

Figure 7. Bathymetry and topography grids of the reference model: (a) A grid, where the black box indicates the coverage of B grid; (b) B grid, where the black box indicates the coverage of C grid; (c) C grid, where the red circle indicates the location of the tide gauge.

Figure 8. Bathymetry and topography grids of the forecast model: (a) A grid, where the black box indicates the coverage of B grid; (b) B grid, where the black box indicates the coverage of C grid; (c) C grid, where the red circle indicates the location of the tide gauge.

Figure 9. Mixing of computational grid resolution in the C grid of forecast model, where the red circle denotes the tide gauge location.

Figure 10. Modeling results for the 10 June 1996 Andreanov tsunami. (a) Maximum wave amplitude in the C grid computed from the forecast model; (b) Maximum flow speed in the C-grid computed from the forecast model; (c) Maximum wave amplitude in the C grid computed from the reference model; (d) Maximum flow speed in the C-grid computed from the reference model. (e) Comparison of the computed time series with the observations at the Haleiwa tide gauge; (f) close view of (e) between 4 and 10 hours after the earthquake.

Figure 11. Modeling results for the 28 October 2012 Haida Gwaii tsunami. (a) Maximum wave amplitude in the C grid computed from the forecast model; (b) Maximum flow speed in the C-grid computed from the forecast model; (c) Maximum wave amplitude in the C grid computed from the reference model; (d) Maximum flow speed in the C-grid computed from the reference model. (e) Comparison of the computed time series with the

observations at the Haleiwa tide gauge; (f) close view of (e) between 5 and 11 hours after the earthquake.

Figure 12. Modeling results for the 26 February 2013 Solomon Islands tsunami. (a) Maximum wave amplitude in the C grid computed from the forecast model; (b) Maximum flow speed in the C-grid computed from the forecast model; (c) Maximum wave amplitude in the C grid computed from the reference model; (d) Maximum flow speed in the C-grid computed from the reference model. (e) Comparison of the computed time series with the observations at the Haleiwa tide gauge; (f) close view of (e) between 6 and 12 hours after the earthquake.

Figure 13. Synthetic events for model testing.

Figure 14. Modeling results for the synthetic event KISZ 01 to 10. (a) Maximum wave amplitude in the C grid computed from the forecast model; (b) Maximum flow speed in the C-grid computed from the forecast model; (c) Maximum wave amplitude in the C grid computed from the reference model; (d) Maximum flow speed in the C-grid computed from the reference model. (e) Comparison of the time series computed by the forecast model and the reference model; (f) close view of (e) between 5.5 and 11.5 hours after the earthquake.

Figure 15. Modeling results for the synthetic event KISZ 22 to 31. (a) Maximum wave amplitude in the C grid computed from the forecast model; (b) Maximum flow speed in the C-grid computed from the forecast model; (c) Maximum wave amplitude in the C grid computed from the reference model; (d) Maximum flow speed in the C-grid computed from the reference model. (e) Comparison of the time series computed by the forecast model and the reference model; (f) close view of (e) between 7 and 13 hours after the earthquake.

Figure 16. Modeling results for the synthetic event KISZ 32 to 41. (a) Maximum wave amplitude in the C grid computed from the forecast model; (b) Maximum flow speed in the C-grid computed from the forecast model; (c) Maximum wave amplitude in the C grid computed from the reference model; (d) Maximum flow speed in the C-grid computed from the reference model. (e) Comparison of the time series computed by the forecast model and the reference model; (f) close view of (e) between 7 and 13 hours after the earthquake.

Figure 17. Modeling results for the synthetic event KISZ 56 to 65. (a) Maximum wave amplitude in the C grid computed from the forecast model; (b) Maximum flow speed in the C-grid computed from the forecast model; (c) Maximum wave amplitude in the C grid computed from the reference model; (d) Maximum flow speed in the C-grid computed from the reference model. (e) Comparison of the time series computed by the forecast model and the reference model; (f) close view of (e) between 7 and 13 hours after the earthquake.

Figure 18. Modeling results for the synthetic event ACSZ 06 to 15. (a) Maximum wave amplitude in the C grid computed from the forecast model; (b) Maximum flow speed in the C-grid computed from the forecast model; (c) Maximum wave amplitude in the C

grid computed from the reference model; (d) Maximum flow speed in the C-grid computed from the reference model. (e) Comparison of the time series computed by the forecast model and the reference model; (f) close view of (e) between 4 and 10 hours after the earthquake.

Figure 19. Modeling results for the synthetic event KISZ 16 to 25. (a) Maximum wave amplitude in the C grid computed from the forecast model; (b) Maximum flow speed in the C-grid computed from the forecast model; (c) Maximum wave amplitude in the C grid computed from the reference model; (d) Maximum flow speed in the C-grid computed from the reference model. (e) Comparison of the time series computed by the forecast model and the reference model; (f) close view of (e) between 4 and 10 hours after the earthquake.

Figure 20. Modeling results for the synthetic event ACSZ 22 to 31. (a) Maximum wave amplitude in the C grid computed from the forecast model; (b) Maximum flow speed in the C-grid computed from the forecast model; (c) Maximum wave amplitude in the C grid computed from the reference model; (d) Maximum flow speed in the C-grid computed from the reference model. (e) Comparison of the time series computed by the forecast model and the reference model; (f) close view of (e) between 4 and 10 hours after the earthquake.

Figure 21. Modeling results for the synthetic event ACSZ 50 to 59. (a) Maximum wave amplitude in the C grid computed from the forecast model; (b) Maximum flow speed in the C-grid computed from the forecast model; (c) Maximum wave amplitude in the C grid computed from the reference model; (d) Maximum flow speed in the C-grid computed from the reference model. (e) Comparison of the time series computed by the forecast model and the reference model; (f) close view of (e) between 5 and 11 hours after the earthquake.

Figure 22. Modeling results for the synthetic event KISZ 56 to 65. (a) Maximum wave amplitude in the C grid computed from the forecast model; (b) Maximum flow speed in the C-grid computed from the forecast model; (c) Maximum wave amplitude in the C grid computed from the reference model; (d) Maximum flow speed in the C-grid computed from the reference model. (e) Comparison of the time series computed by the forecast model and the reference model; (f) close view of (e) between 4 and 10 hours after the earthquake.

Figure 23. Modeling results for the synthetic event CSSZ 01 to 10. (a) Maximum wave amplitude in the C grid computed from the forecast model; (b) Maximum flow speed in the C-grid computed from the forecast model; (c) Maximum wave amplitude in the C grid computed from the reference model; (d) Maximum flow speed in the C-grid computed from the reference model. (e) Comparison of the time series computed by the forecast model and the reference model; (f) close view of (e) between 7 and 13 hours after the earthquake.

Figure 24. Modeling results for the synthetic event CSSZ 37 to 46. (a) Maximum wave amplitude in the C grid computed from the forecast model; (b) Maximum flow speed in the C-grid computed from the forecast model; (c) Maximum wave amplitude in the C

grid computed from the reference model; (d) Maximum flow speed in the C-grid computed from the reference model. (e) Comparison of the time series computed by the forecast model and the reference model; (f) close view of (e) between 12 and 18 hours after the earthquake.

Figure 25. Modeling results for the synthetic event CSSZ 89 to 98. (a) Maximum wave amplitude in the C grid computed from the forecast model; (b) Maximum flow speed in the C-grid computed from the forecast model; (c) Maximum wave amplitude in the C grid computed from the reference model; (d) Maximum flow speed in the C-grid computed from the reference model. (e) Comparison of the time series computed by the forecast model and the reference model; (f) close view of (e) between 12 and 18 hours after the earthquake.

Figure 26. Modeling results for the synthetic event CSSZ 102 to 111. (a) Maximum wave amplitude in the C grid computed from the forecast model; (b) Maximum flow speed in the C-grid computed from the forecast model; (c) Maximum wave amplitude in the C grid computed from the reference model; (d) Maximum flow speed in the C-grid computed from the reference model. (e) Comparison of the time series computed by the forecast model and the reference model; (f) close view of (e) between 15 and 21 hours after the earthquake.

Figure 27. Modeling results for the synthetic event NTSZ 30 to 39. (a) Maximum wave amplitude in the C grid computed from the forecast model; (b) Maximum flow speed in the C-grid computed from the forecast model; (c) Maximum wave amplitude in the C grid computed from the reference model; (d) Maximum flow speed in the C-grid computed from the reference model. (e) Comparison of the time series computed by the forecast model and the reference model; (f) close view of (e) between 5 and 11 hours after the earthquake.

Figure 28. Modeling results for the synthetic event NVSZ 28 to 37. (a) Maximum wave amplitude in the C grid computed from the forecast model; (b) Maximum flow speed in the C-grid computed from the forecast model; (c) Maximum wave amplitude in the C grid computed from the reference model; (d) Maximum flow speed in the C-grid computed from the reference model. (e) Comparison of the time series computed by the forecast model and the reference model; (f) close view of (e) between 7 and 13 hours after the earthquake.

Figure 29. Modeling results for the synthetic event MOSZ 01 to 10. (a) Maximum wave amplitude in the C grid computed from the forecast model; (b) Maximum flow speed in the C-grid computed from the forecast model; (c) Maximum wave amplitude in the C grid computed from the reference model; (d) Maximum flow speed in the C-grid computed from the reference model. (e) Comparison of the time series computed by the forecast model and the reference model; (f) close view of (e) between 8 and 14 hours after the earthquake.

Figure 30. Modeling results for the synthetic event NGSZ 03 to 12. (a) Maximum wave amplitude in the C grid computed from the forecast model; (b) Maximum flow speed in the C-grid computed from the forecast model; (c) Maximum wave amplitude in the C

grid computed from the reference model; (d) Maximum flow speed in the C-grid computed from the reference model. (e) Comparison of the time series computed by the forecast model and the reference model; (f) close view of (e) between 9 and 15 hours after the earthquake.

Figure 31. Modeling results for the synthetic event EPSZ 06 to 15. (a) Maximum wave amplitude in the C grid computed from the forecast model; (b) Maximum flow speed in the C-grid computed from the forecast model; (c) Maximum wave amplitude in the C grid computed from the reference model; (d) Maximum flow speed in the C-grid computed from the reference model. (e) Comparison of the time series computed by the forecast model and the reference model; (f) close view of (e) between 10 and 16 hours after the earthquake.

Figure 32. Modeling results for the synthetic event RNSZ 12 to 21. (a) Maximum wave amplitude in the C grid computed from the forecast model; (b) Maximum flow speed in the C-grid computed from the forecast model; (c) Maximum wave amplitude in the C grid computed from the reference model; (d) Maximum flow speed in the C-grid computed from the reference model. (e) Comparison of the time series computed by the forecast model and the reference model; (f) close view of (e) between 7.5 and 13.5 hours after the earthquake.

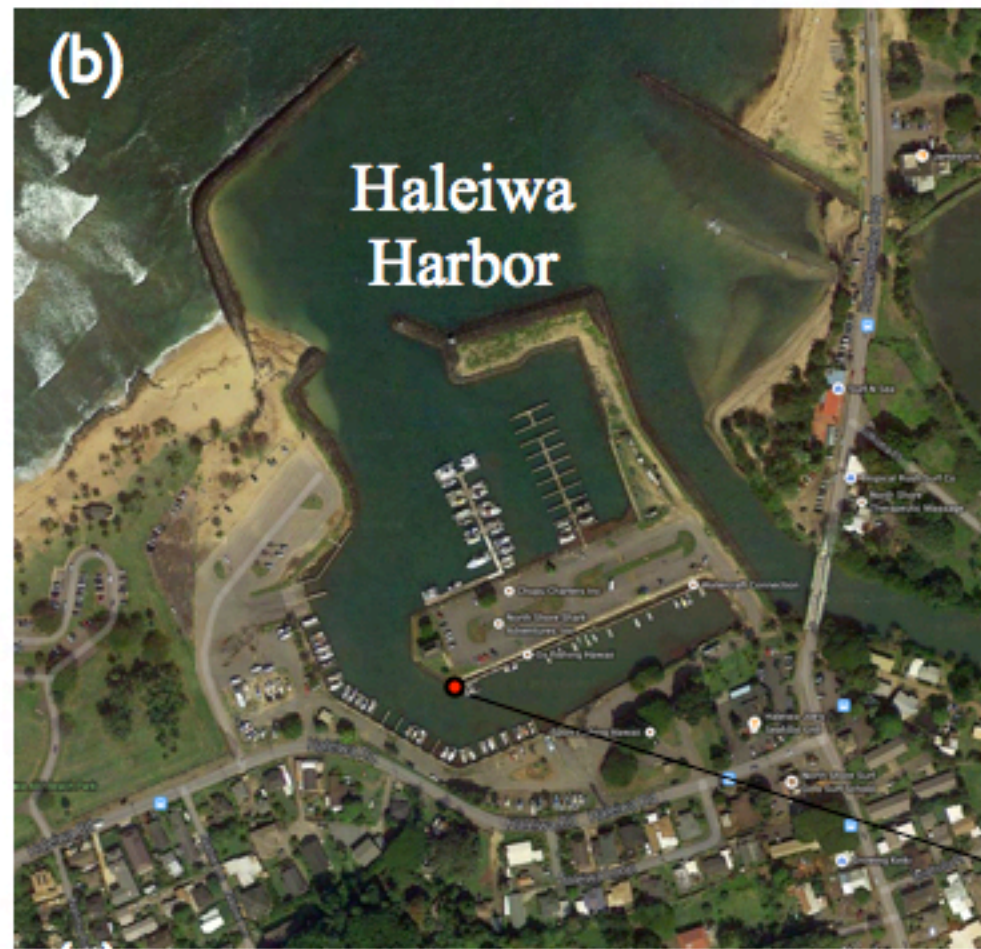
Figure 33. Modeling results for the synthetic event NTSZ b36. (a) Maximum wave amplitude in the C grid computed from the forecast model; (b) Maximum flow speed in the C-grid computed from the forecast model; (c) Maximum wave amplitude in the C grid computed from the reference model; (d) Maximum flow speed in the C-grid computed from the reference model. (e) Comparison of the time series computed by the forecast model and the reference model; (f) close view of (e) between 5.5 and 11.5 hours after the earthquake.

Figure 34. Modeling results for the synthetic event EPSZ b19. (a) Maximum wave amplitude in the C grid computed from the forecast model; (b) Maximum flow speed in the C-grid computed from the forecast model; (c) Maximum wave amplitude in the C grid computed from the reference model; (d) Maximum flow speed in the C-grid computed from the reference model. (e) Comparison of the time series computed by the forecast model and the reference model; (f) close view of (e) between 10 and 16 hours after the earthquake.

(a)



(b)

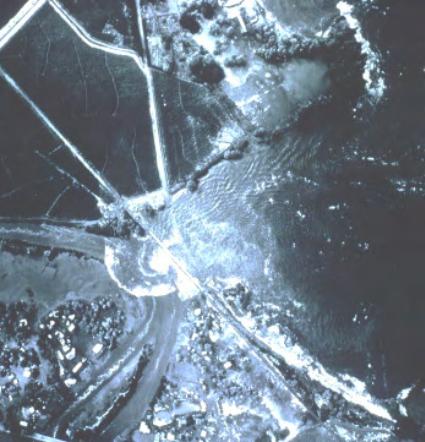


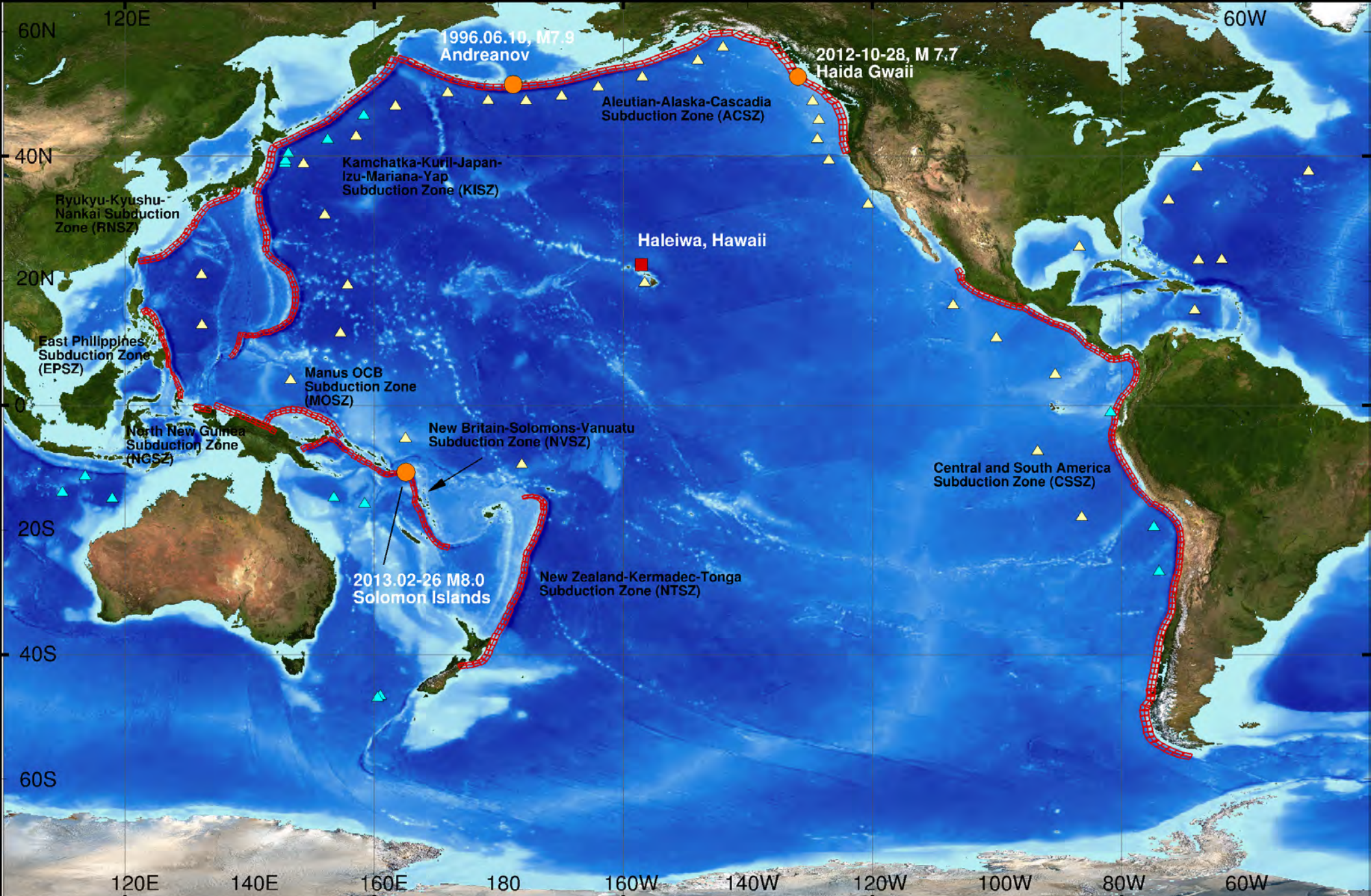
Tide gauge in Haleiwa harbor

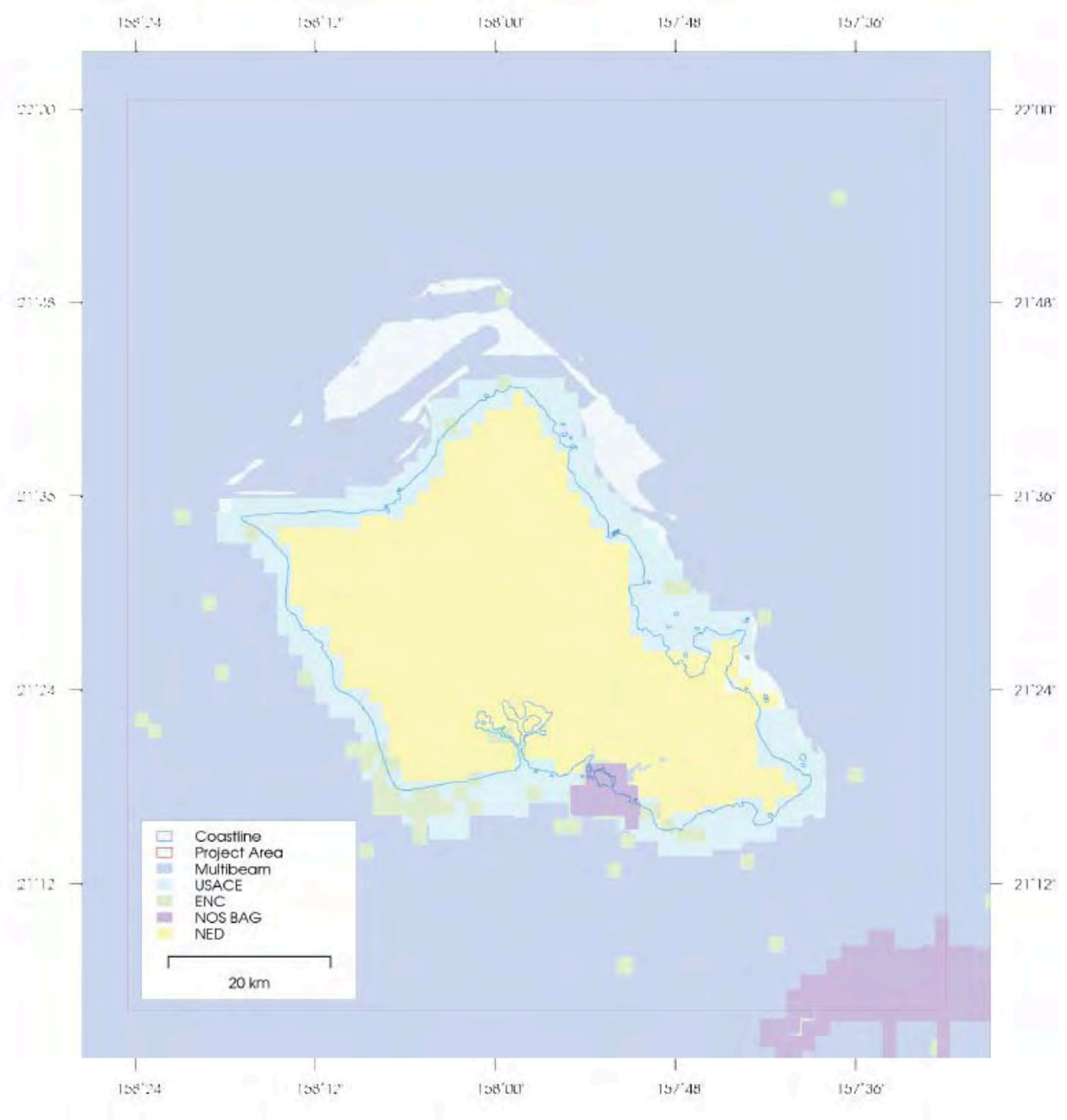
(c)

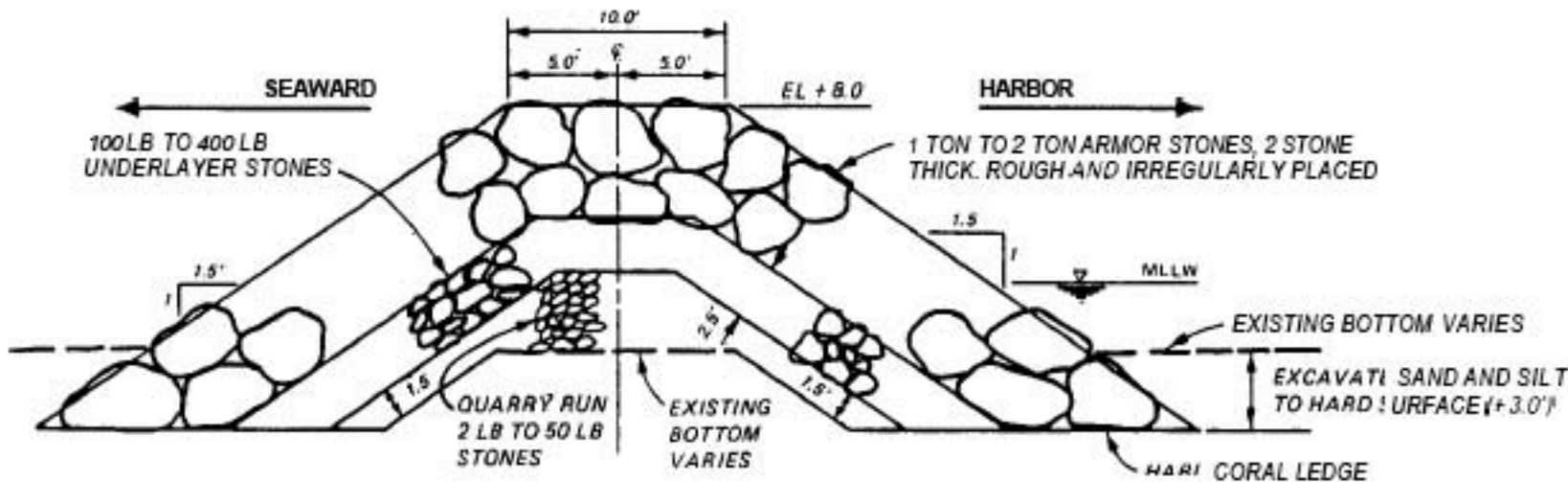


A-35, April 1, 1946. Haleiwa, Waialua Bay. This aerial photograph taken on the morning of the wave indicates only light damage. Debris was found at 10 feet by the ground party. The beached boats suffered no significant damage.

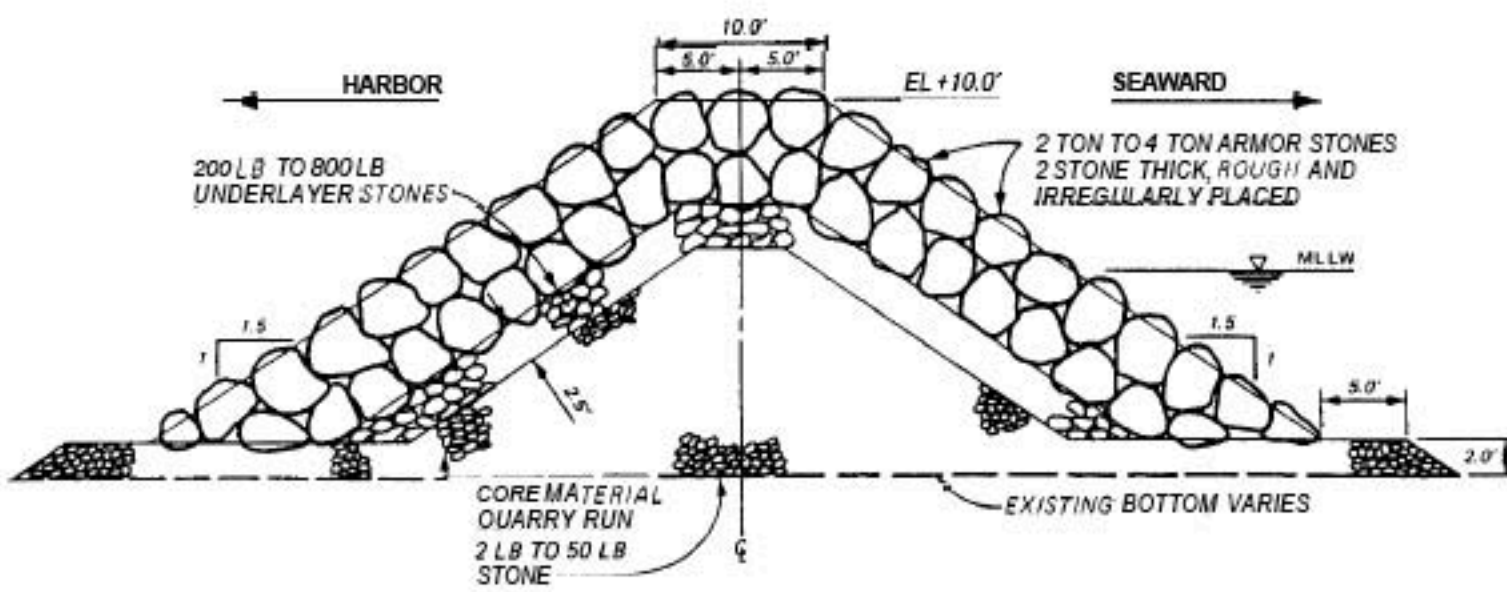




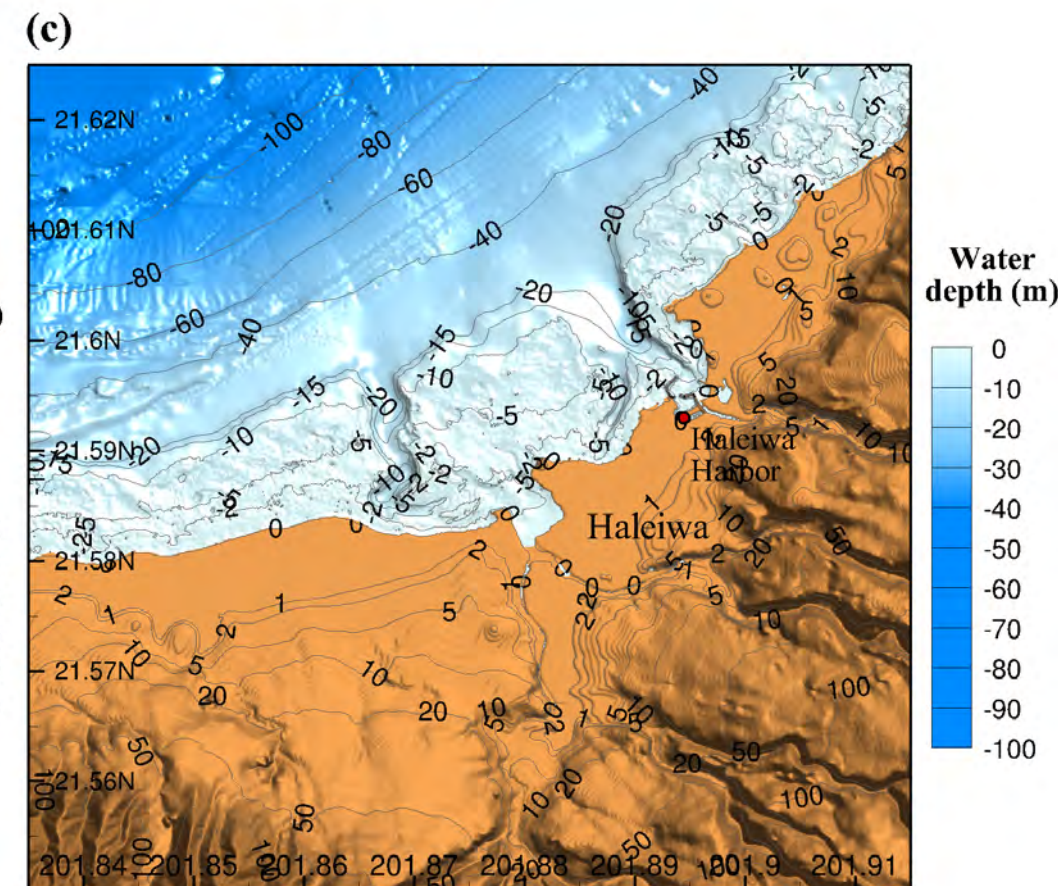
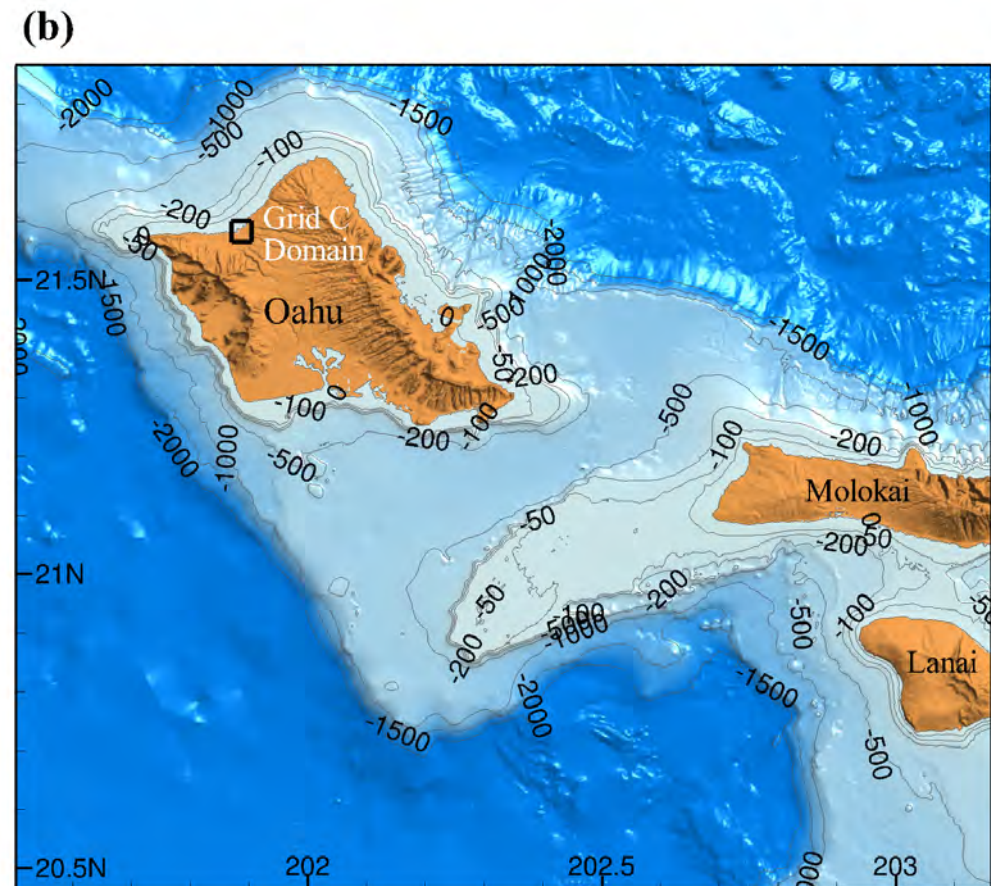
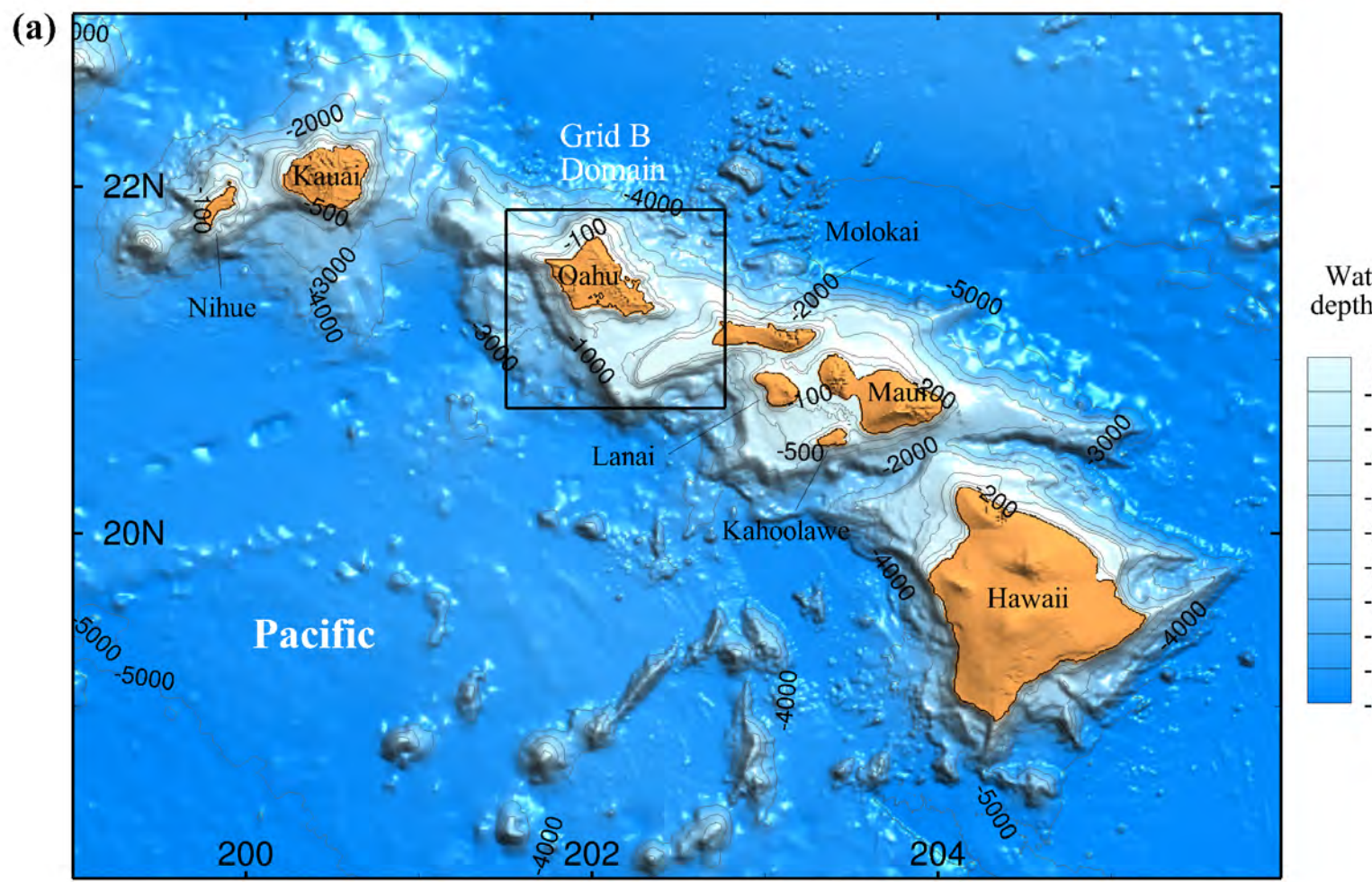


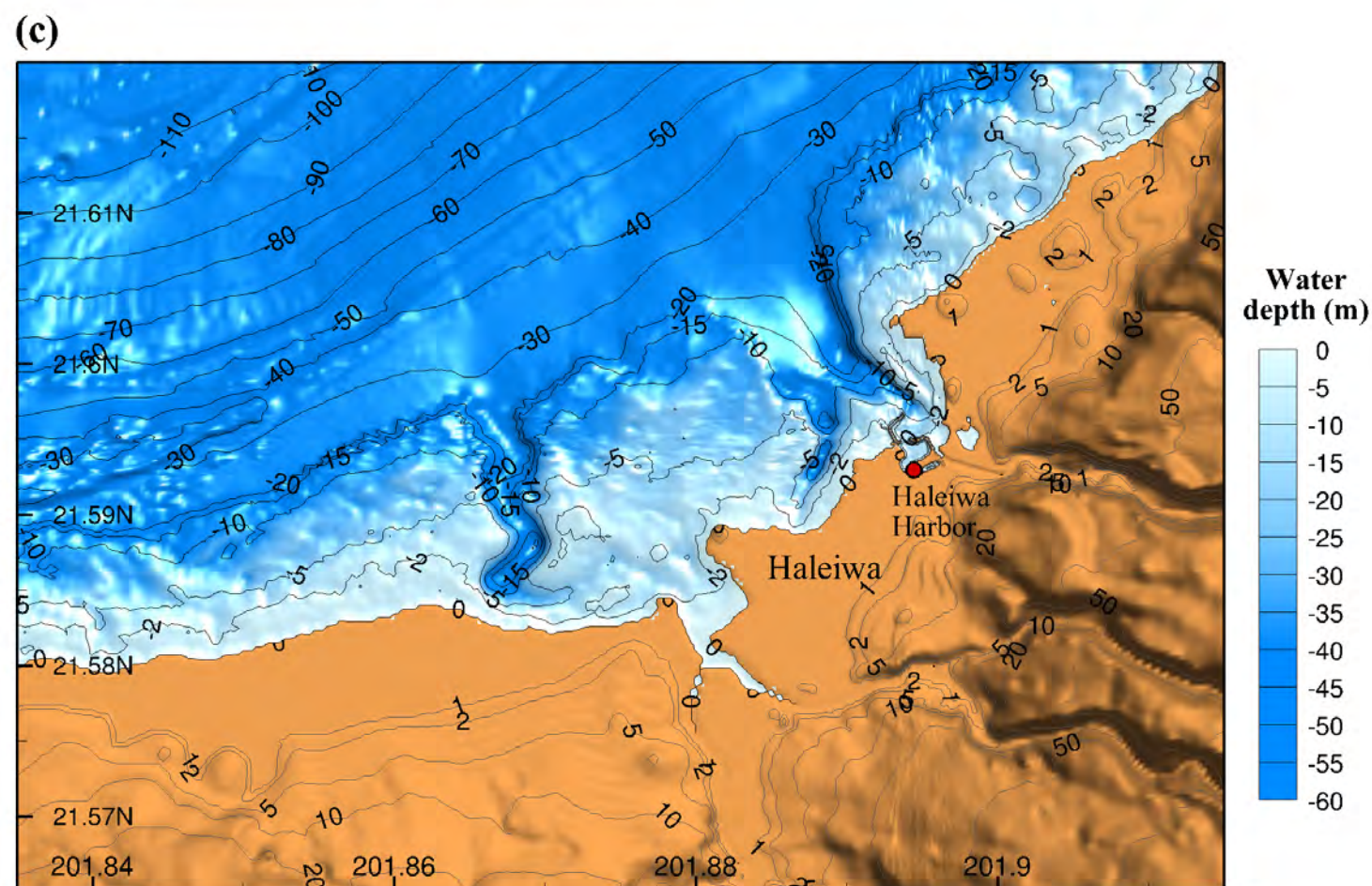
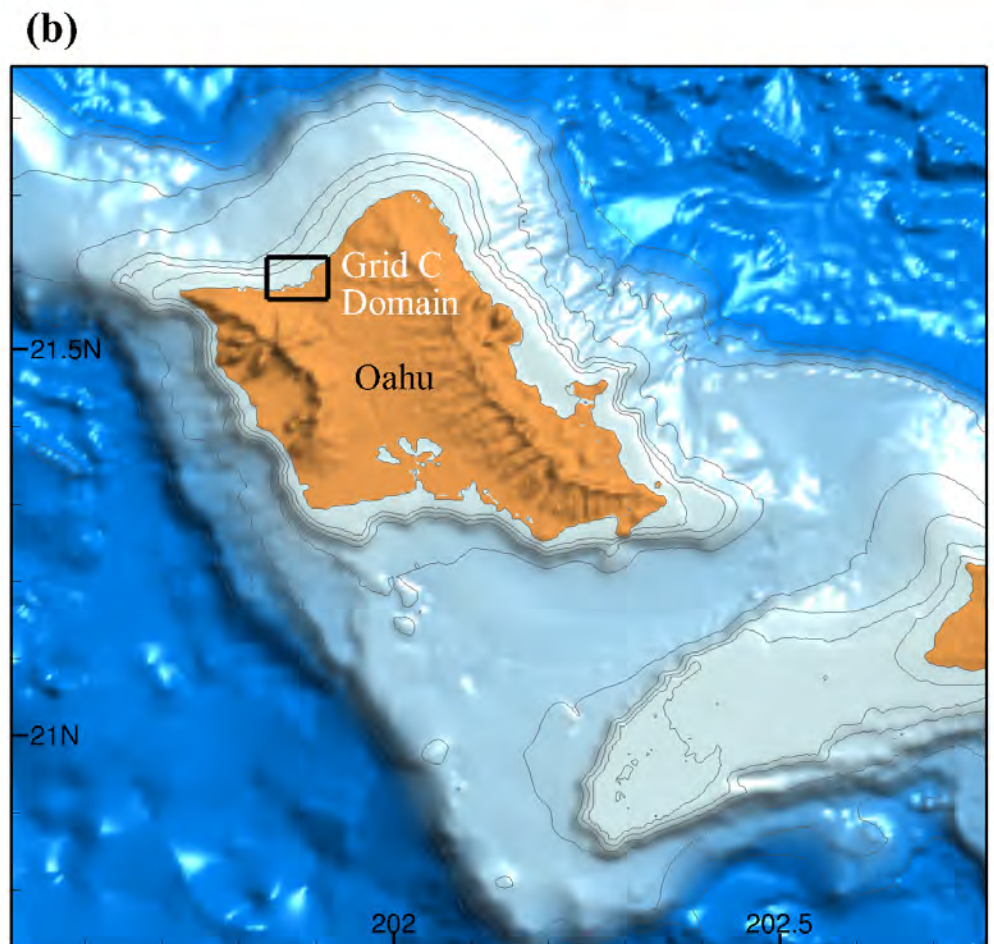
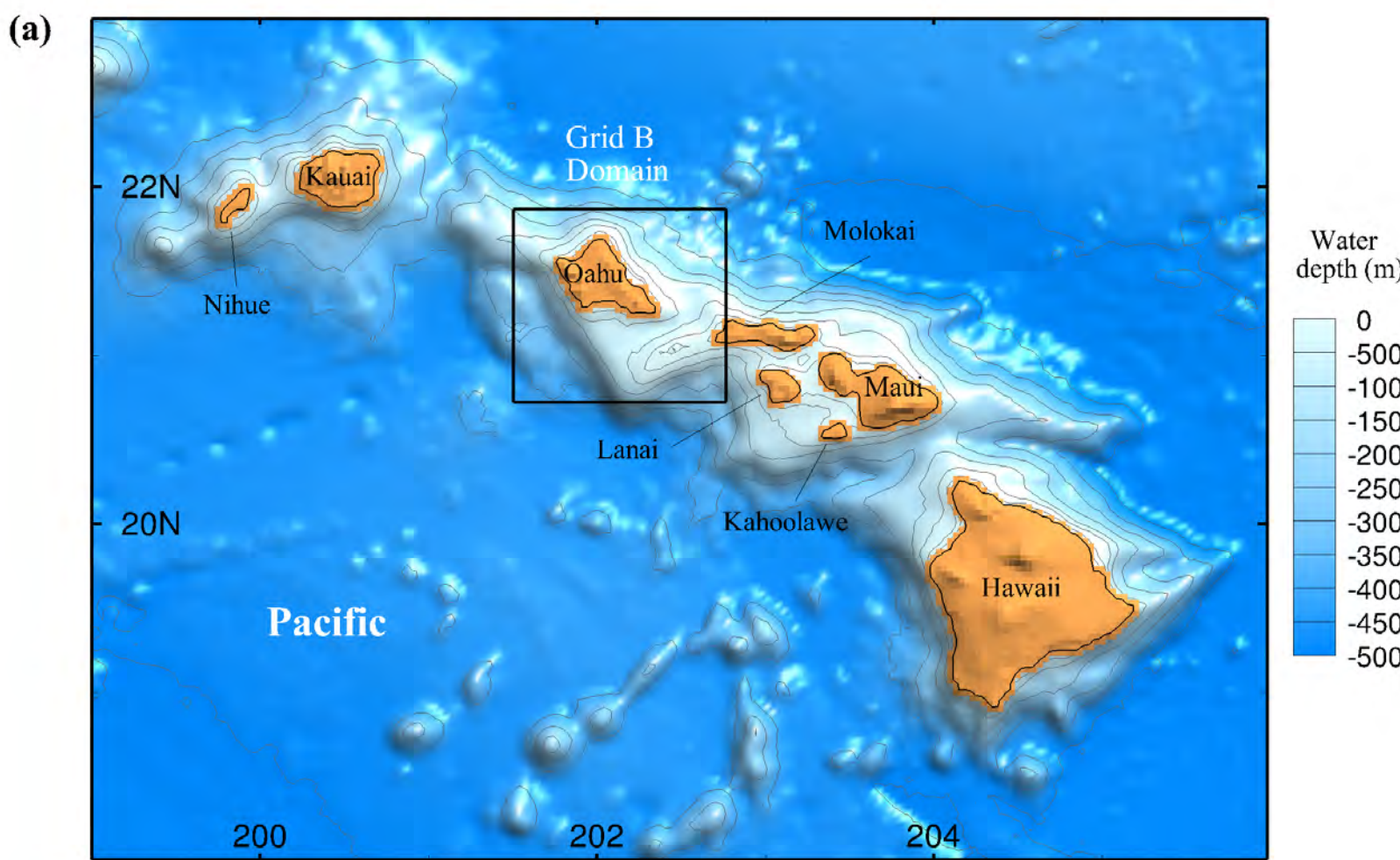


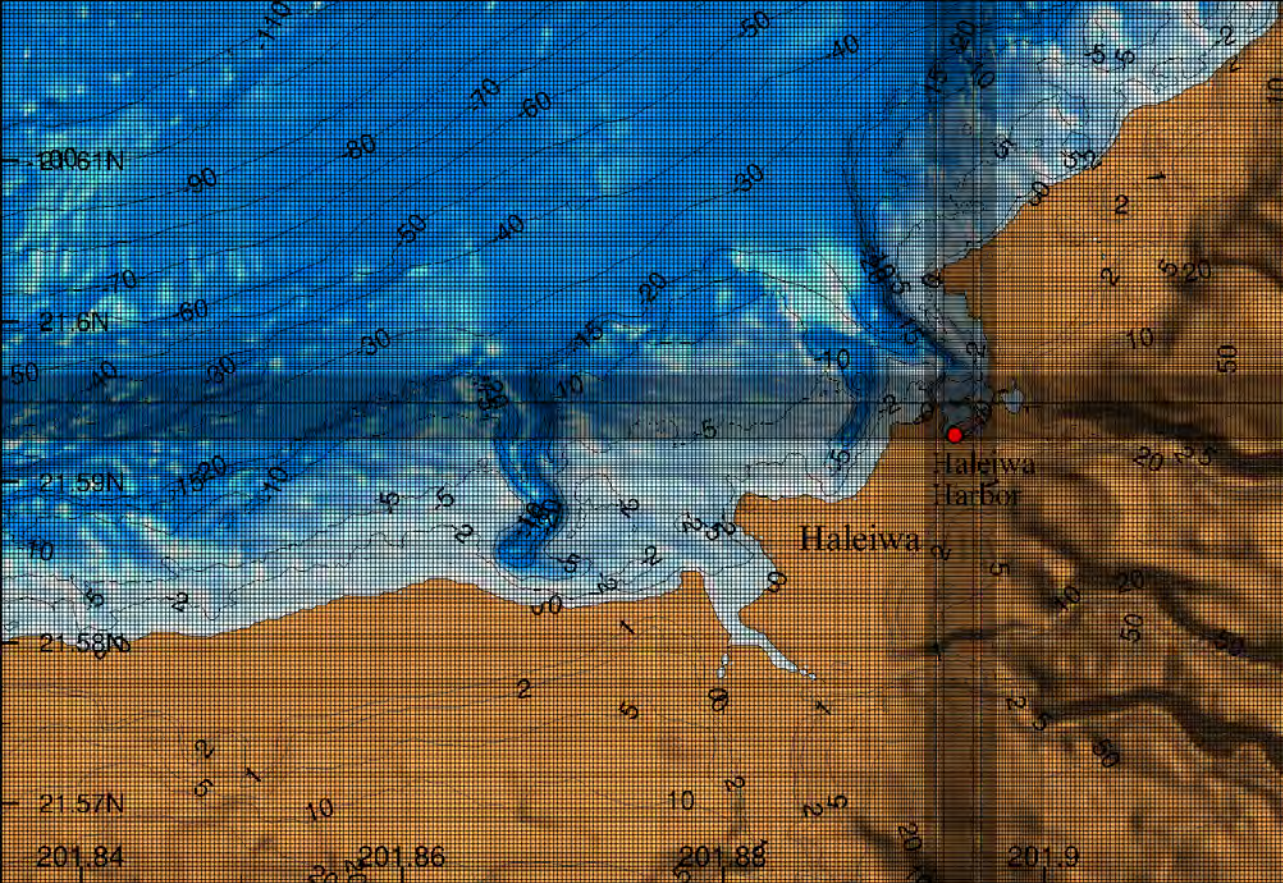
EO BREAKWATER SECTION
STA 0+05 TO STA 0+80

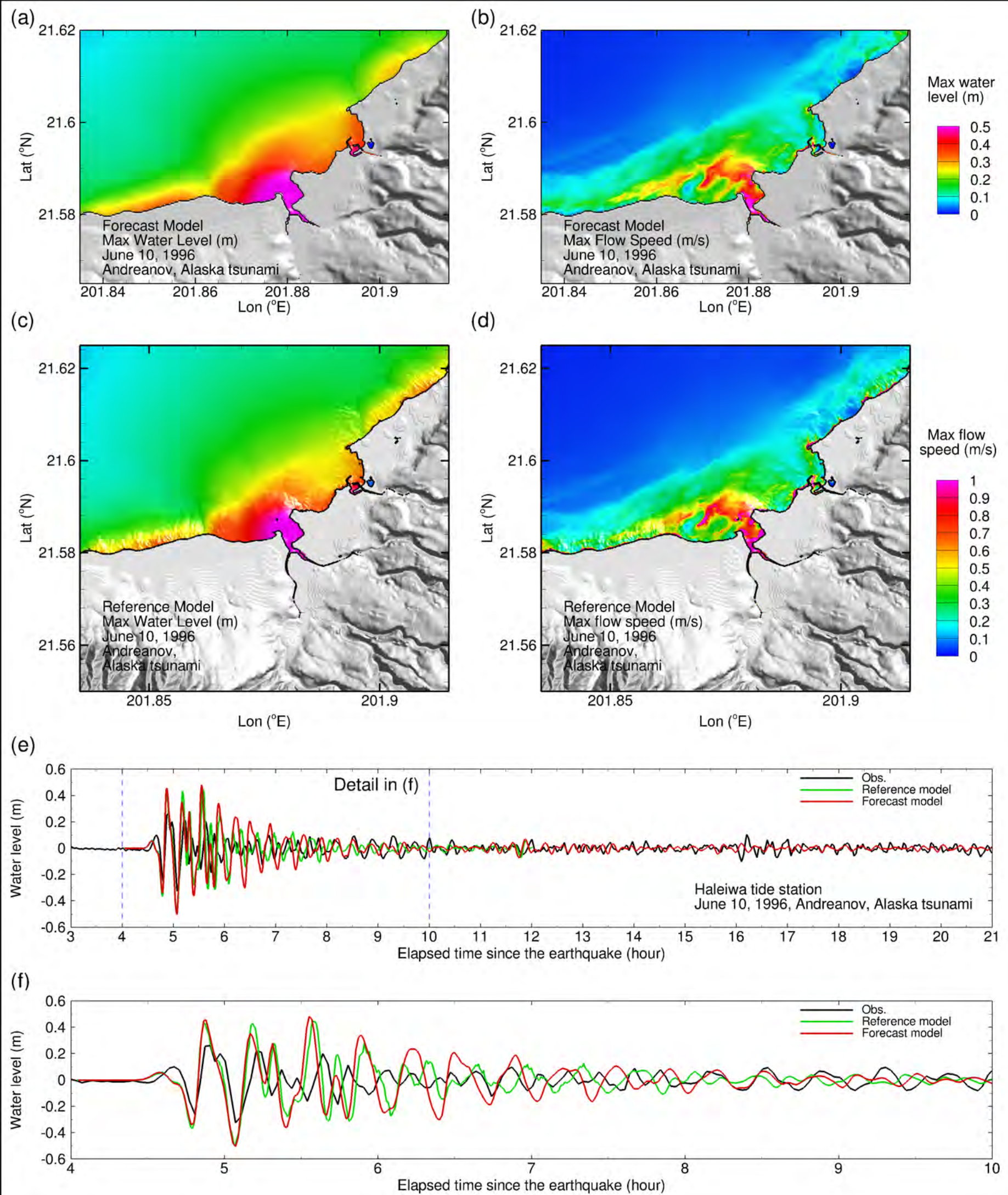


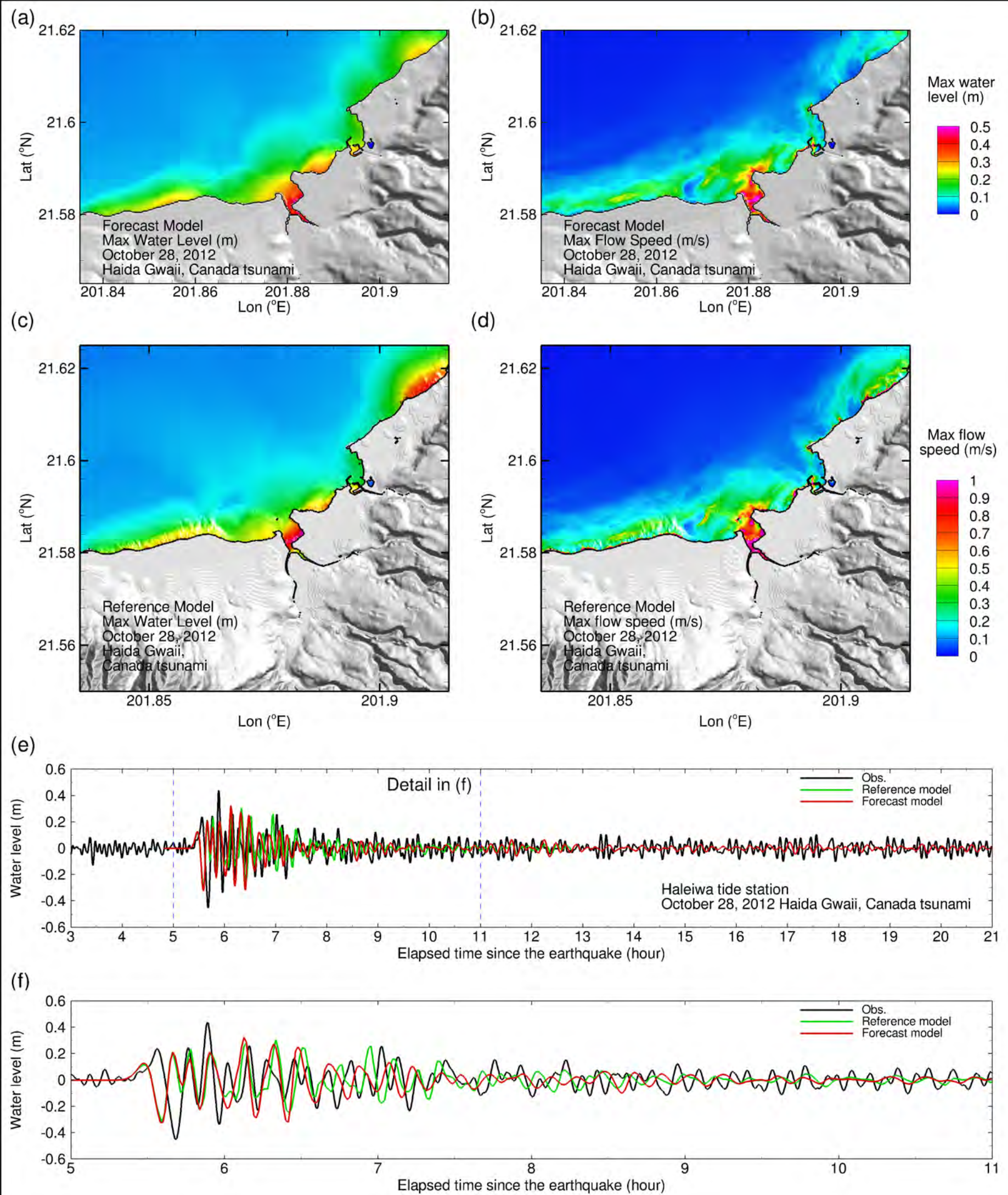
110° BREAKWATER SECTION
STA 12+00 TO STA 13+10

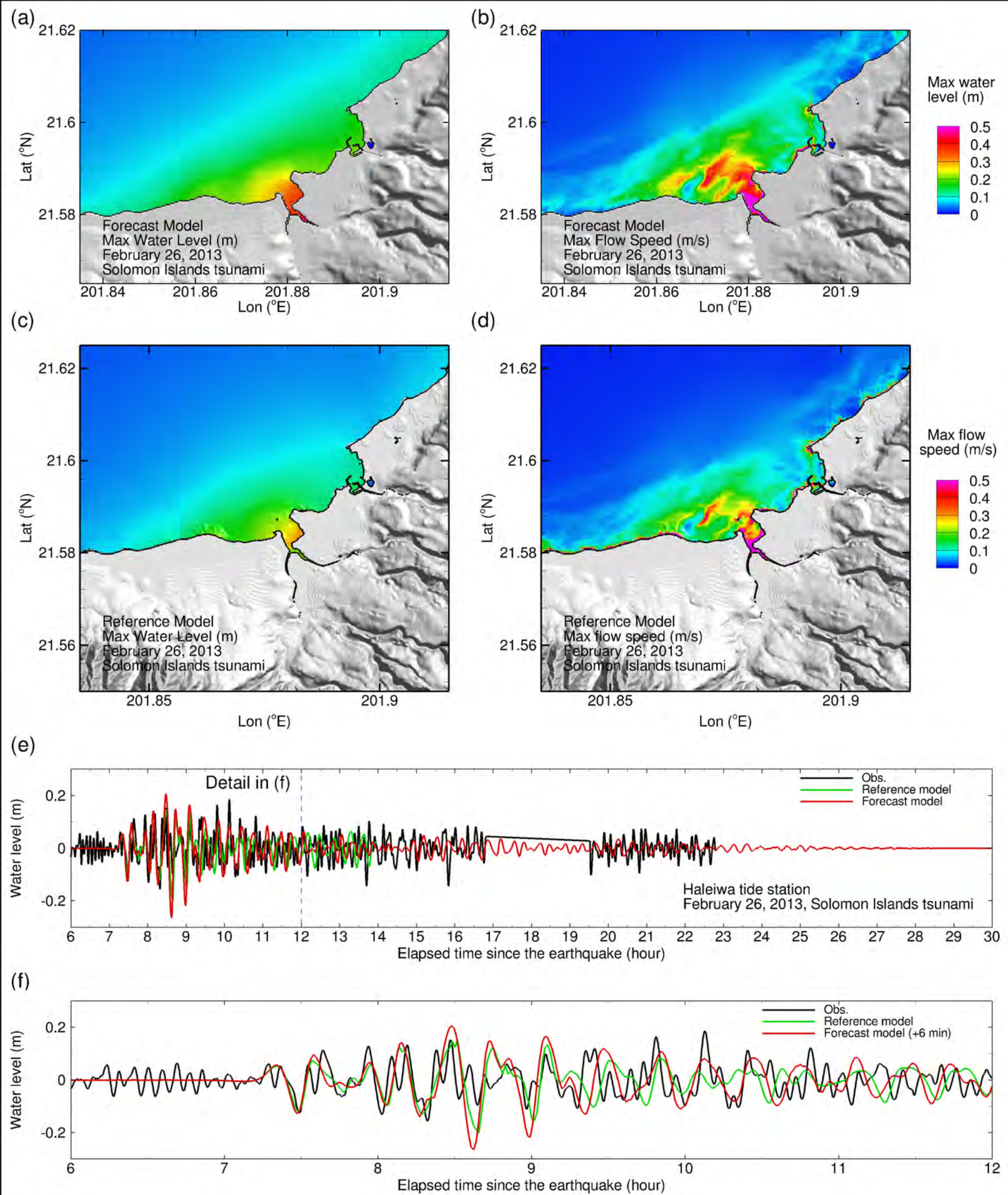


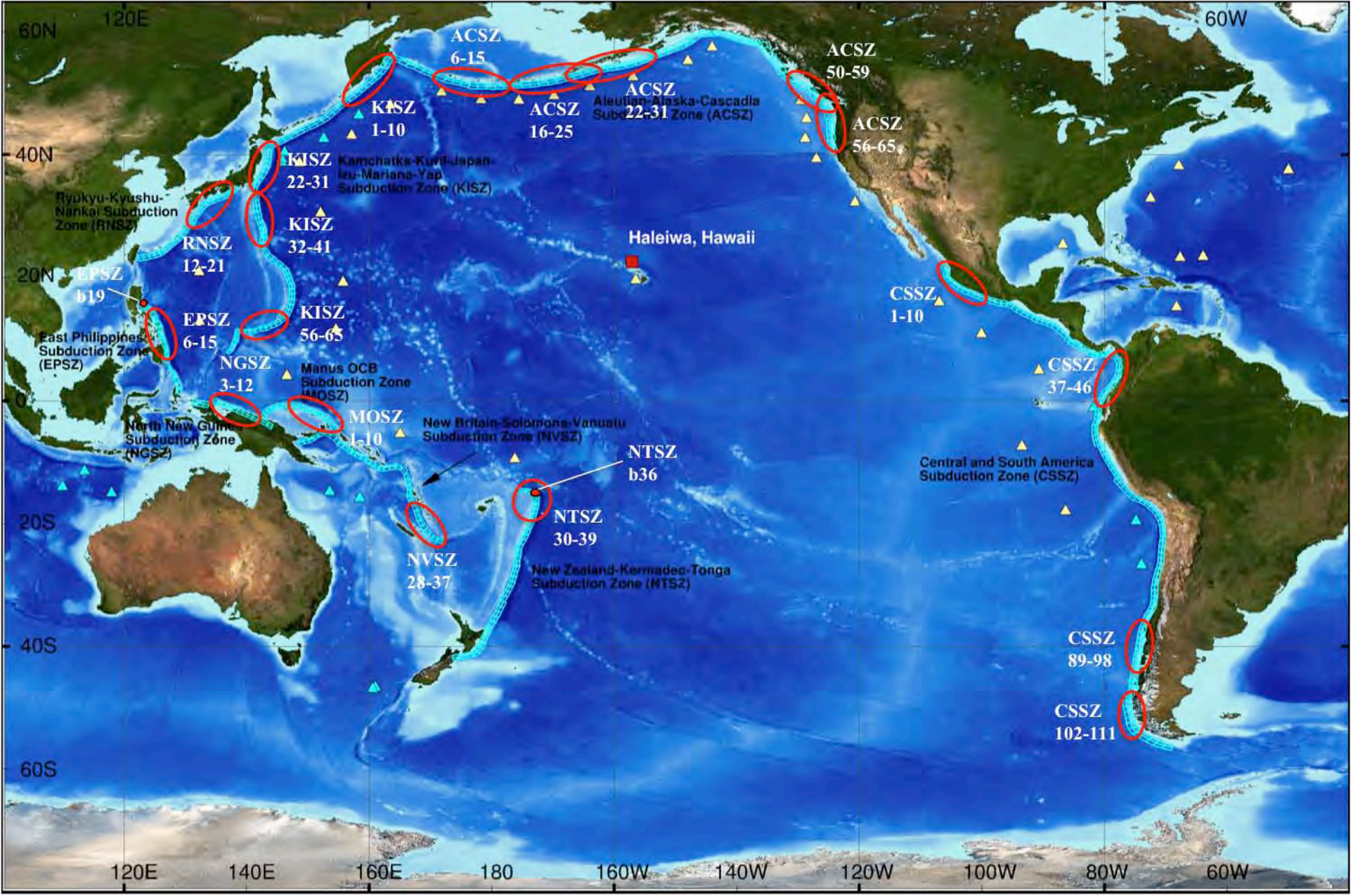


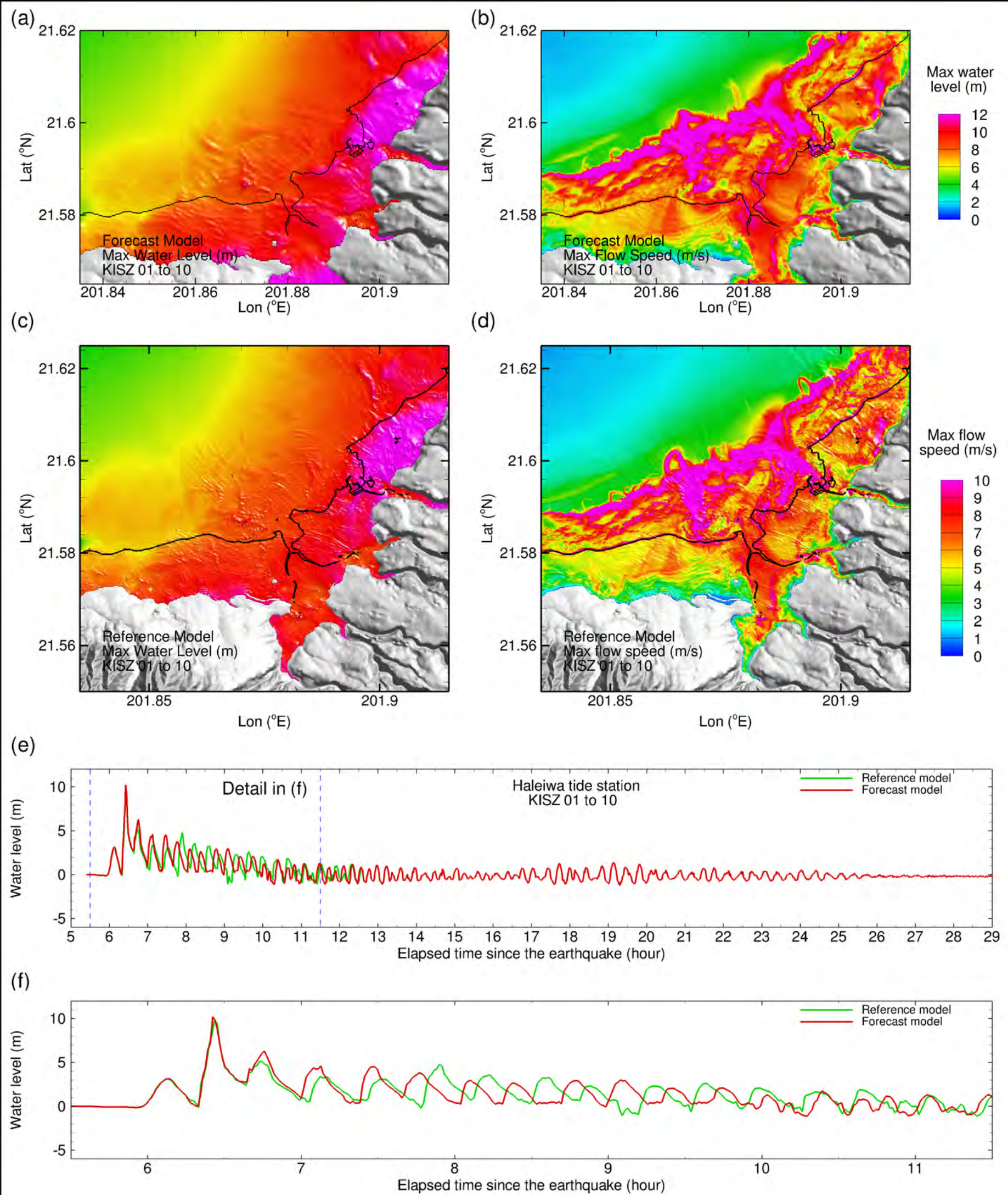


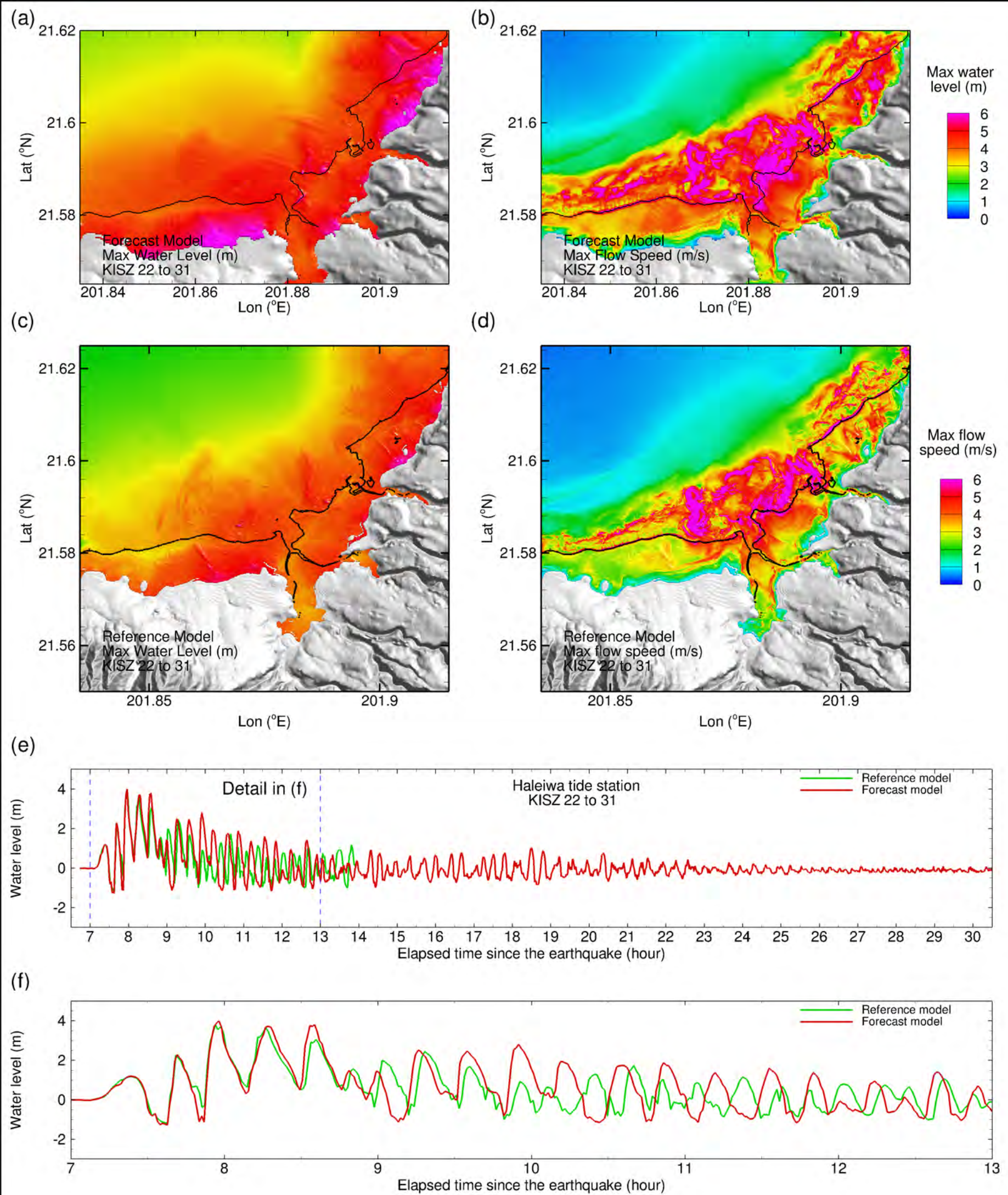


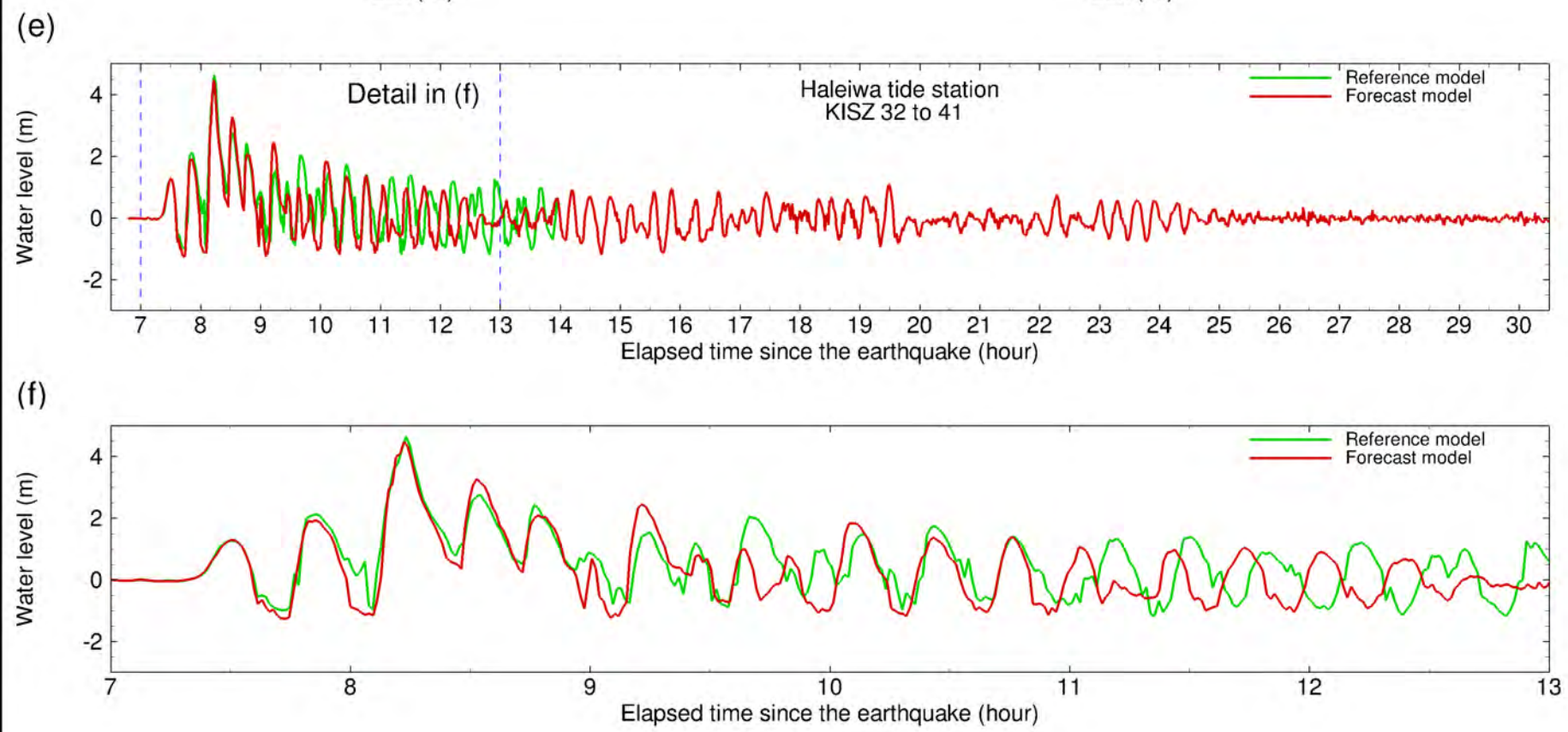
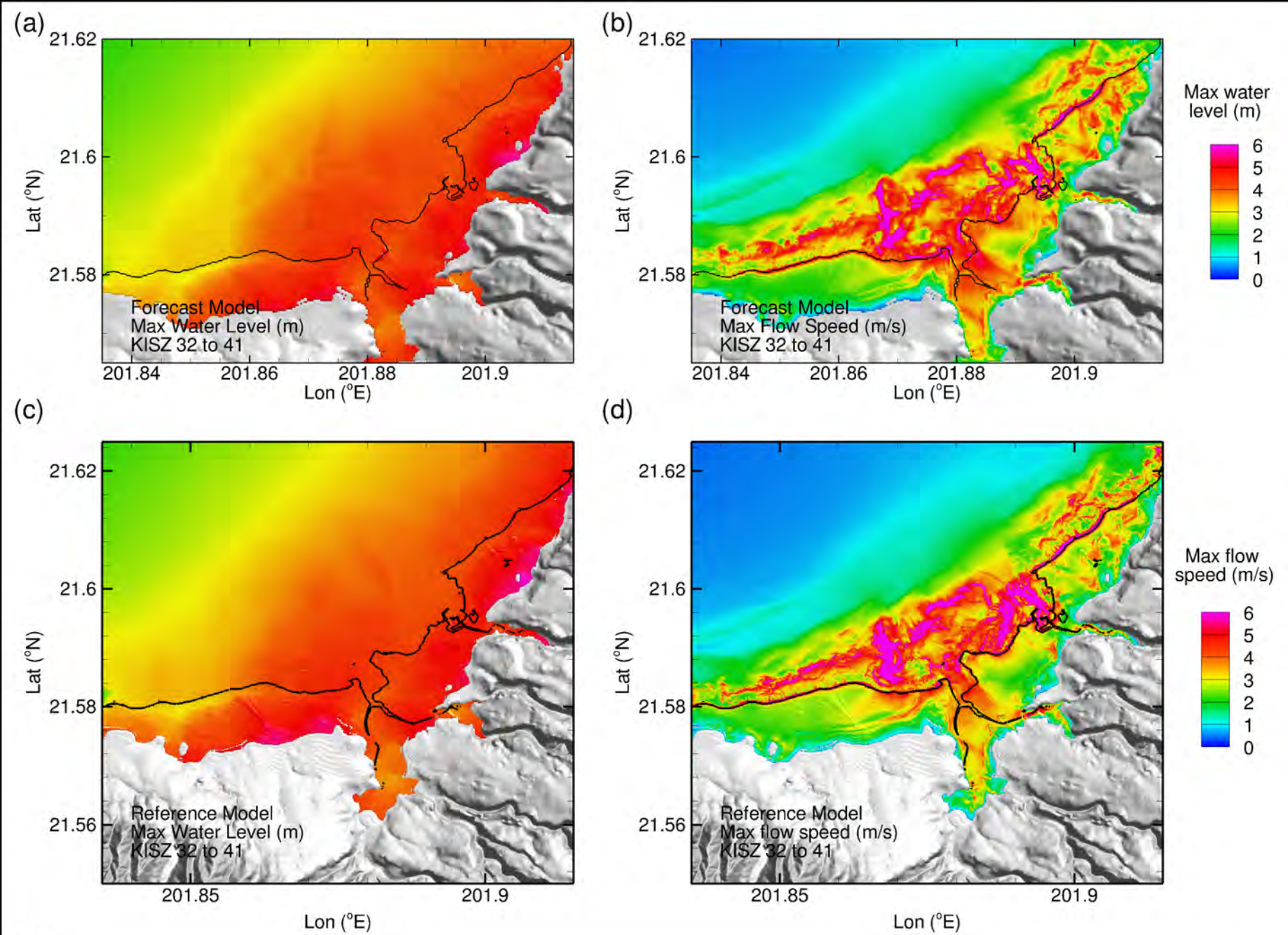


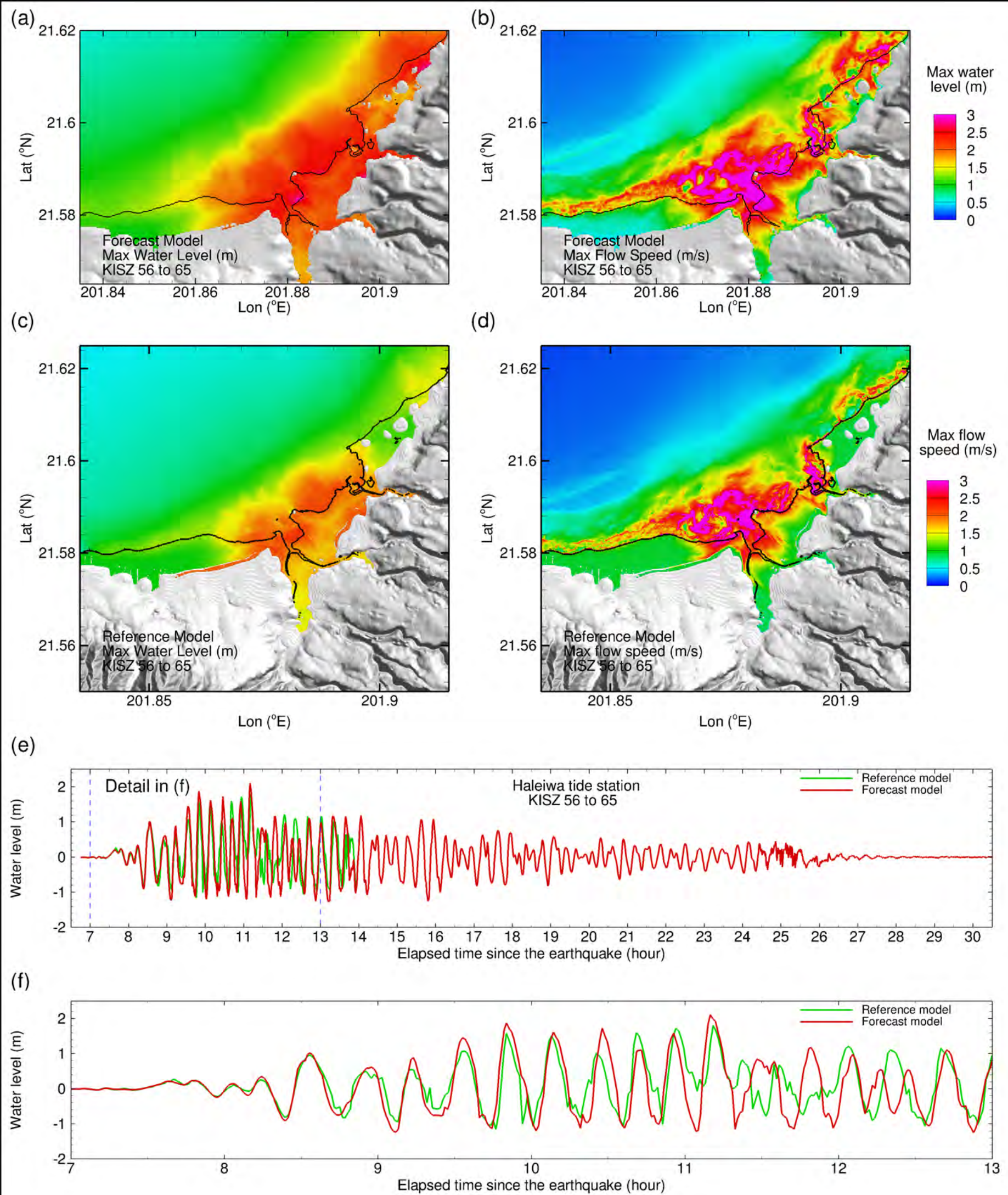


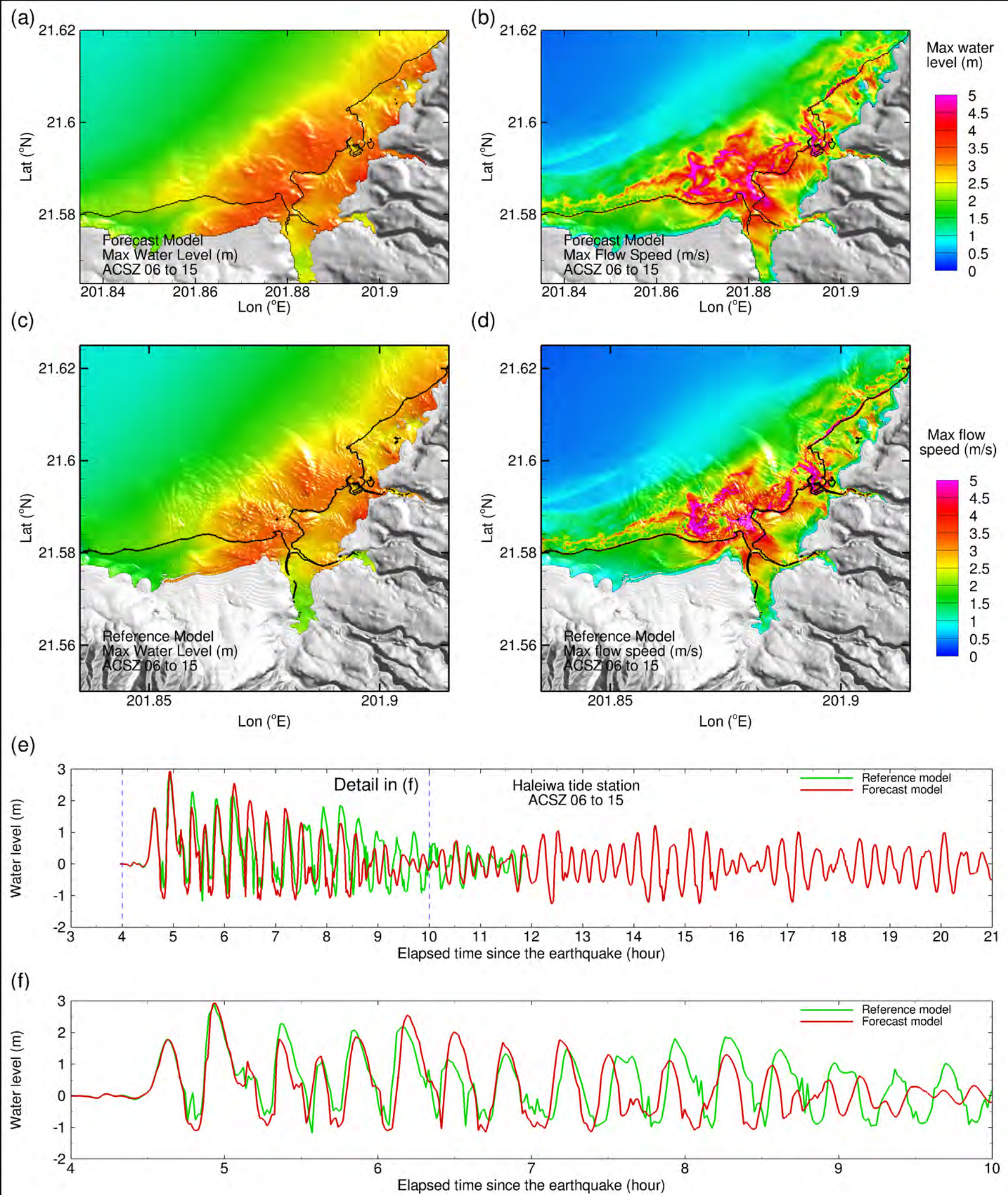


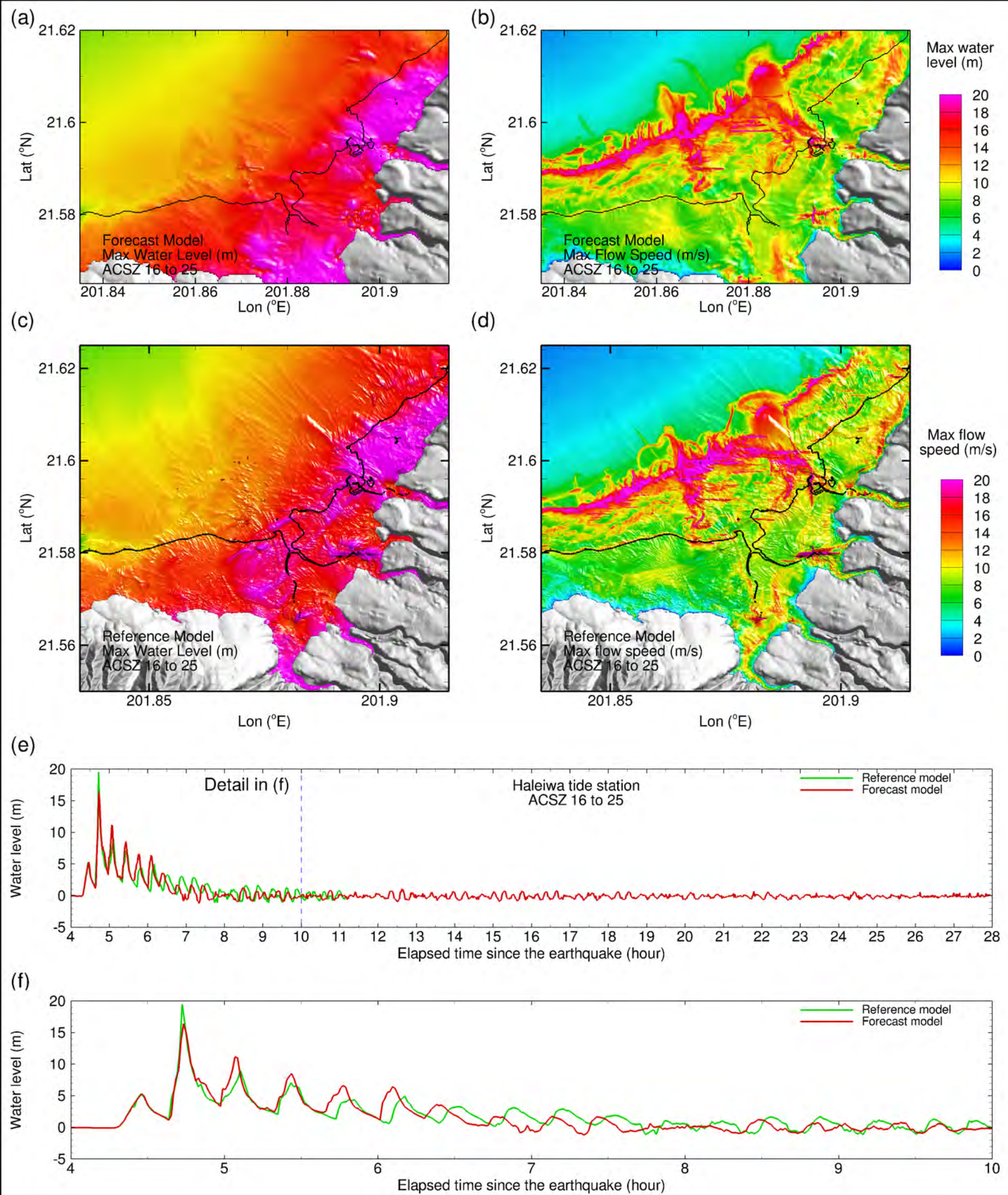


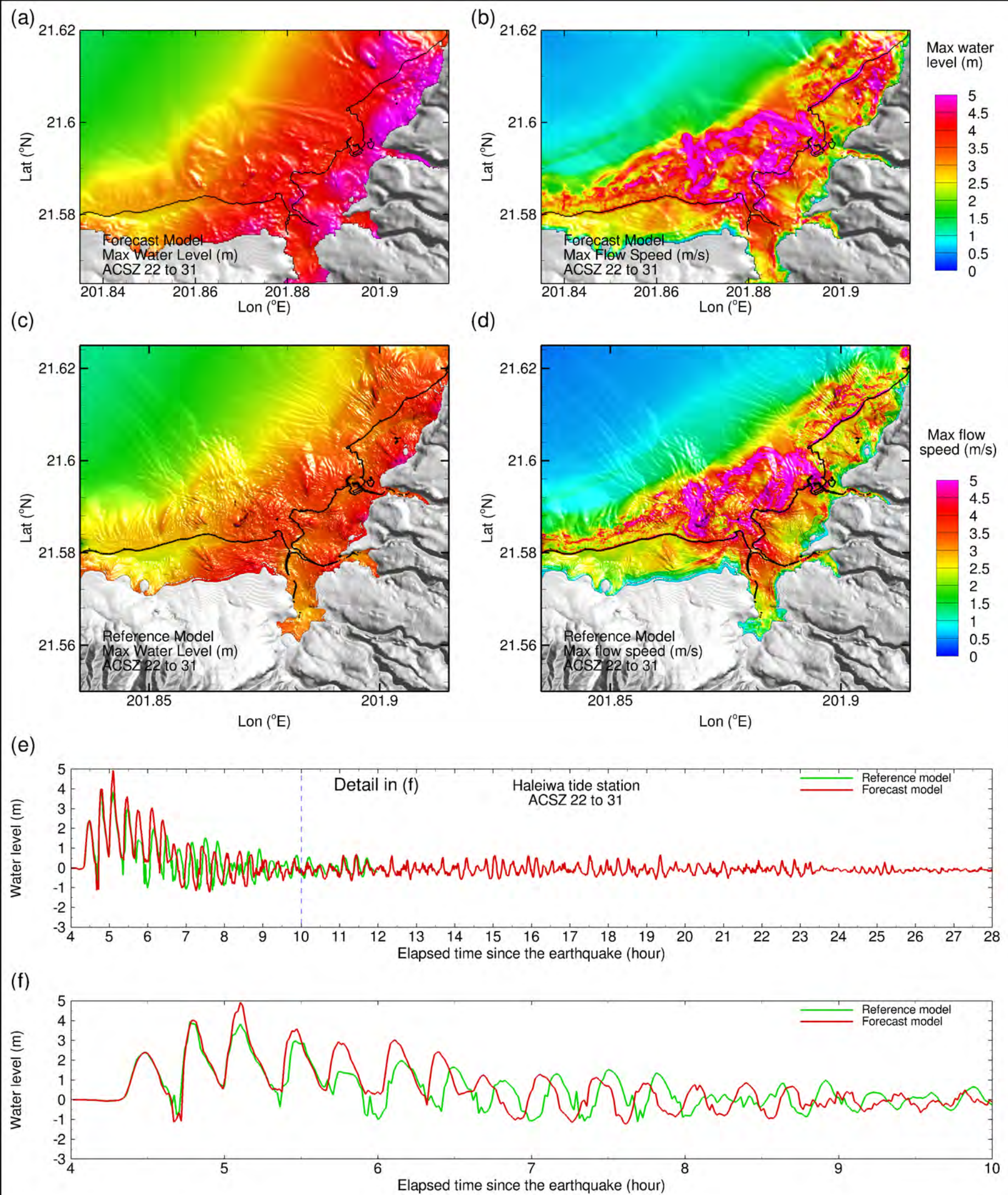


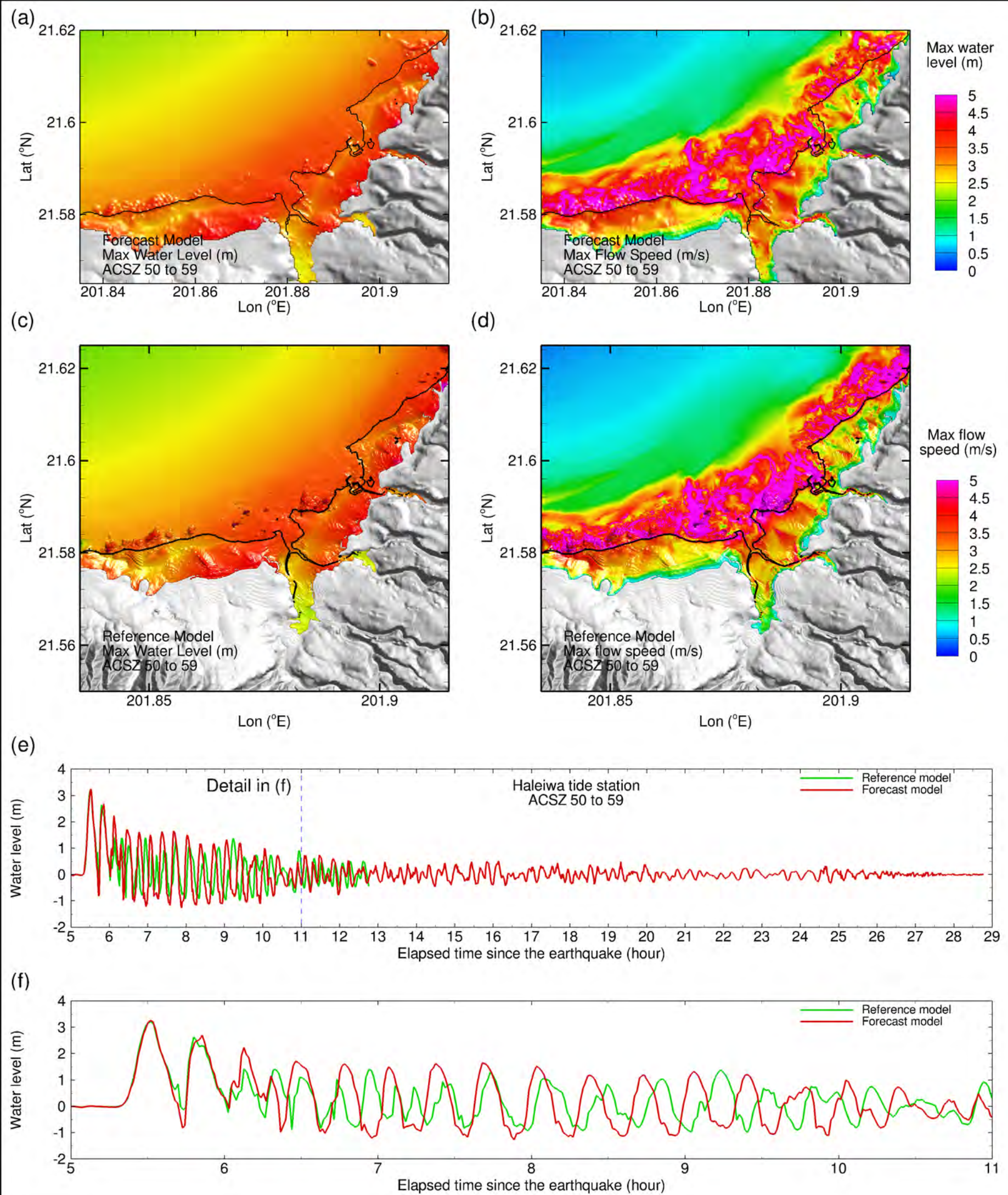


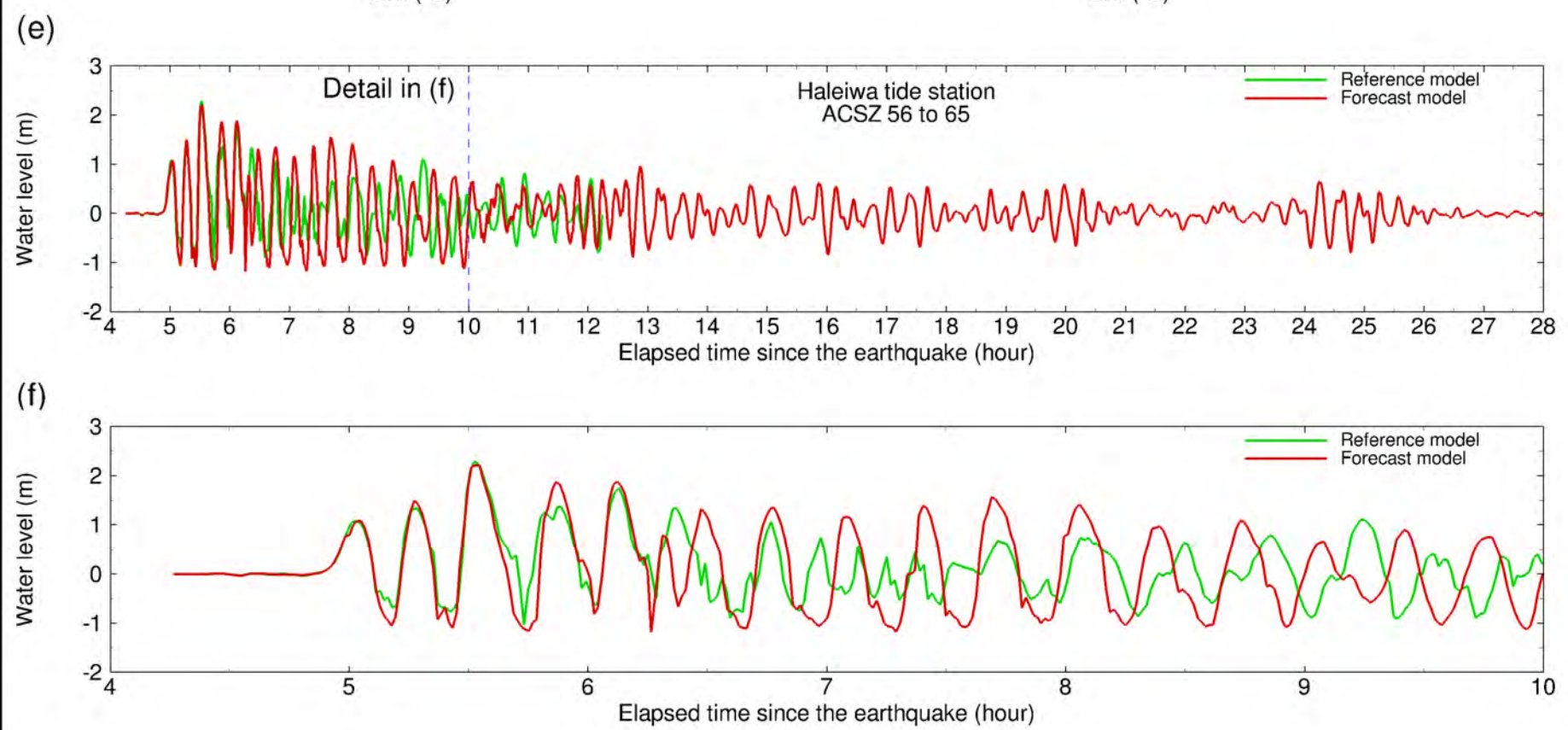
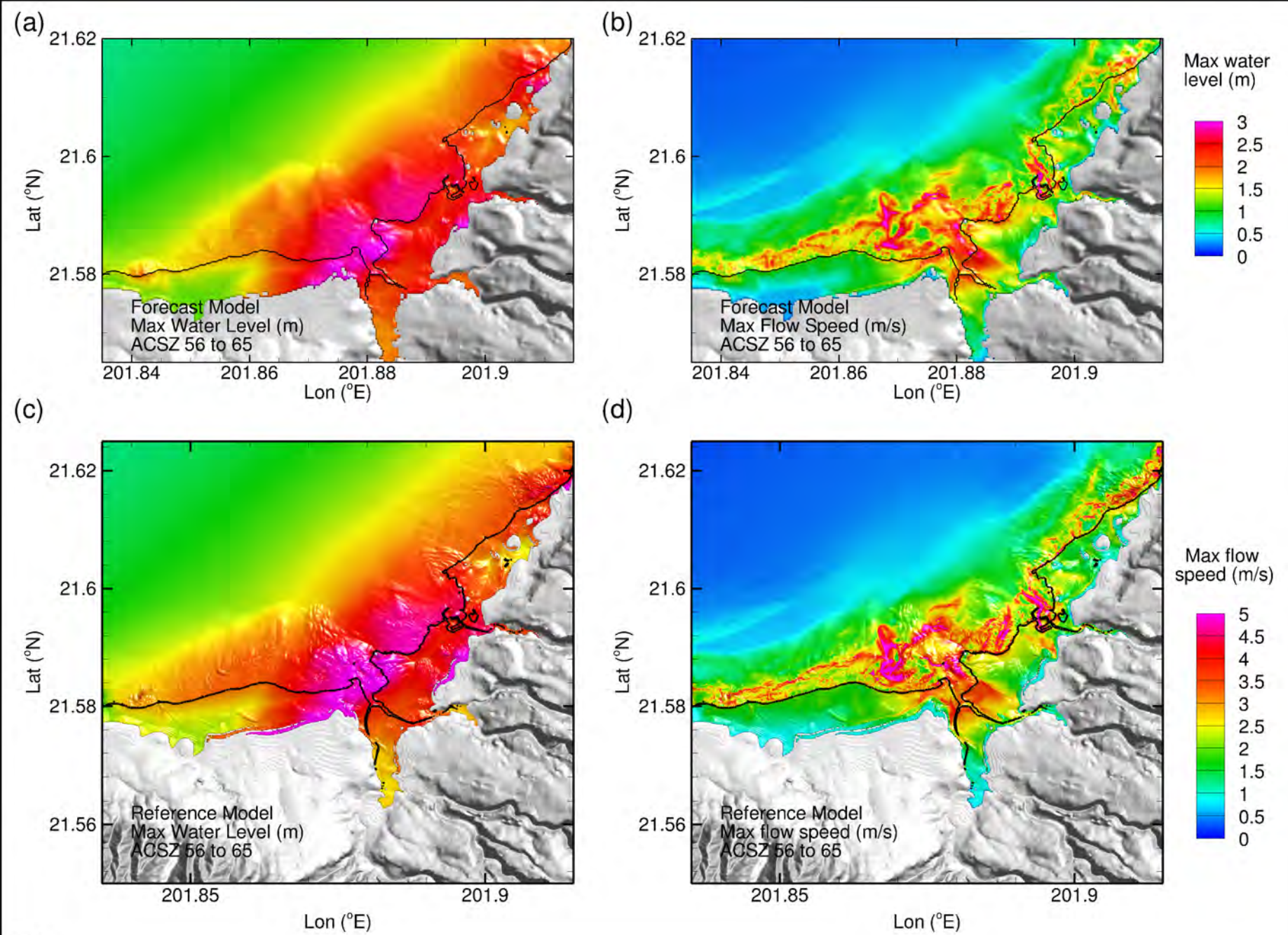


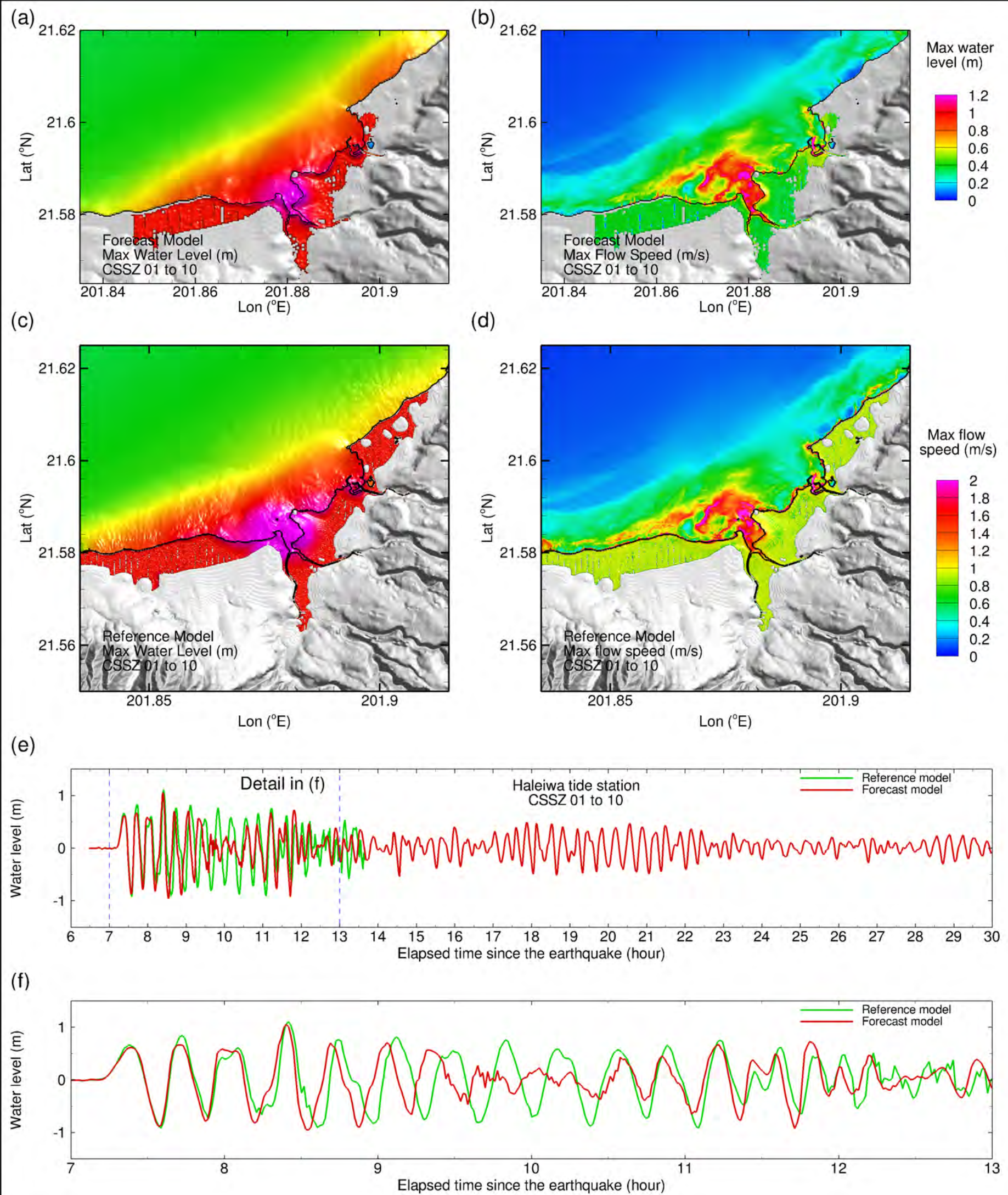


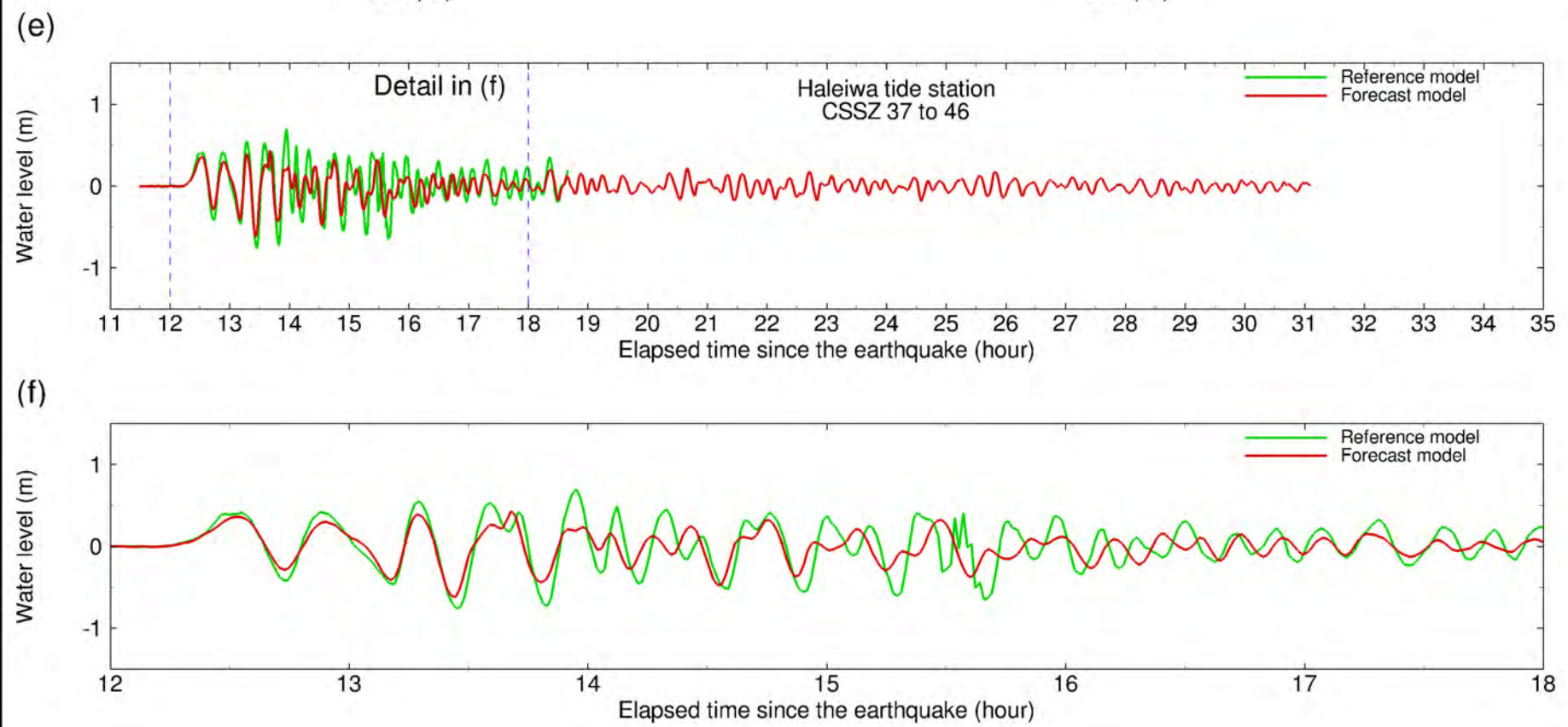
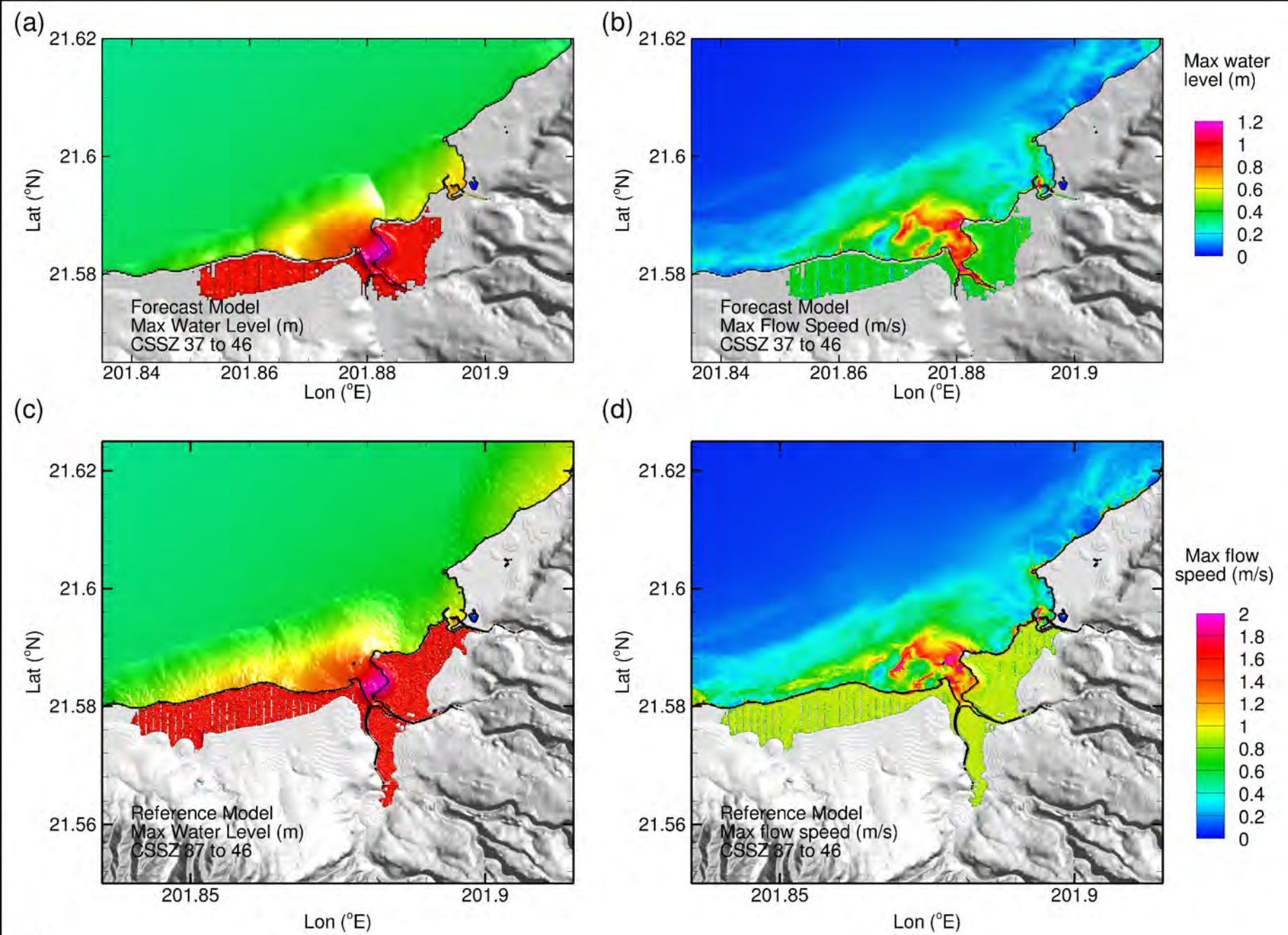


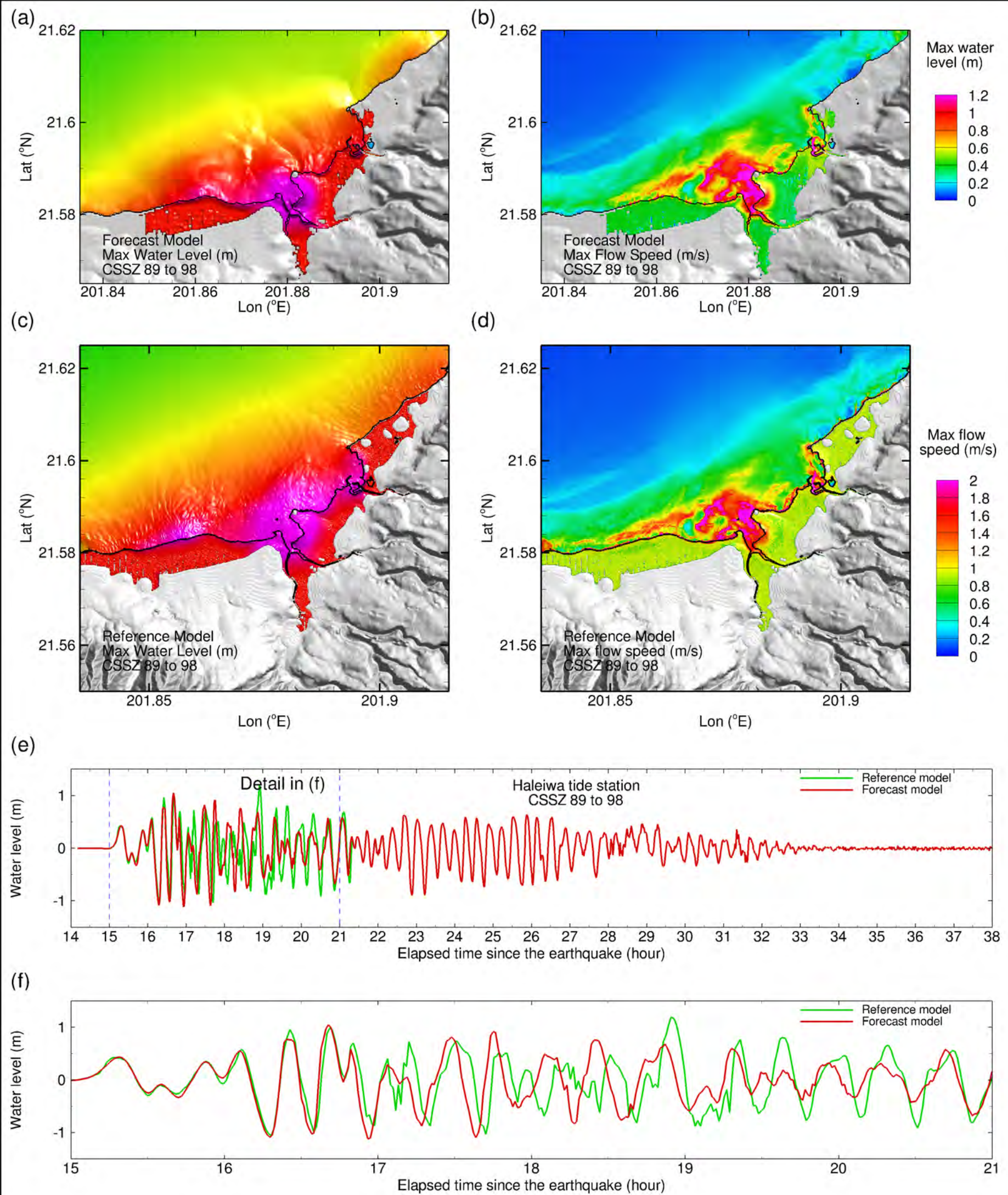


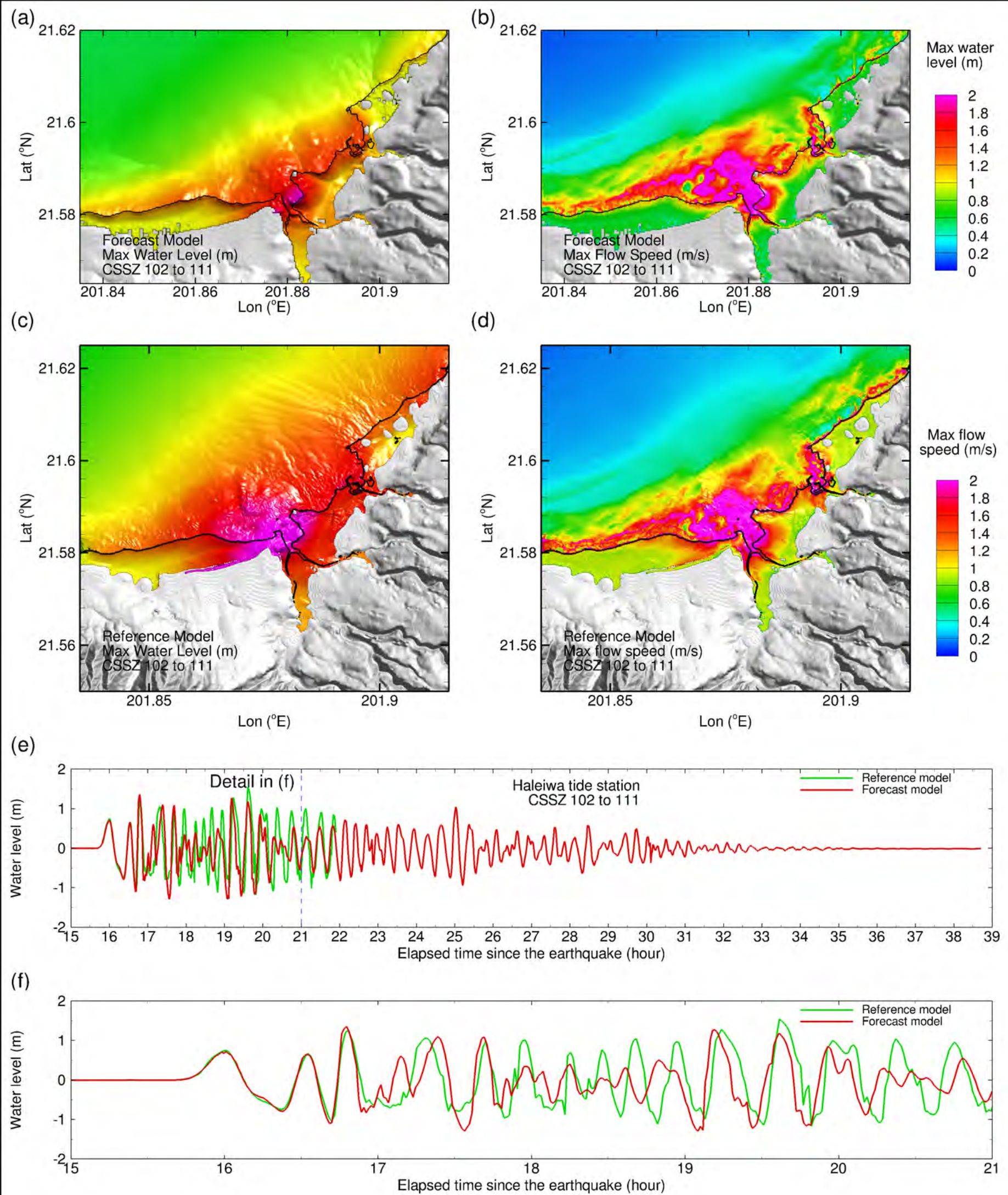


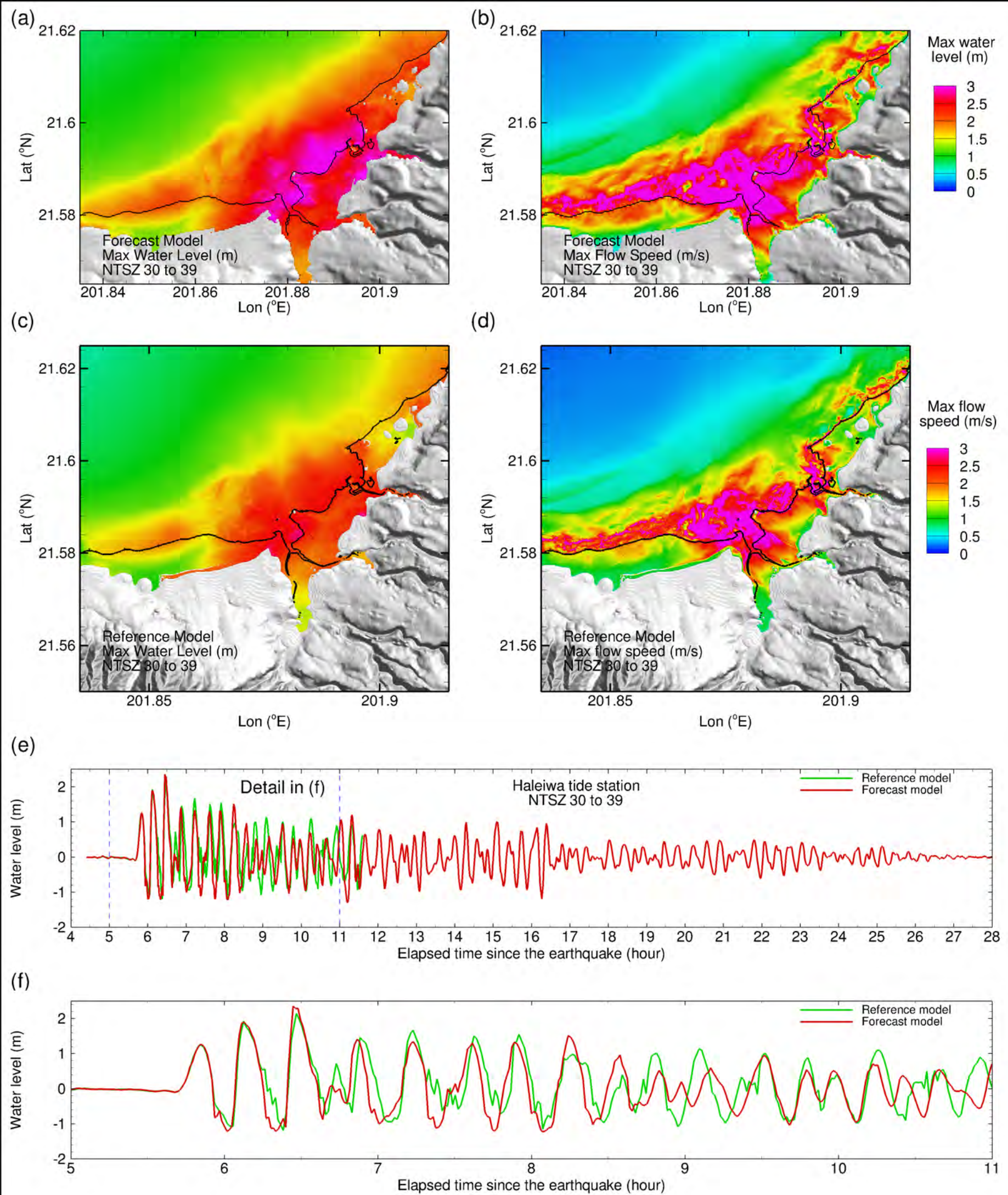


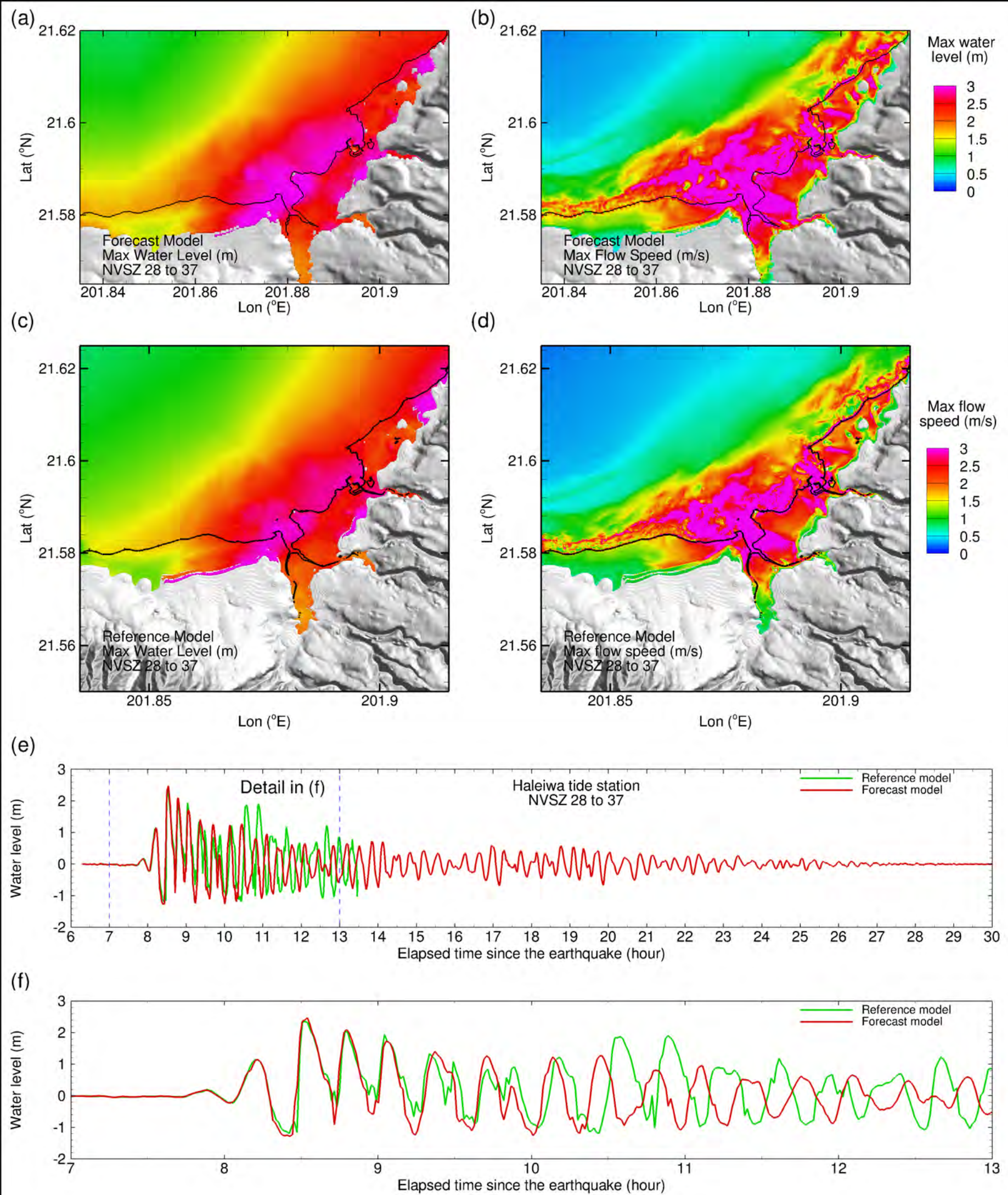


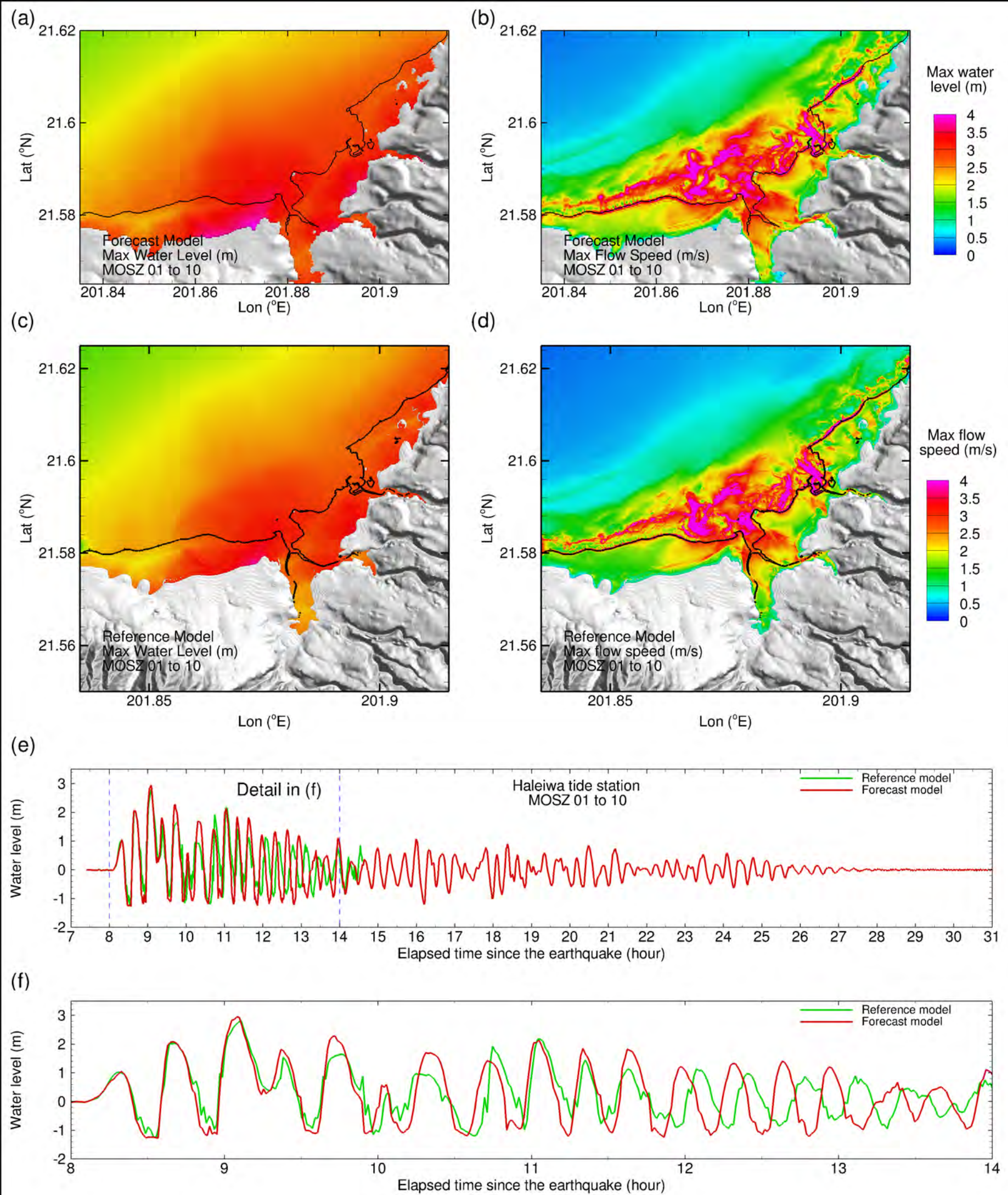


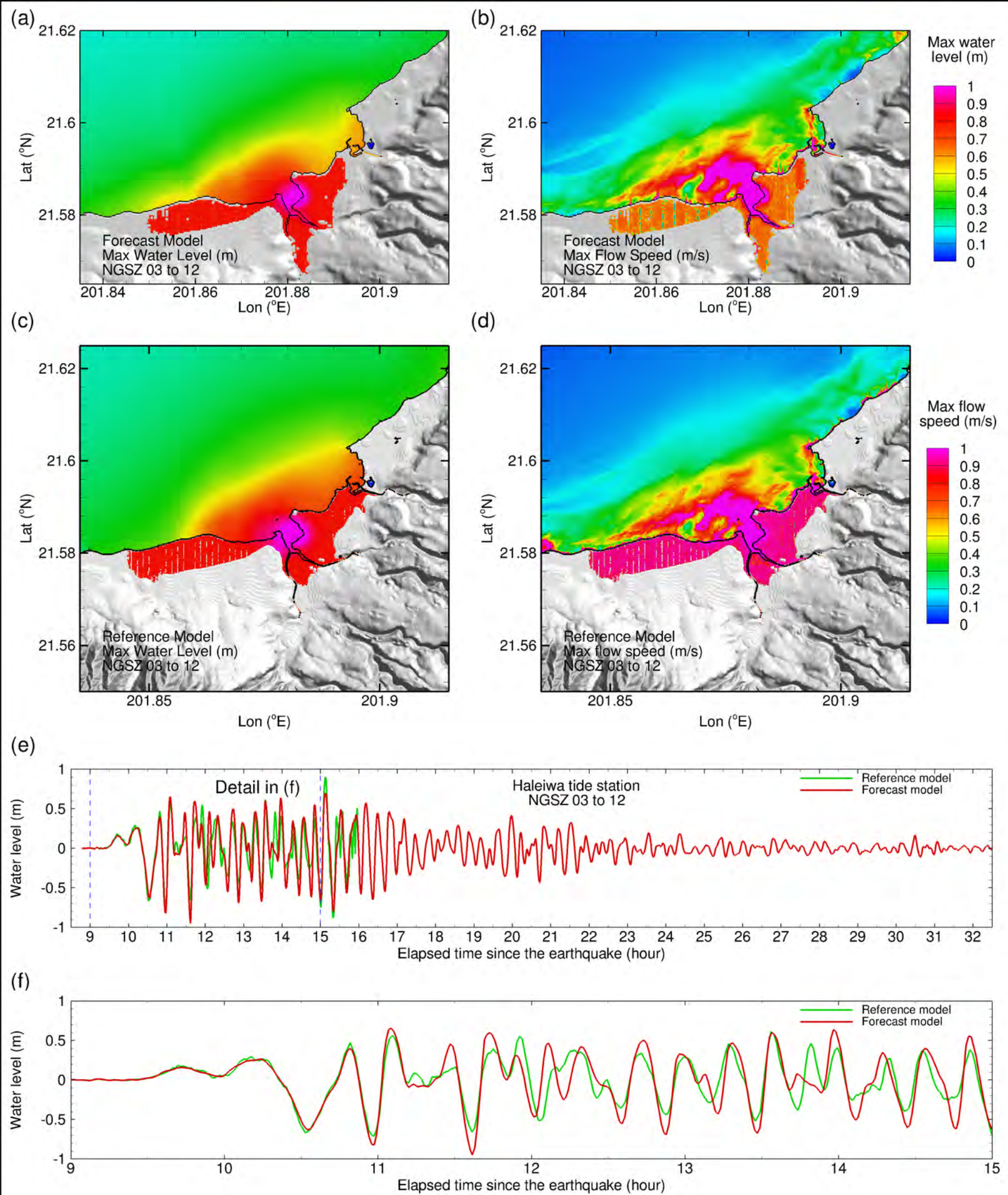


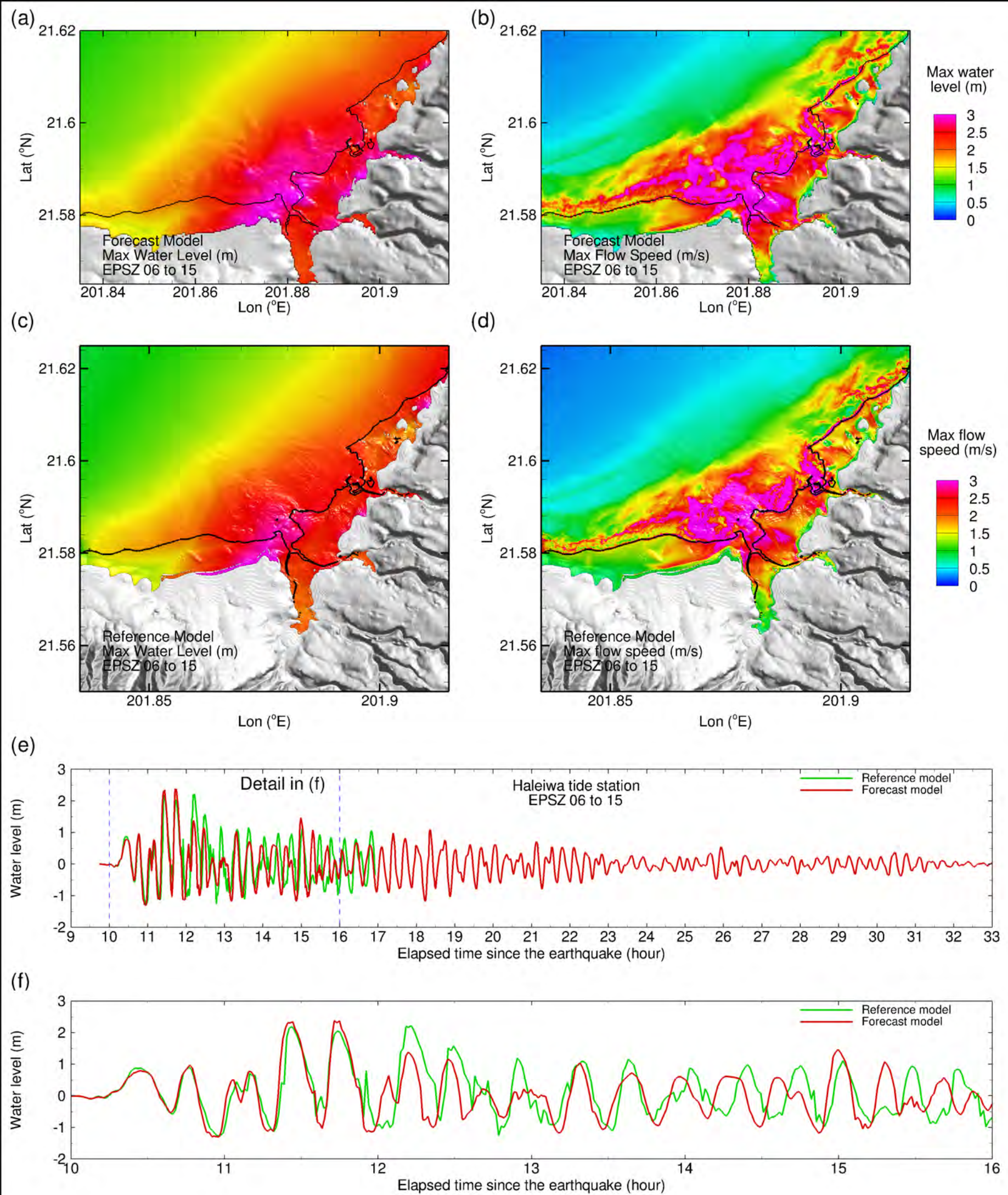


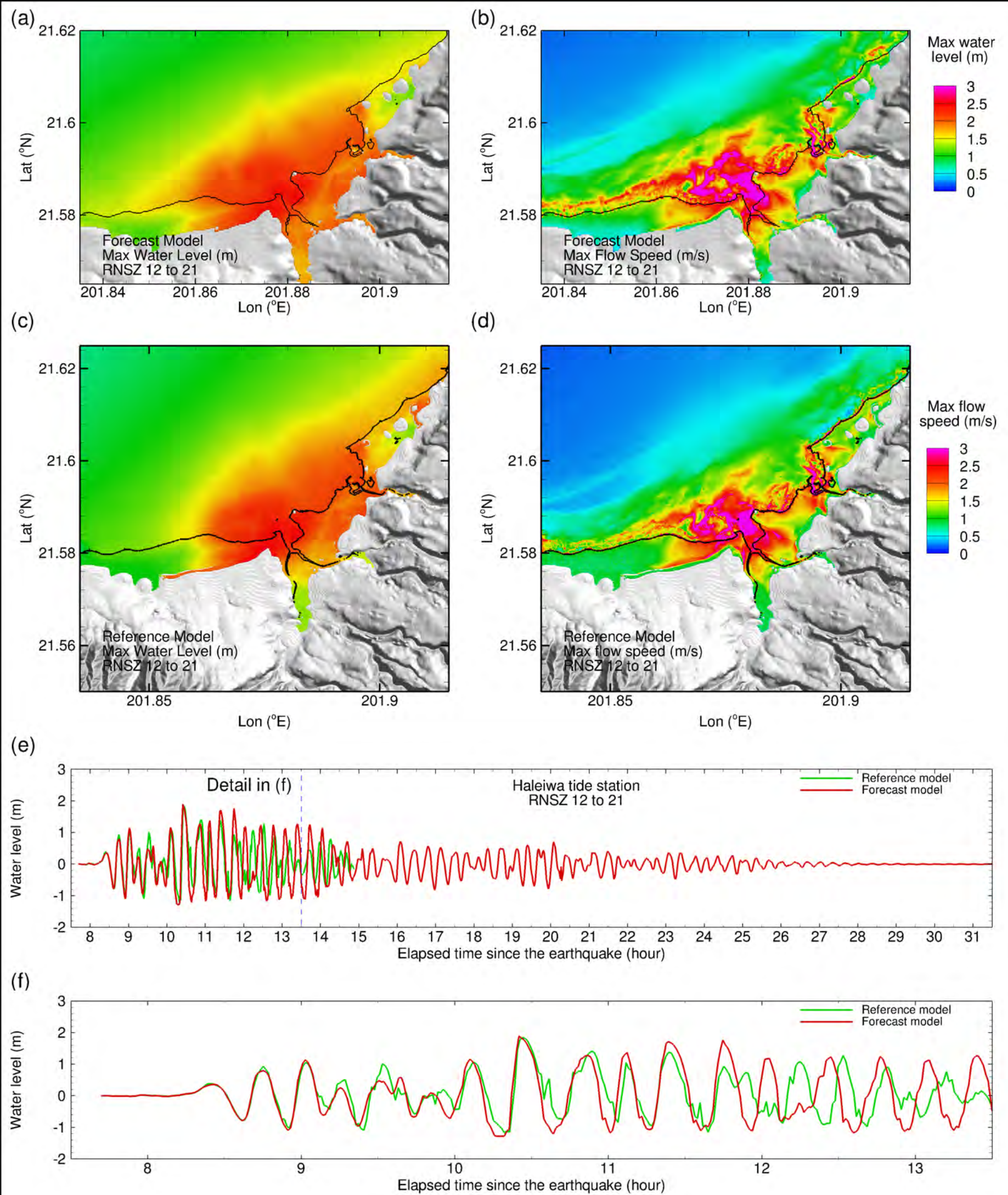


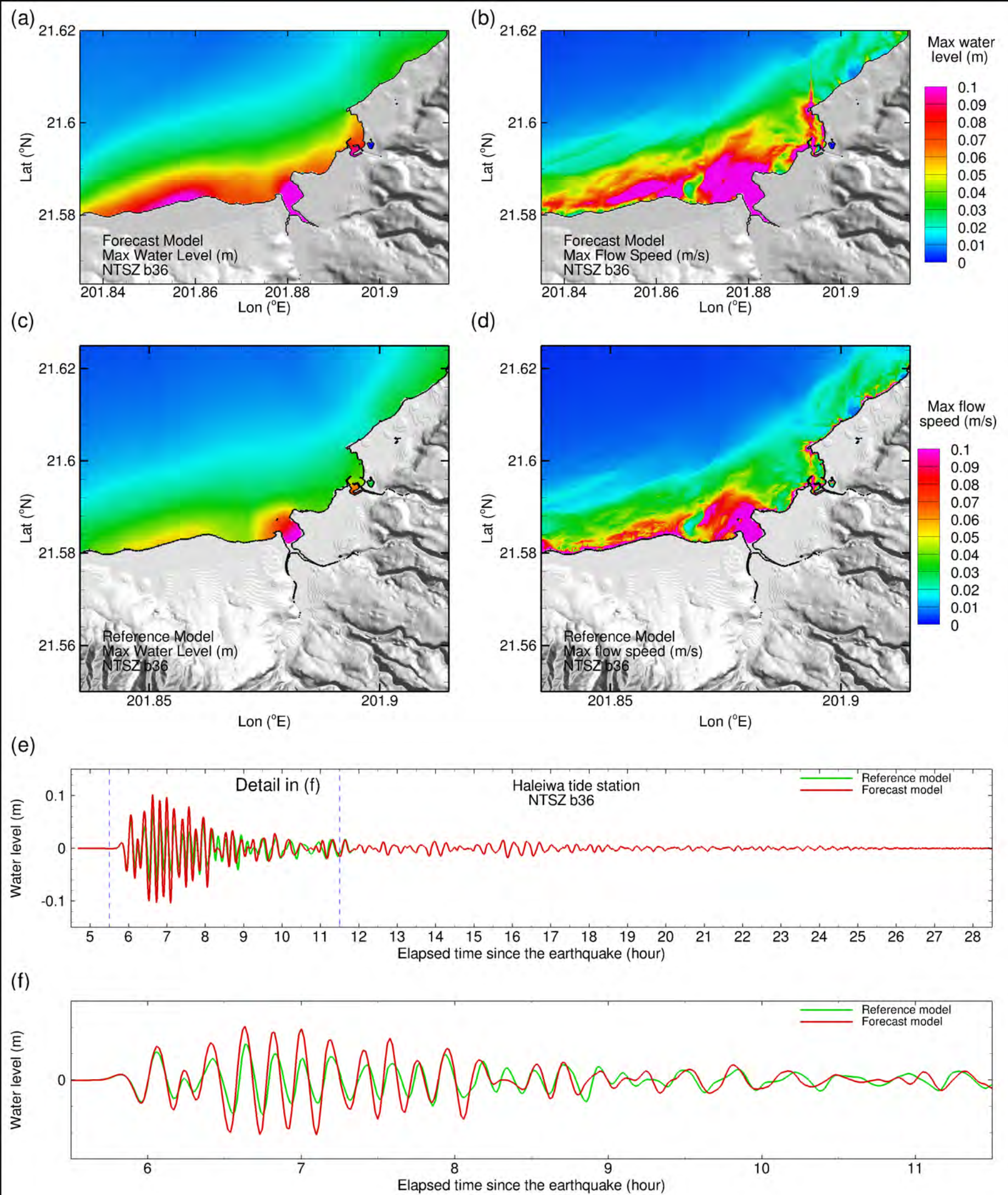


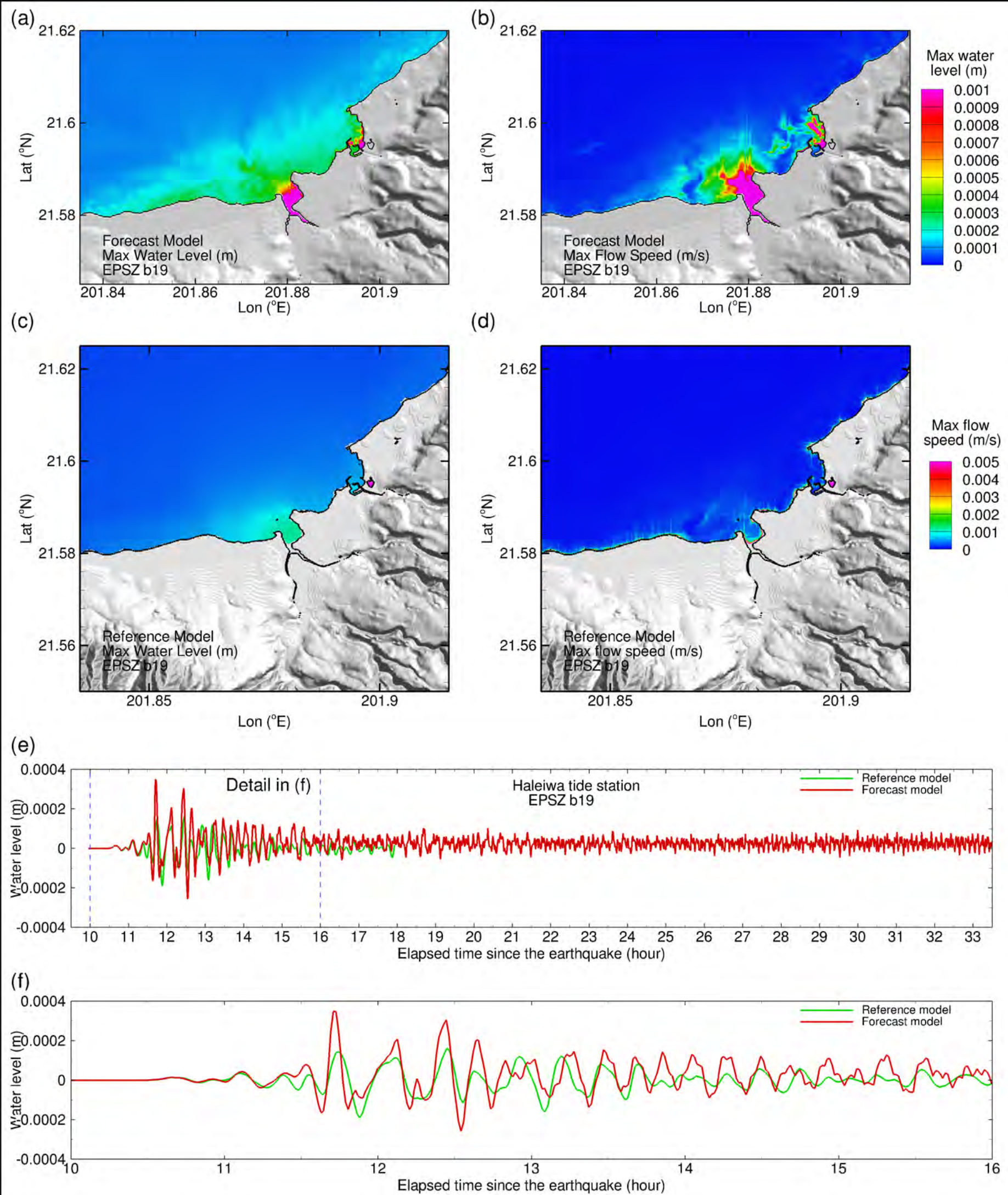












Appendix A.

Development of the Haleiwa, Hawaii, tsunami forecast model occurred prior to parameters changes that were made to reflect modification to the MOST model code. As a result, the input file for running both the optimized tsunami forecast model and the high-resolution reference inundation model in MOST have been updated accordingly. Appendix A1 and A2 provide the updated files for Haleiwa, Hawaii.

Forecast model .in file:

```
0.0001 Minimum amplitude of input offshore wave (m)
1.0 Input minimum depth for offshore (m)
0.1 Input "dry land" depth for inundation (m)
0.0009 Input friction coefficient (n**2)
1 let a and b run up
300.0 blowup limit
0.4 input time step (sec)
108000 input amount of steps
36 Compute "A" arrays every n-th time step, n=
6 Compute "B" arrays every n-th time step, n=
72 Input number of steps between snapshots
0 ...Starting from
1 ...saving grid every n-th node, n=
```

Reference model .in file:

```
0.0001 Minimum amplitude of input offshore wave (m)
1.0 Input minimum depth for offshore (m)
0.1 Input "dry land" depth for inundation (m)
0.0009 Input friction coefficient (n**2)
1 let a and b run up
300.0 blowup limit
0.18 input time step (sec)
160000 input amount of steps
23 Compute "A" arrays every n-th time step, n=
3 Compute "B" arrays every n-th time step, n=
345 Input number of steps between snapshots
0 ...Starting from
1 ...saving grid every n-th node, n=
```

Appendix B. Propagation database: Pacific Ocean Unit Sources

These propagation source details reflect the database as of October 2013, and there may have been updates in the earthquake source parameters after this date.

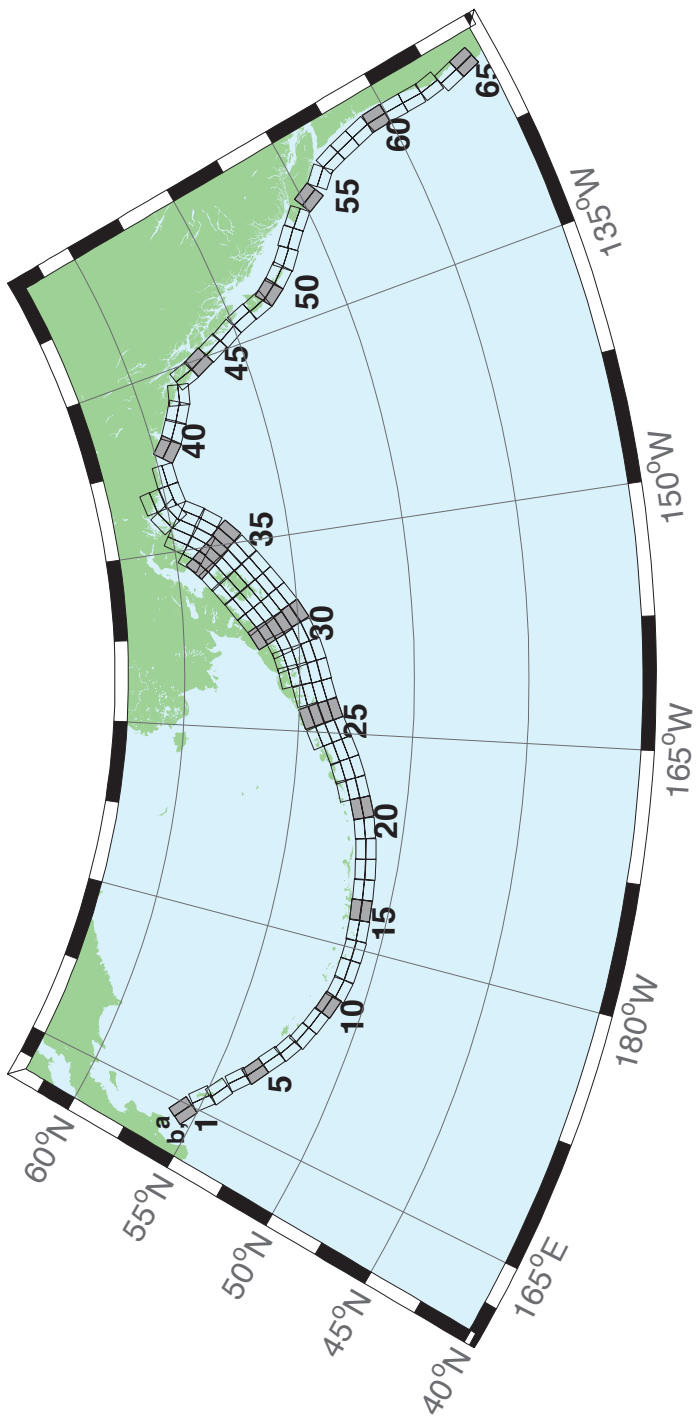


Figure B.1: Aleutian–Alaska–Cascadia Subduction Zone unit sources.

Table B.1 – continued

Segment	Description	Longitude($^{\circ}$ E)	Latitude($^{\circ}$ N)	Strike($^{\circ}$)	Dip($^{\circ}$)	Depth (km)
acsz-57a	Aleutian–Alaska–Cascadia	234.9041	48.2596	341	11	12.82
acsz-57b	Aleutian–Alaska–Cascadia	234.2797	48.1161	341	9	5
acsz-58a	Aleutian–Alaska–Cascadia	235.3021	47.3812	344	11	12.82
acsz-58b	Aleutian–Alaska–Cascadia	234.6776	47.2597	344	9	5
acsz-59a	Aleutian–Alaska–Cascadia	235.6432	46.5082	345	11	12.82
acsz-59b	Aleutian–Alaska–Cascadia	235.0257	46.3941	345	9	5
acsz-60a	Aleutian–Alaska–Cascadia	235.8640	45.5429	356	11	12.82
acsz-60b	Aleutian–Alaska–Cascadia	235.2363	45.5121	356	9	5
acsz-61a	Aleutian–Alaska–Cascadia	235.9106	44.6227	359	11	12.82
acsz-61b	Aleutian–Alaska–Cascadia	235.2913	44.6150	359	9	5
acsz-62a	Aleutian–Alaska–Cascadia	235.9229	43.7245	359	11	12.82
acsz-62b	Aleutian–Alaska–Cascadia	235.3130	43.7168	359	9	5
acsz-63a	Aleutian–Alaska–Cascadia	236.0220	42.9020	350	11	12.82
acsz-63b	Aleutian–Alaska–Cascadia	235.4300	42.8254	350	9	5
acsz-64a	Aleutian–Alaska–Cascadia	235.9638	41.9818	345	11	12.82
acsz-64b	Aleutian–Alaska–Cascadia	235.3919	41.8677	345	9	5
acsz-65a	Aleutian–Alaska–Cascadia	236.2643	41.1141	345	11	12.82
acsz-65b	Aleutian–Alaska–Cascadia	235.7000	41.0000	345	9	5
acsz-238a	Aleutian–Alaska–Cascadia	213.2878	59.8406	236.8	15	17.94
acsz-238y	Aleutian–Alaska–Cascadia	212.3424	60.5664	236.8	15	43.82
acsz-238z	Aleutian–Alaska–Cascadia	212.8119	60.2035	236.8	15	30.88

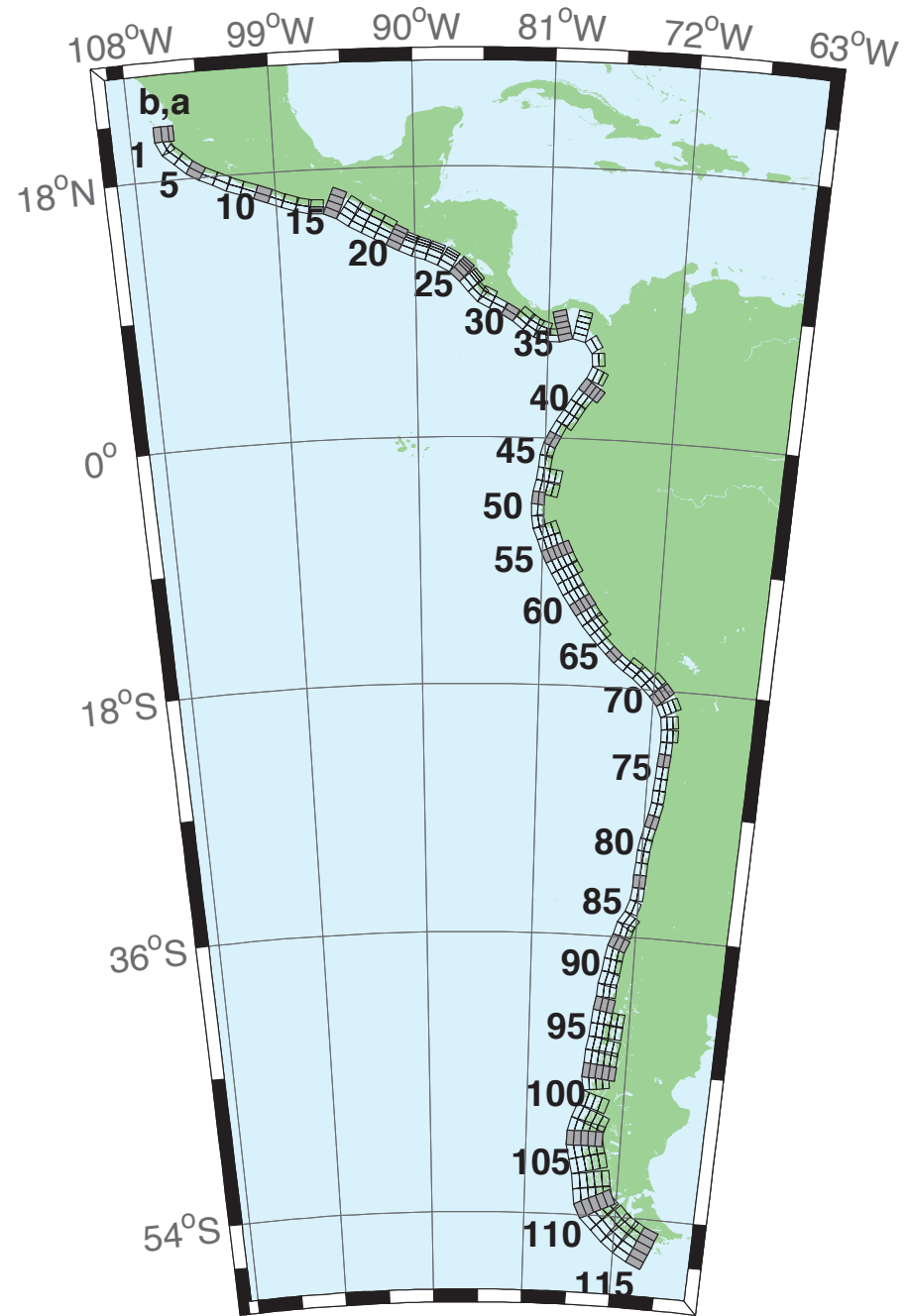


Figure B.2: Central and South America Subduction Zone unit sources.

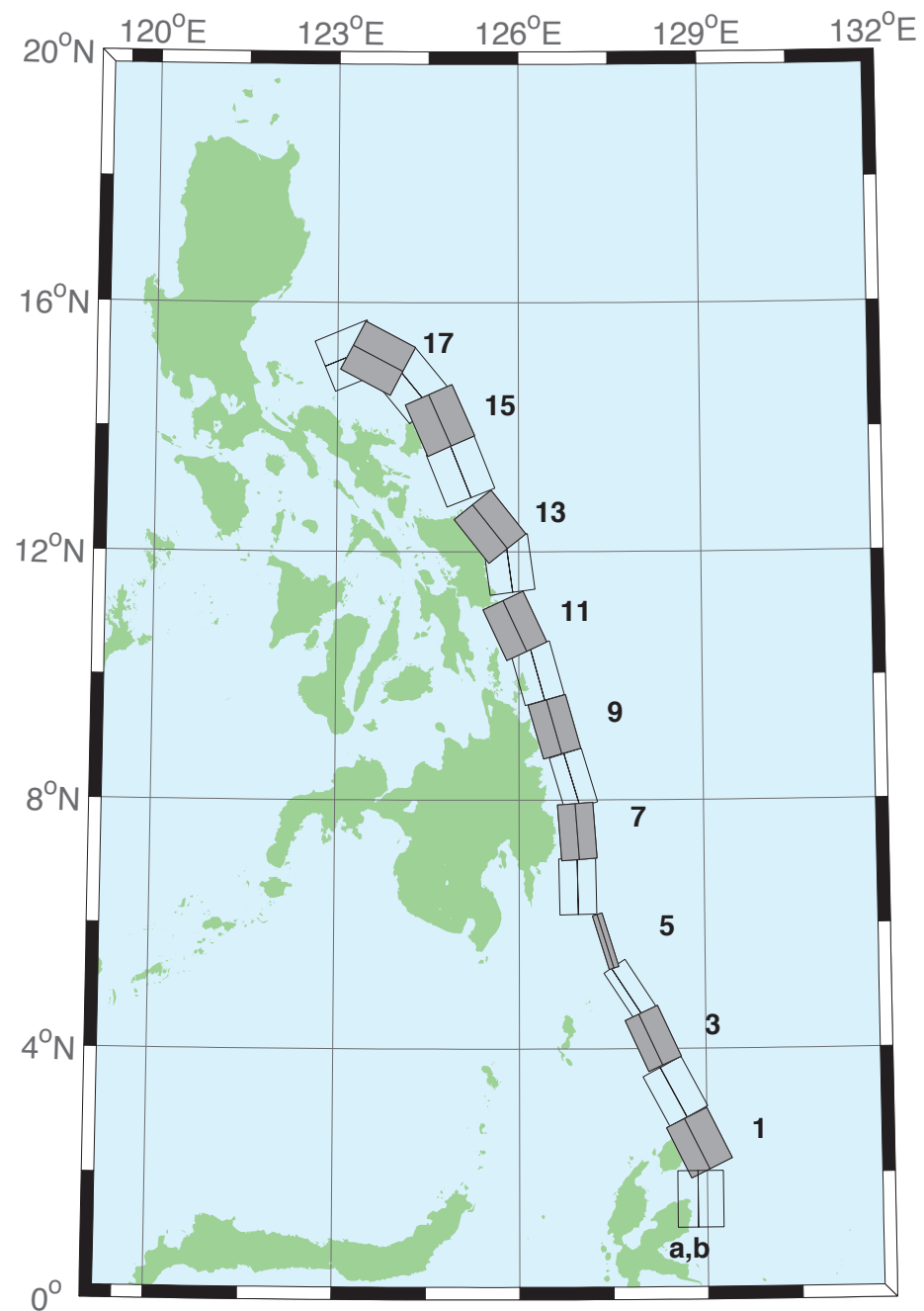


Figure B.3: Eastern Philippines Subduction Zone unit sources.

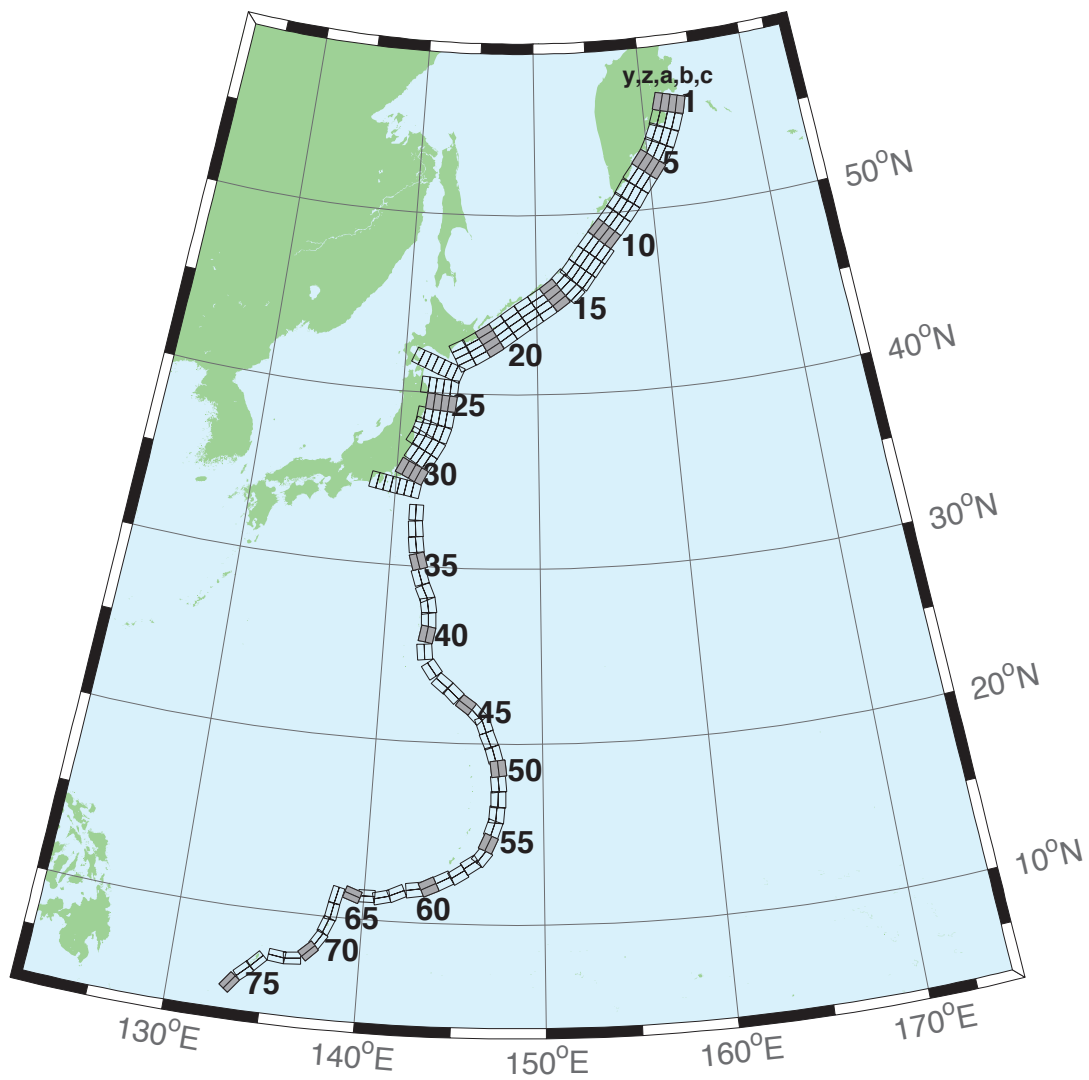


Figure B.4: Kamchatka-Kuril-Japan-Izu-Mariana-Yap Subduction Zone unit sources.

Table B.4 – continued

Segment	Description	Longitude($^{\circ}$ E)	Latitude($^{\circ}$ N)	Strike($^{\circ}$)	Dip($^{\circ}$)	Depth (km)
kisz-71b	Kamchatka-Kuril-Japan-Izu-Mariana-Yap	136.4202	7.5920	263.9	45	5
kisz-72a	Kamchatka-Kuril-Japan-Izu-Mariana-Yap	135.6310	7.9130	276.9	45	40.36
kisz-72b	Kamchatka-Kuril-Japan-Izu-Mariana-Yap	135.5926	7.5977	276.9	45	5
kisz-73a	Kamchatka-Kuril-Japan-Izu-Mariana-Yap	134.3296	7.4541	224	45	40.36
kisz-73b	Kamchatka-Kuril-Japan-Izu-Mariana-Yap	134.5600	7.2335	224	45	5
kisz-74a	Kamchatka-Kuril-Japan-Izu-Mariana-Yap	133.7125	6.8621	228.1	45	40.36
kisz-74b	Kamchatka-Kuril-Japan-Izu-Mariana-Yap	133.9263	6.6258	228.1	45	5
kisz-75a	Kamchatka-Kuril-Japan-Izu-Mariana-Yap	133.0224	6.1221	217.7	45	40.36
kisz-75b	Kamchatka-Kuril-Japan-Izu-Mariana-Yap	133.2751	5.9280	217.7	45	5

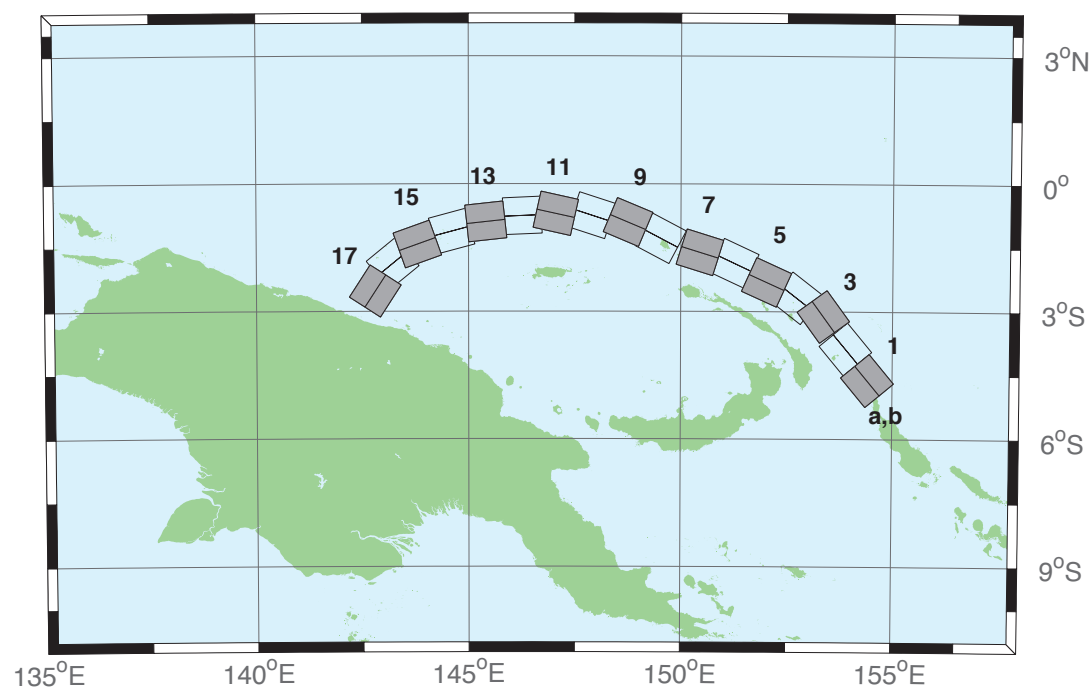


Figure B.5: Manus–Oceanic Convergent Boundary Subduction Zone unit sources.

Table B.5: Earthquake parameters for Manus–Oceanic Convergent Boundary Subduction Zone unit sources.

Segment	Description	Longitude(°E)	Latitude(°N)	Strike(°)	Dip(°)	Depth (km)
mosz-1a	Manus	154.0737	-4.8960	140.2	15	15.88
mosz-1b	Manus	154.4082	-4.6185	140.2	15	2.94
mosz-2a	Manus	153.5589	-4.1575	140.2	15	15.91
mosz-2b	Manus	153.8931	-3.8800	140.2	15	2.97
mosz-3a	Manus	153.0151	-3.3716	143.9	15	16.64
mosz-3b	Manus	153.3662	-3.1160	143.9	15	3.7
mosz-4a	Manus	152.4667	-3.0241	127.7	15	17.32
mosz-4b	Manus	152.7321	-2.6806	127.7	15	4.38
mosz-5a	Manus	151.8447	-2.7066	114.3	15	17.57
mosz-5b	Manus	152.0235	-2.3112	114.3	15	4.63
mosz-6a	Manus	151.0679	-2.2550	115	15	17.66
mosz-6b	Manus	151.2513	-1.8618	115	15	4.72
mosz-7a	Manus	150.3210	-2.0236	107.2	15	17.73
mosz-7b	Manus	150.4493	-1.6092	107.2	15	4.79
mosz-8a	Manus	149.3226	-1.6666	117.8	15	17.83
mosz-8b	Manus	149.5251	-1.2829	117.8	15	4.89
mosz-9a	Manus	148.5865	-1.3017	112.7	15	17.84
mosz-9b	Manus	148.7540	-0.9015	112.7	15	4.9
mosz-10a	Manus	147.7760	-1.1560	108	15	17.78
mosz-10b	Manus	147.9102	-0.7434	108	15	4.84
mosz-11a	Manus	146.9596	-1.1226	102.5	15	17.54
mosz-11b	Manus	147.0531	-0.6990	102.5	15	4.6
mosz-12a	Manus	146.2858	-1.1820	87.48	15	17.29
mosz-12b	Manus	146.2667	-0.7486	87.48	15	4.35
mosz-13a	Manus	145.4540	-1.3214	83.75	15	17.34
mosz-13b	Manus	145.4068	-0.8901	83.75	15	4.4
mosz-14a	Manus	144.7151	-1.5346	75.09	15	17.21
mosz-14b	Manus	144.6035	-1.1154	75.09	15	4.27
mosz-15a	Manus	143.9394	-1.8278	70.43	15	16.52
mosz-15b	Manus	143.7940	-1.4190	70.43	15	3.58
mosz-16a	Manus	143.4850	-2.2118	50.79	15	15.86
mosz-16b	Manus	143.2106	-1.8756	50.79	15	2.92
mosz-17a	Manus	143.1655	-2.7580	33	15	16.64
mosz-17b	Manus	142.8013	-2.5217	33	15	3.7

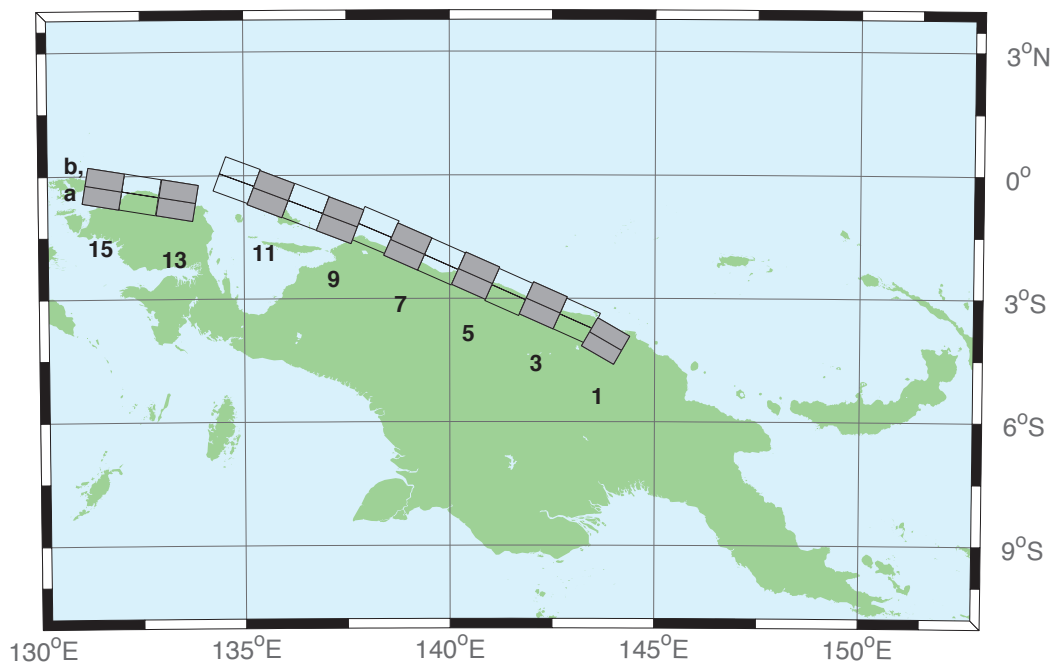


Figure B.6: New Guinea Subduction Zone unit sources.

Table B.6: Earthquake parameters for New Guinea Subduction Zone unit sources.

Segment	Description	Longitude($^{\circ}$ E)	Latitude($^{\circ}$ N)	Strike($^{\circ}$)	Dip($^{\circ}$)	Depth (km)
ngsz-1a	New Guinea	143.6063	-4.3804	120	29	25.64
ngsz-1b	New Guinea	143.8032	-4.0402	120	29	1.4
ngsz-2a	New Guinea	142.9310	-3.9263	114	27.63	20.1
ngsz-2b	New Guinea	143.0932	-3.5628	114	21.72	1.6
ngsz-3a	New Guinea	142.1076	-3.5632	114	20.06	18.73
ngsz-3b	New Guinea	142.2795	-3.1778	114	15.94	5
ngsz-4a	New Guinea	141.2681	-3.2376	114	21	17.76
ngsz-4b	New Guinea	141.4389	-2.8545	114	14.79	5
ngsz-5a	New Guinea	140.4592	-2.8429	114	21.26	16.14
ngsz-5b	New Guinea	140.6296	-2.4605	114	12.87	5
ngsz-6a	New Guinea	139.6288	-2.4960	114	22.72	15.4
ngsz-6b	New Guinea	139.7974	-2.1175	114	12	5
ngsz-7a	New Guinea	138.8074	-2.1312	114	21.39	15.4
ngsz-7b	New Guinea	138.9776	-1.7491	114	12	5
ngsz-8a	New Guinea	138.0185	-1.7353	113.1	18.79	15.14
ngsz-8b	New Guinea	138.1853	-1.3441	113.1	11.7	5
ngsz-9a	New Guinea	137.1805	-1.5037	111	15.24	13.23
ngsz-9b	New Guinea	137.3358	-1.0991	111	9.47	5
ngsz-10a	New Guinea	136.3418	-1.1774	111	13.51	11.09
ngsz-10b	New Guinea	136.4983	-0.7697	111	7	5
ngsz-11a	New Guinea	135.4984	-0.8641	111	11.38	12.49
ngsz-11b	New Guinea	135.6562	-0.4530	111	8.62	5
ngsz-12a	New Guinea	134.6759	-0.5216	110.5	10	13.68
ngsz-12b	New Guinea	134.8307	-0.1072	110.5	10	5
ngsz-13a	New Guinea	133.3065	-1.0298	99.5	10	13.68
ngsz-13b	New Guinea	133.3795	-0.5935	99.5	10	5
ngsz-14a	New Guinea	132.4048	-0.8816	99.5	10	13.68
ngsz-14b	New Guinea	132.4778	-0.4453	99.5	10	5
ngsz-15a	New Guinea	131.5141	-0.7353	99.5	10	13.68
ngsz-15b	New Guinea	131.5871	-0.2990	99.5	10	5

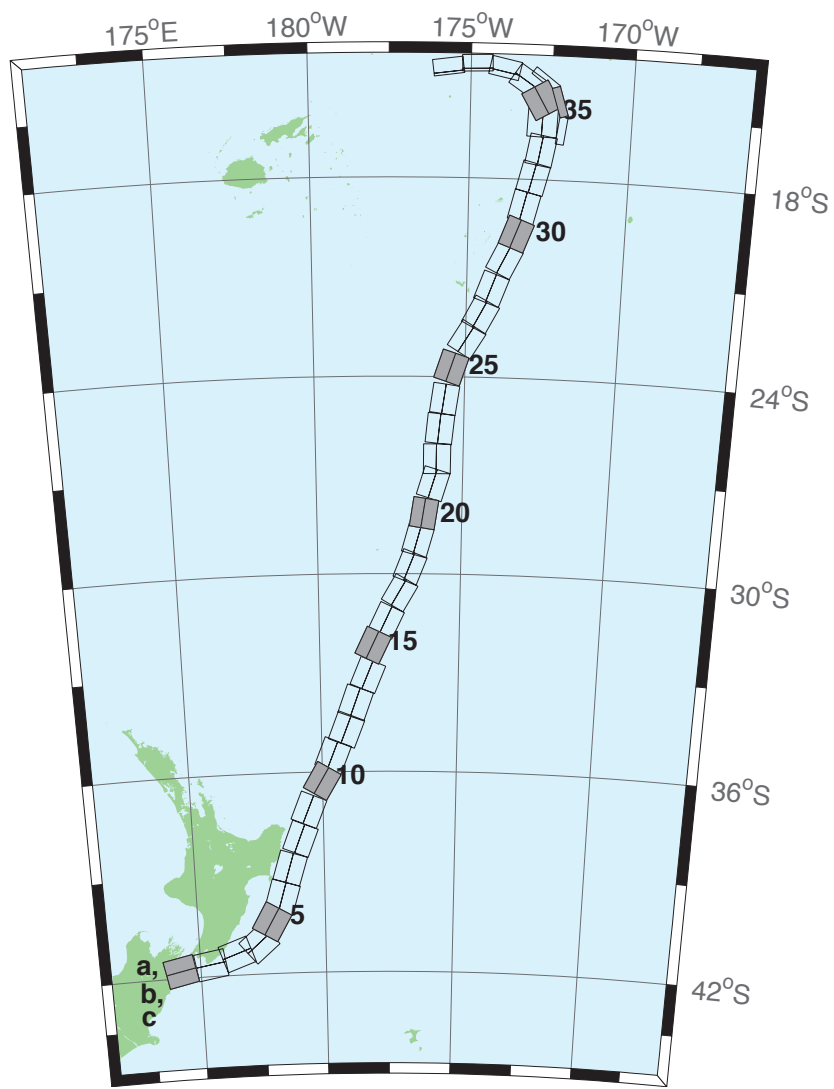


Figure B.7: New Zealand–Kermadec–Tonga Subduction Zone unit sources.

Table B.7 – continued

Segment	Description	Longitude($^{\circ}$ E)	Latitude($^{\circ}$ N)	Strike($^{\circ}$)	Dip($^{\circ}$)	Depth (km)
ntsz-27b	New Zealand–Tonga	185.4522	-22.0928	207.9	18.27	5
ntsz-28a	New Zealand–Tonga	185.4037	-21.1758	200.5	32.44	21.76
ntsz-28b	New Zealand–Tonga	185.7849	-21.3084	200.5	19.58	5
ntsz-29a	New Zealand–Tonga	185.8087	-20.2629	206.4	32.47	20.4
ntsz-29b	New Zealand–Tonga	186.1710	-20.4312	206.4	17.94	5
ntsz-30a	New Zealand–Tonga	186.1499	-19.5087	200.9	32.98	22.46
ntsz-30b	New Zealand–Tonga	186.5236	-19.6432	200.9	20.44	5
ntsz-31a	New Zealand–Tonga	186.3538	-18.7332	193.9	34.41	21.19
ntsz-31b	New Zealand–Tonga	186.7339	-18.8221	193.9	18.89	5
ntsz-32a	New Zealand–Tonga	186.5949	-17.8587	194.1	30	19.12
ntsz-32b	New Zealand–Tonga	186.9914	-17.9536	194.1	16.4	5
ntsz-33a	New Zealand–Tonga	186.8172	-17.0581	190	33.15	23.34
ntsz-33b	New Zealand–Tonga	187.2047	-17.1237	190	21.52	5
ntsz-34a	New Zealand–Tonga	186.7814	-16.2598	182.1	15	13.41
ntsz-34b	New Zealand–Tonga	187.2330	-16.2759	182.1	9.68	5
ntsz-34c	New Zealand–Tonga	187.9697	-16.4956	7.62	57.06	6.571
ntsz-35a	New Zealand–Tonga	186.8000	-15.8563	149.8	15	12.17
ntsz-35b	New Zealand–Tonga	187.1896	-15.6384	149.8	8.24	5
ntsz-35c	New Zealand–Tonga	187.8776	-15.6325	342.4	57.06	6.571
ntsz-36a	New Zealand–Tonga	186.5406	-15.3862	123.9	40.44	36.72
ntsz-36b	New Zealand–Tonga	186.7381	-15.1025	123.9	39.38	5
ntsz-36c	New Zealand–Tonga	187.3791	-14.9234	307	57.06	6.571
ntsz-37a	New Zealand–Tonga	185.9883	-14.9861	102	68.94	30.99
ntsz-37b	New Zealand–Tonga	186.0229	-14.8282	102	31.32	5
ntsz-38a	New Zealand–Tonga	185.2067	-14.8259	88.4	80	26.13
ntsz-38b	New Zealand–Tonga	185.2044	-14.7479	88.4	25	5
ntsz-39a	New Zealand–Tonga	184.3412	-14.9409	82.55	80	26.13
ntsz-39b	New Zealand–Tonga	184.3307	-14.8636	82.55	25	5

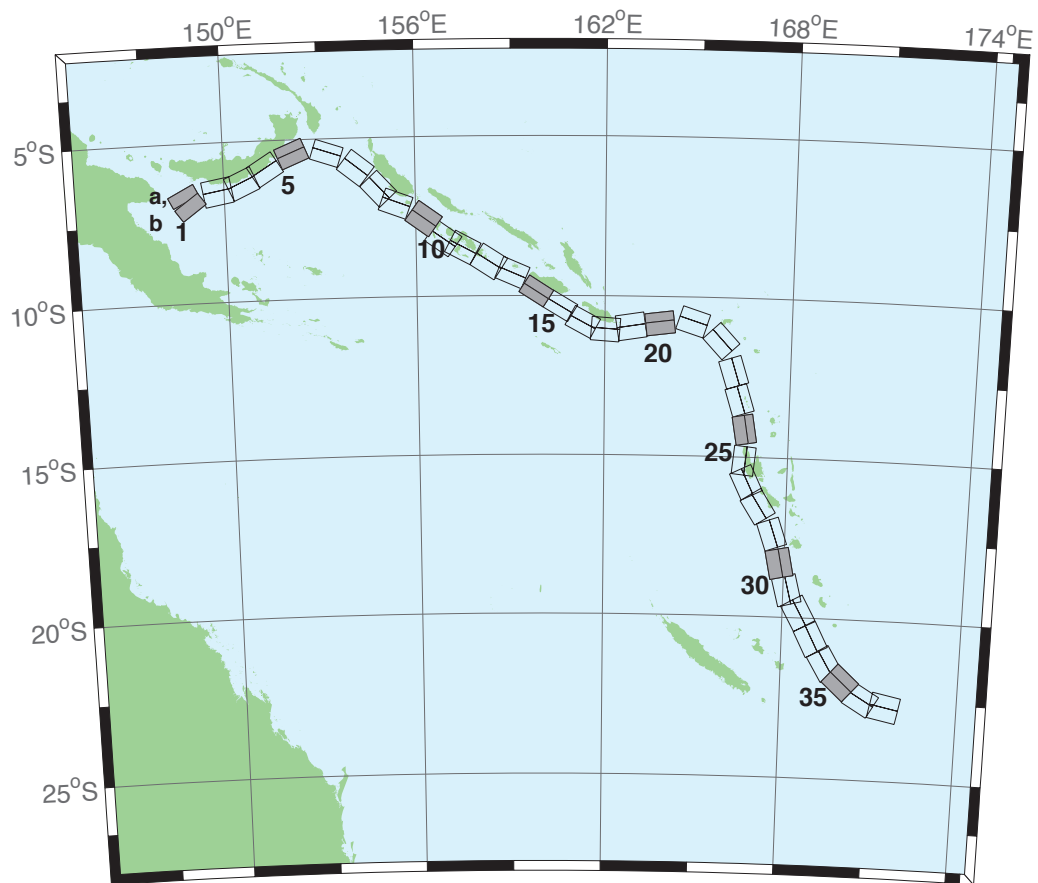


Figure B.8: New Britain–Solomons–Vanuatu Zone unit sources.

Table B.8 – continued

Segment	Description	Longitude($^{\circ}$ E)	Latitude($^{\circ}$ N)	Strike($^{\circ}$)	Dip($^{\circ}$)	Depth (km)
nvsz-27b	New Britain–Vanuatu	166.7068	-15.7695	334.2	24.15	5
nvsz-28a	New Britain–Vanuatu	167.4074	-16.3455	327.5	41.53	22.44
nvsz-28b	New Britain–Vanuatu	167.1117	-16.5264	327.5	20.42	5
nvsz-29a	New Britain–Vanuatu	167.9145	-17.2807	341.2	49.1	24.12
nvsz-29b	New Britain–Vanuatu	167.6229	-17.3757	341.2	22.48	5
nvsz-30a	New Britain–Vanuatu	168.2220	-18.2353	348.6	44.19	23.99
nvsz-30b	New Britain–Vanuatu	167.8895	-18.2991	348.6	22.32	5
nvsz-31a	New Britain–Vanuatu	168.5022	-19.0510	345.6	42.2	22.26
nvsz-31b	New Britain–Vanuatu	168.1611	-19.1338	345.6	20.2	5
nvsz-32a	New Britain–Vanuatu	168.8775	-19.6724	331.1	42.03	21.68
nvsz-32b	New Britain–Vanuatu	168.5671	-19.8338	331.1	19.49	5
nvsz-33a	New Britain–Vanuatu	169.3422	-20.4892	332.9	40.25	22.4
nvsz-33b	New Britain–Vanuatu	169.0161	-20.6453	332.9	20.37	5
nvsz-34a	New Britain–Vanuatu	169.8304	-21.2121	329.1	39	22.73
nvsz-34b	New Britain–Vanuatu	169.5086	-21.3911	329.1	20.77	5
nvsz-35a	New Britain–Vanuatu	170.3119	-21.6945	311.9	39	22.13
nvsz-35b	New Britain–Vanuatu	170.0606	-21.9543	311.9	20.03	5
nvsz-36a	New Britain–Vanuatu	170.9487	-22.1585	300.4	39.42	23.5
nvsz-36b	New Britain–Vanuatu	170.7585	-22.4577	300.4	21.71	5
nvsz-37a	New Britain–Vanuatu	171.6335	-22.3087	281.3	30	22.1
nvsz-37b	New Britain–Vanuatu	171.5512	-22.6902	281.3	20	5

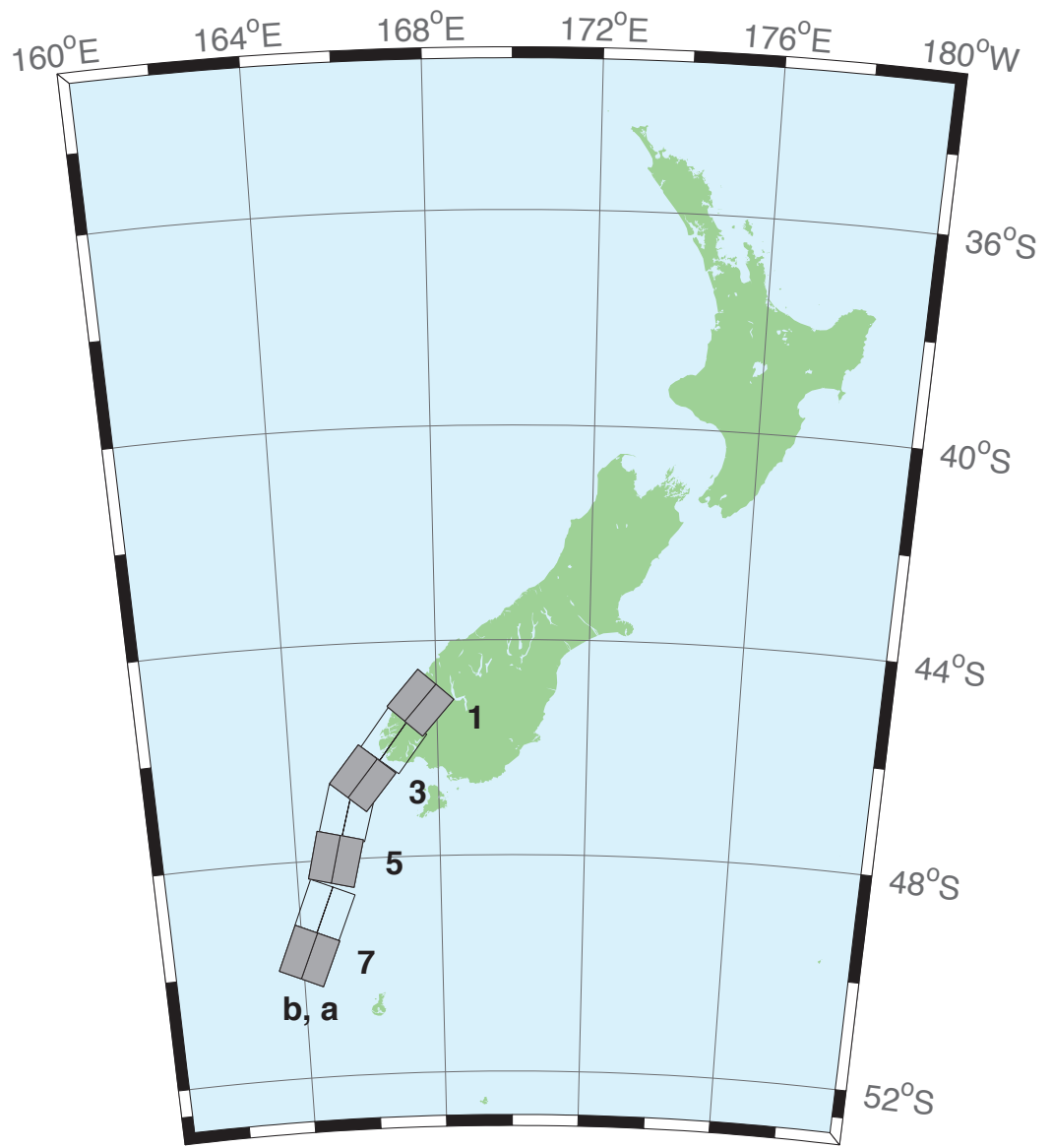


Figure B.9: New Zealand–Puysegur Zone unit sources.

Table B.9: Earthquake parameters for New Zealand–Puysegur Subduction Zone unit sources.

Segment	Description	Longitude($^{\circ}$ E)	Latitude($^{\circ}$ N)	Strike($^{\circ}$)	Dip($^{\circ}$)	Depth (km)
nzs–1a	New Zealand–Puysegur	168.0294	-45.4368	41.5	15	17.94
nzs–1b	New Zealand–Puysegur	167.5675	-45.1493	41.5	15	5
nzs–2a	New Zealand–Puysegur	167.3256	-46.0984	37.14	15	17.94
nzs–2b	New Zealand–Puysegur	166.8280	-45.8365	37.14	15	5
nzs–3a	New Zealand–Puysegur	166.4351	-46.7897	39.53	15	17.94
nzs–3b	New Zealand–Puysegur	165.9476	-46.5136	39.53	15	5
nzs–4a	New Zealand–Puysegur	166.0968	-47.2583	15.38	15	17.94
nzs–4b	New Zealand–Puysegur	165.4810	-47.1432	15.38	15	5
nzs–5a	New Zealand–Puysegur	165.7270	-48.0951	13.94	15	17.94
nzs–5b	New Zealand–Puysegur	165.0971	-47.9906	13.94	15	5
nzs–6a	New Zealand–Puysegur	165.3168	-49.0829	22.71	15	17.94
nzs–6b	New Zealand–Puysegur	164.7067	-48.9154	22.71	15	5
nzs–7a	New Zealand–Puysegur	164.8017	-49.9193	23.25	15	17.94
nzs–7b	New Zealand–Puysegur	164.1836	-49.7480	23.25	15	5

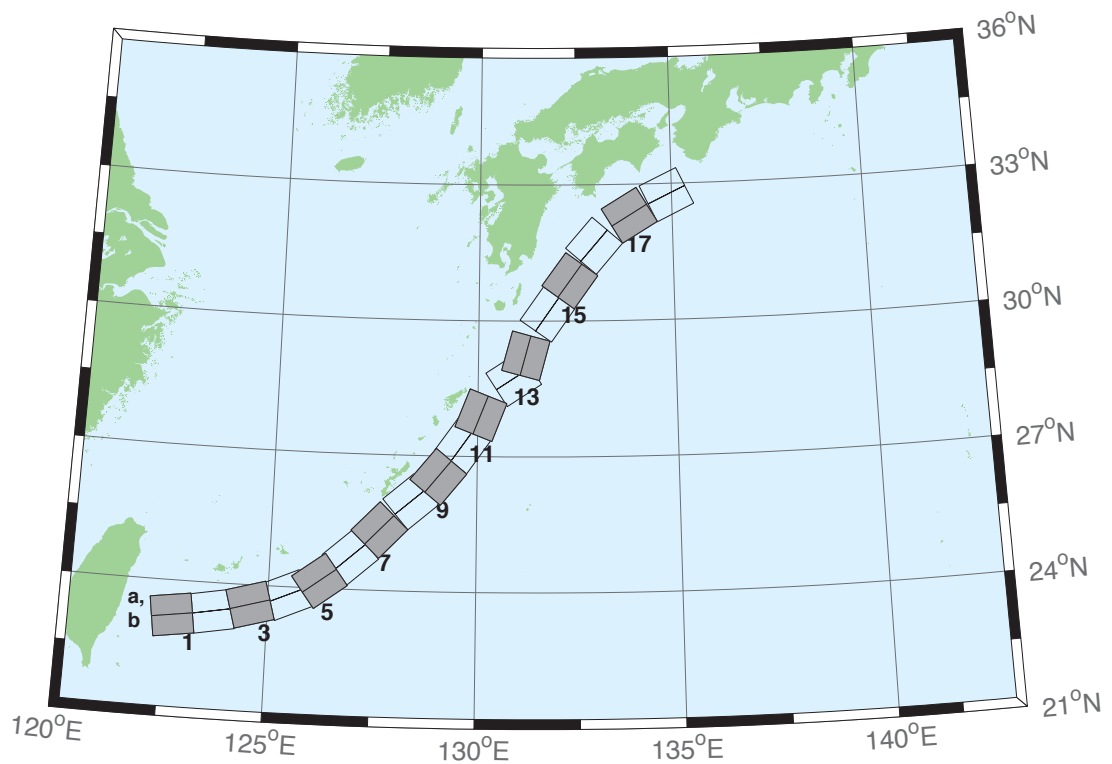


Figure B.10: Ryukyu–Kyushu–Nankai Zone unit sources.

Table B.10: Earthquake parameters for Ryukyu–Kyushu–Nankai Subduction Zone unit sources.

Segment	Description	Longitude($^{\circ}$ E)	Latitude($^{\circ}$ N)	Strike($^{\circ}$)	Dip($^{\circ}$)	Depth (km)
rnsz–1a	Ryukyu–Nankai	122.6672	23.6696	262	14	11.88
rnsz–1b	Ryukyu–Nankai	122.7332	23.2380	262	10	3.2
rnsz–2a	Ryukyu–Nankai	123.5939	23.7929	259.9	18.11	12.28
rnsz–2b	Ryukyu–Nankai	123.6751	23.3725	259.9	10	3.6
rnsz–3a	Ryukyu–Nankai	124.4604	23.9777	254.6	19.27	14.65
rnsz–3b	Ryukyu–Nankai	124.5830	23.5689	254.6	12.18	4.1
rnsz–4a	Ryukyu–Nankai	125.2720	24.2102	246.8	18	20.38
rnsz–4b	Ryukyu–Nankai	125.4563	23.8177	246.8	16	6.6
rnsz–5a	Ryukyu–Nankai	125.9465	24.5085	233.6	18	20.21
rnsz–5b	Ryukyu–Nankai	126.2241	24.1645	233.6	16	6.43
rnsz–6a	Ryukyu–Nankai	126.6349	25.0402	228.7	17.16	19.55
rnsz–6b	Ryukyu–Nankai	126.9465	24.7176	228.7	15.16	6.47
rnsz–7a	Ryukyu–Nankai	127.2867	25.6343	224	15.85	17.98
rnsz–7b	Ryukyu–Nankai	127.6303	25.3339	224	13.56	6.26
rnsz–8a	Ryukyu–Nankai	128.0725	26.3146	229.7	14.55	14.31
rnsz–8b	Ryukyu–Nankai	128.3854	25.9831	229.7	9.64	5.94
rnsz–9a	Ryukyu–Nankai	128.6642	26.8177	219.2	15.4	12.62
rnsz–9b	Ryukyu–Nankai	129.0391	26.5438	219.2	8	5.66
rnsz–10a	Ryukyu–Nankai	129.2286	27.4879	215.2	17	12.55
rnsz–10b	Ryukyu–Nankai	129.6233	27.2402	215.2	8.16	5.45
rnsz–11a	Ryukyu–Nankai	129.6169	28.0741	201.3	17	12.91
rnsz–11b	Ryukyu–Nankai	130.0698	27.9181	201.3	8.8	5.26
rnsz–12a	Ryukyu–Nankai	130.6175	29.0900	236.7	16.42	13.05
rnsz–12b	Ryukyu–Nankai	130.8873	28.7299	236.7	9.57	4.74
rnsz–13a	Ryukyu–Nankai	130.7223	29.3465	195.2	20.25	15.89
rnsz–13b	Ryukyu–Nankai	131.1884	29.2362	195.2	12.98	4.66
rnsz–14a	Ryukyu–Nankai	131.3467	30.3899	215.1	22.16	19.73
rnsz–14b	Ryukyu–Nankai	131.7402	30.1507	215.1	17.48	4.71
rnsz–15a	Ryukyu–Nankai	131.9149	31.1450	216	15.11	16.12
rnsz–15b	Ryukyu–Nankai	132.3235	30.8899	216	13.46	4.48
rnsz–16a	Ryukyu–Nankai	132.5628	31.9468	220.9	10.81	10.88
rnsz–16b	Ryukyu–Nankai	132.9546	31.6579	220.9	7.19	4.62
rnsz–17a	Ryukyu–Nankai	133.6125	32.6956	239	10.14	12.01
rnsz–17b	Ryukyu–Nankai	133.8823	32.3168	239	8.41	4.7
rnsz–18a	Ryukyu–Nankai	134.6416	33.1488	244.7	10.99	14.21
rnsz–18b	Ryukyu–Nankai	134.8656	32.7502	244.5	10.97	4.7
rnsz–19a	Ryukyu–Nankai	135.6450	33.5008	246.5	14.49	14.72
rnsz–19b	Ryukyu–Nankai	135.8523	33.1021	246.5	11.87	4.44
rnsz–20a	Ryukyu–Nankai	136.5962	33.8506	244.8	15	14.38
rnsz–20b	Ryukyu–Nankai	136.8179	33.4581	244.8	12	3.98
rnsz–21a	Ryukyu–Nankai	137.2252	34.3094	231.9	15	15.4
rnsz–21b	Ryukyu–Nankai	137.5480	33.9680	231.9	12	5
rnsz–22a	Ryukyu–Nankai	137.4161	34.5249	192.3	15	15.4
rnsz–22b	Ryukyu–Nankai	137.9301	34.4327	192.3	12	5

Appendix C. SIFT testing results

Authors: Lindsey Wright, Yong Wei

1.0 PURPOSE

Forecast models are tested with synthetic tsunami events covering a range of tsunami source locations. Testing is also done with selected historical tsunami events when available.

The purpose of forecast model testing is three-fold. The first objective is to assure that the results obtained with NOAA's tsunami forecast system, which has been released to the Tsunami Warning Centers for operational use, are consistent those obtained by the researcher during the development of the forecast model. The second objective is to test the forecast model for consistency, accuracy, time efficiency, and quality of results over a range of possible tsunami locations and magnitudes. The third objective is to identify bugs and issues in need of resolution by the researcher who developed the Forecast Model or by the forecast software development team before the next version release to NOAA's two Tsunami Warning Centers.

Local hardware and software applications, and tools familiar to the researcher(s), are used to run the Method of Splitting Tsunamis (MOST) model during the forecast model development. The test results presented in this report lend confidence that the model performs as developed and produces the same results when initiated within the forecast application in an operational setting as those produced by the researcher during the forecast model development. The test results assure those who rely on the Haleiwa tsunami forecast model that consistent results are produced irrespective of system.

2.0 TESTING PROCEDURE

The general procedure for forecast model testing is to run a set of synthetic tsunami scenarios and a selected set of historical tsunami events through the forecast system application and compare the results with those obtained by the researcher during the forecast model development and presented in the Tsunami Forecast Model Report. Specific steps taken to test the model include:

1. Identification of testing scenarios, including the standard set of synthetic events, appropriate historical events, and customized synthetic scenarios that may have been used by the researcher(s) in developing the forecast model.
 2. Creation of new events to represent customized synthetic scenarios used by the researcher(s) in developing the forecast model, if any.
 3. Submission of test model runs with the forecast system, and export of the results from A, B, and C grids, along with time series.
 4. Recording applicable metadata, including the specific version of the forecast system used for testing.
 5. Examination of forecast model results from the forecast system for instabilities in both time series and plot results.
 6. Comparison of forecast model results obtained through the forecast system with those obtained during the forecast model development.
 7. Summarization of results with specific mention of quality, consistency, and time efficiency.
 8. Reporting of issues identified to modeler and forecast software development team.
9. Retesting the forecast models in the forecast system when reported issues have been addressed or explained.

Synthetic model runs were tested on a DELL PowerEdge R510 computer equipped with two Xeon E5670 processors at 2.93 Ghz, each with 12 MBytes of cache and 32GB memory. The processors are hex core and support hyperthreading, resulting in the computer performing as a 24 processor core machine. Additionally, the testing computer supports 10 Gigabit Ethernet for fast network connections. This computer configuration is similar or the same as the configurations of the computers installed at the Tsunami Warning Centers so the compute times should only vary slightly.

Results

The Haleiwa forecast model was tested with NOAA's tsunami forecast system version 3.2.

The Haleiwa forecast model was tested with four synthetic scenarios and one historical tsunami event. Test results from the forecast system and comparisons with the results obtained during the forecast model development are shown numerically in Table 1 and graphically in Figures 1 to 5. The results show that the forecast model is stable and robust, with consistent and high quality results across geographically distributed tsunami sources and mega-event tsunami magnitudes. The model run time (wall clock time) was 58 minutes for 12 hours of simulation time, and under 19 minutes for 4 hours. This run time is not within the 10 minute run time for 4 hours of simulation time but is justified because....

Four synthetic events were run on the Haleiwa forecast model. The modeled scenarios were stable for all cases tested, with no instabilities or ringing. Amplitudes greater than 100 centimeters (cm) were recorded for all test cases. The largest modeled amplitude was 407 cm and originated in Kamchatka-Yap-Mariana-Izu-Bonin (KISZ 22-31) source. The smallest signal of 106 cm was recorded at the Central and South America (CSSZ 91-100) source. The forecast system output was consistently higher than max values found during development with an average difference of 6 cm. The main cause of these differences is the output time interval, which was 57.6 sec during the model development (for the purpose of storage saving), and is 28.8 sec in SIFT. Direct comparisons of output from the forecast tool with results of both the Tohoku 2011 historical event and available development synthetic events, demonstrated that the wave pattern were nearly identical in shape and pattern.

List of Figures

Figure 1. Response of the Haleiwa forecast model to synthetic scenario KISZ 22-31 ($\alpha=25$). Maximum sea surface elevation for (a) A-grid, b) B-grid, c) C-grid. (d) Sea surface elevation time series at the C-grid warning point (d). (f) The result obtained during model development and is shown for comparison with test results.

Figure 2. Response of the Haleiwa forecast model to synthetic scenario ACSZ 56-65 ($\alpha=25$). Maximum sea surface elevation for (a) A-grid, b) B-grid, c) C-grid. (d) Sea surface elevation time series at the C-grid warning point. (f) The result obtained during model development and is shown for comparison with test results.

Figure 3. Response of the Haleiwa forecast model to synthetic scenario CSSZ 89-98 ($\alpha=30$). Maximum sea surface elevation for (a) A-grid, b) B-grid, c) C-grid. (d) Sea surface elevation time series at the C-grid warning point. (f) The result obtained during model development and is shown for comparison with test results.

Figure 4. Response of the Haleiwa forecast model to synthetic scenario NTSZ 30-39 ($\alpha=30$). Maximum sea surface elevation for (a) A-grid, b) B-grid, c) C-grid. (d) Sea surface elevation time series at the C-grid warning point. (f) The result obtained during model development and is shown for comparison with test results.

Figure 5. Response of the Haleiwa forecast model to the 2013 Solomon Islands tsunami. Maximum sea surface elevation for (a) A-grid, b) B-grid, c) C-grid. (d) Sea surface elevation time series at the C-grid warning point. (f) The result obtained during model development and is shown for comparison with test results.

List of Tables

Table 1. Table of maximum and minimum amplitudes at Haleiwa, Hawaii warning point for synthetic and historical events tested using SIFT.

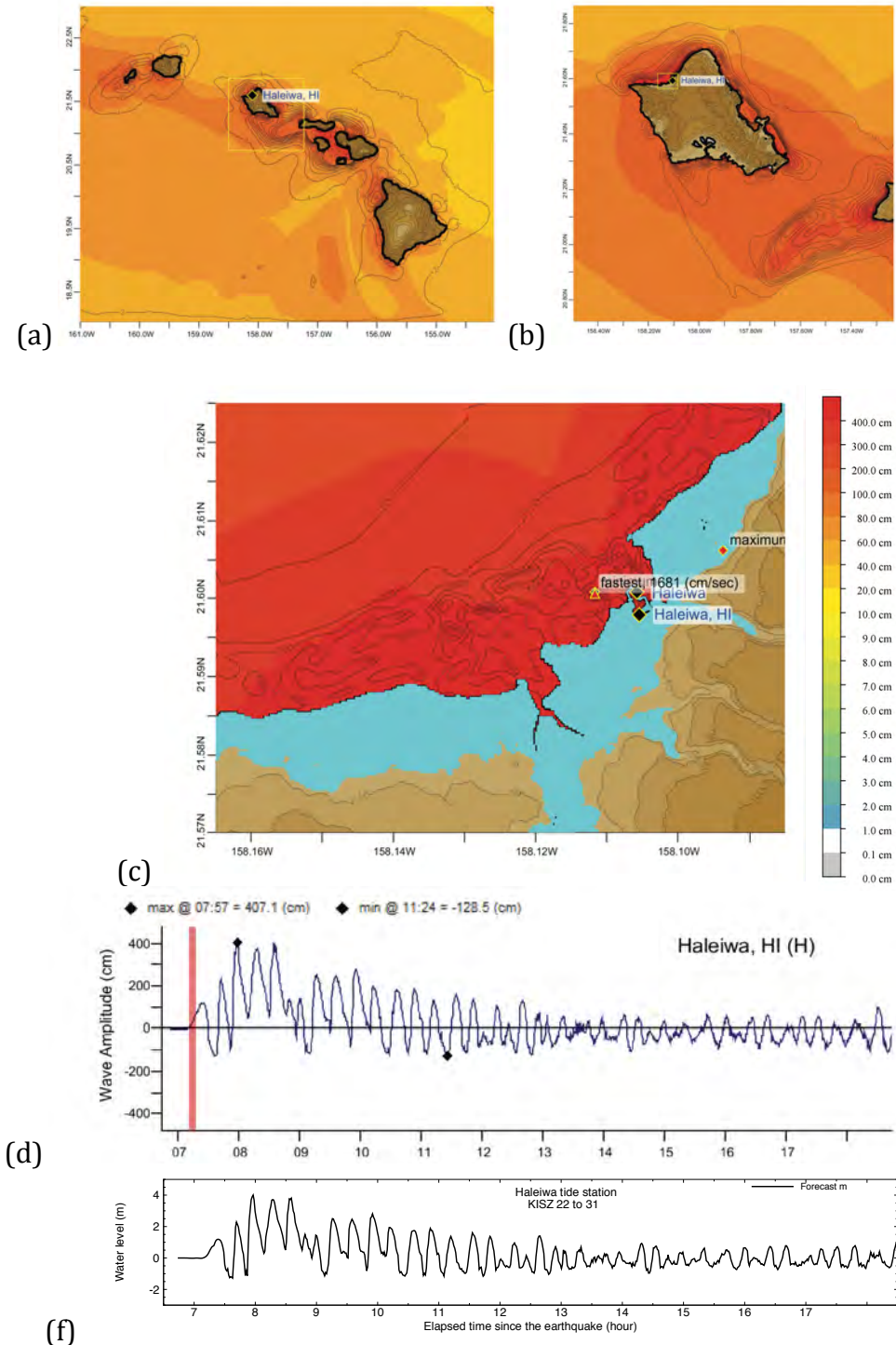


Figure 1. Response of the Haleiwa forecast model to synthetic scenario KISZ 22-31 (alpha=25). Maximum sea surface elevation for (a) A-grid, b) B-grid, c) C-grid. (d) Sea surface elevation time series at the C-grid warning point (d). (f) The result obtained during model development and is shown for comparison with test results.

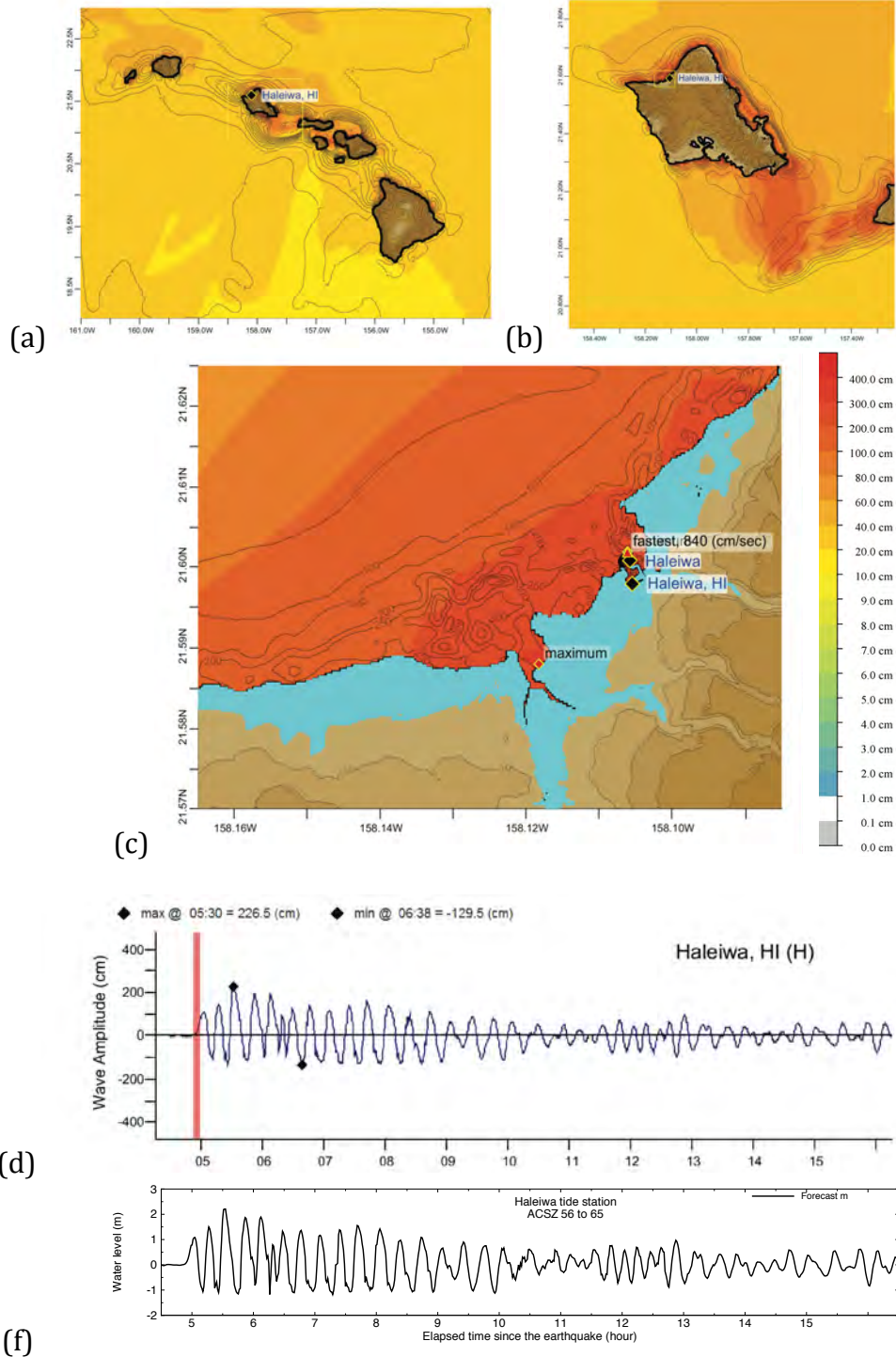


Figure 2: Response of the Haleiwa forecast model to synthetic scenario ACSZ 56-65 ($\alpha=25$). Maximum sea surface elevation for (a) A-grid, b) B-grid, c) C-grid. (d) Sea surface elevation time series at the C-grid warning point. (f) The result obtained during model development and is shown for comparison with test results.

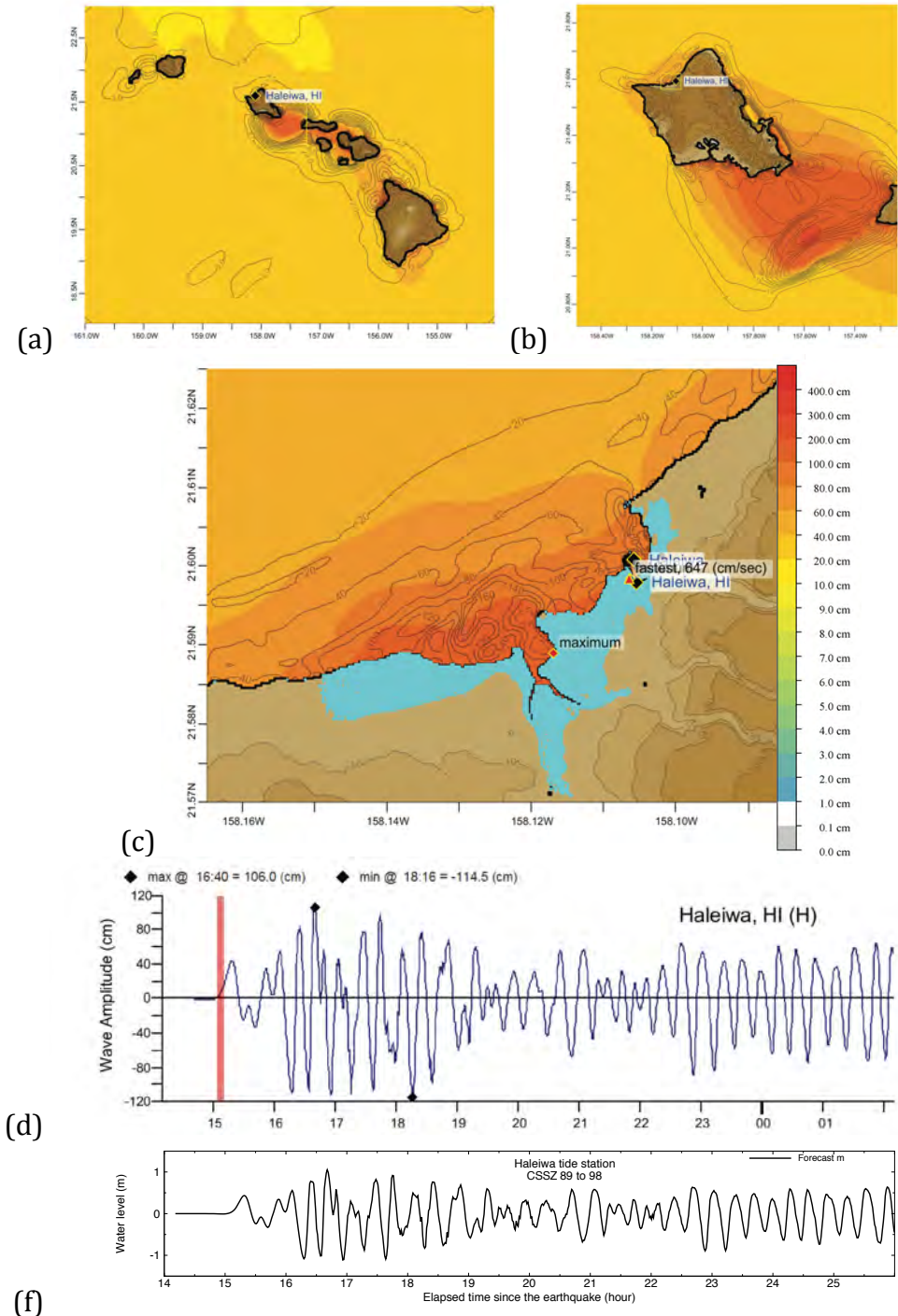


Figure 3: Response of the Haleiwa forecast model to synthetic scenario CSSZ 89-98 ($\alpha=30$). Maximum sea surface elevation for (a) A-grid, b) B-grid, c) C-grid. (d) Sea surface elevation time series at the C-grid warning point. (f) The result obtained during model development and is shown for comparison with test results.

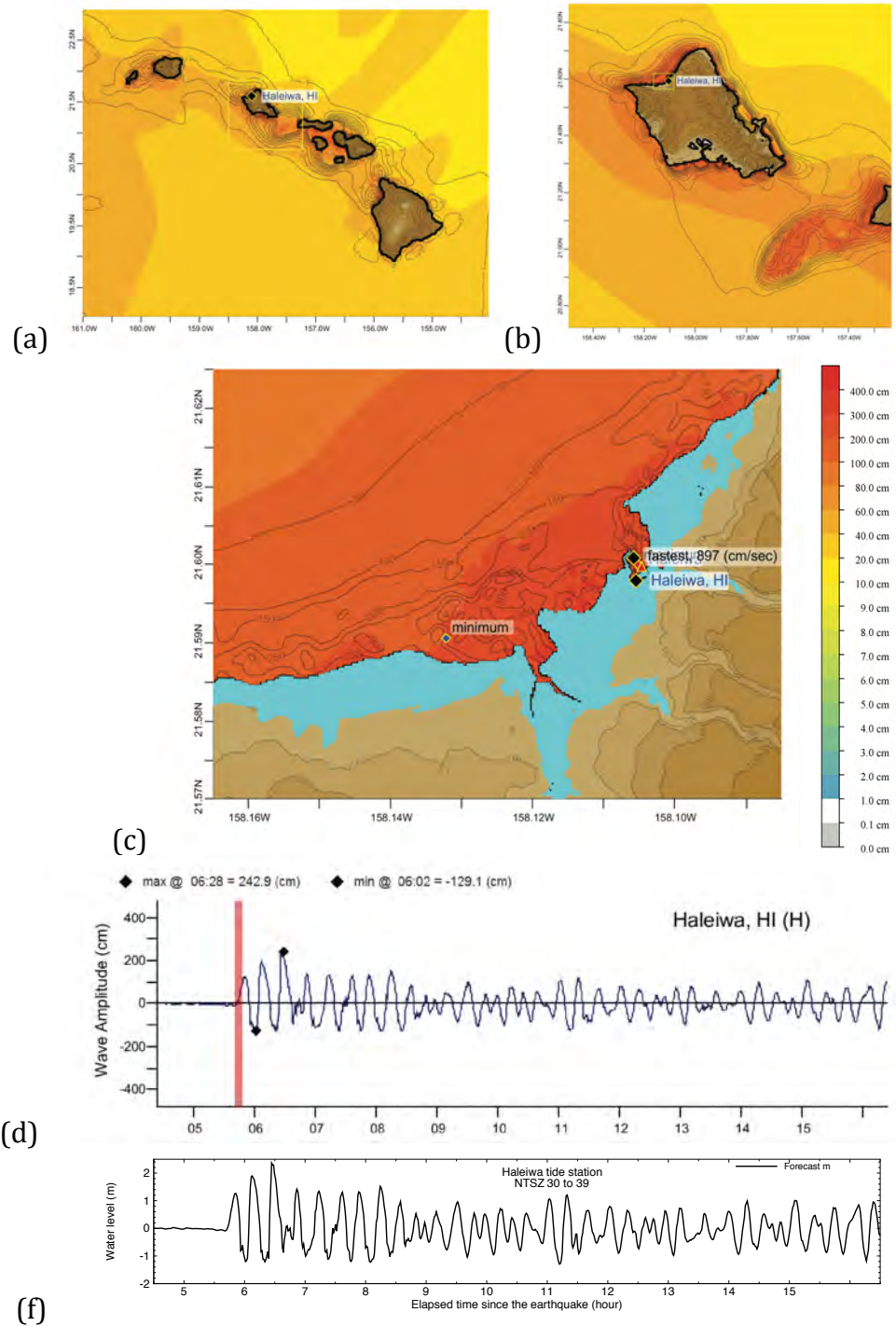


Figure 4. Response of the Haleiwa forecast model to synthetic scenario NTSZ 30-39 ($\alpha=30$). Maximum sea surface elevation for (a) A-grid, b) B-grid, c) C-grid. (d) Sea surface elevation time series at the C-grid warning point. (f) The result obtained during model development and is shown for comparison with test results.

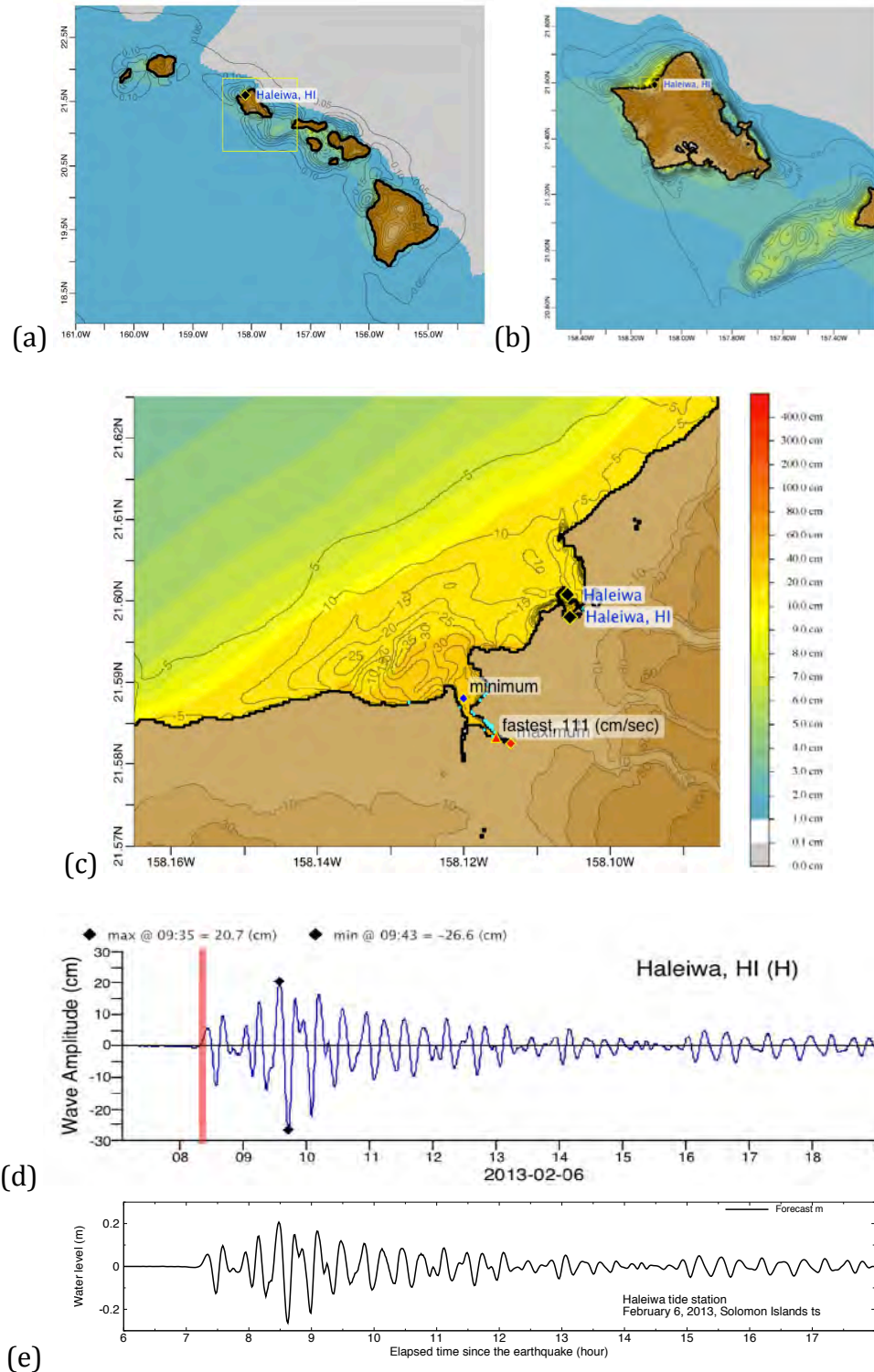


Figure 5. Response of the Haleiwa forecast model to the 2013 Solomon Islands tsunami. Maximum sea surface elevation for (a) A-grid, b) B-grid, c) C-grid. (d) Sea surface elevation time series at the C-grid warning point. (f) The result obtained during model development and is shown for comparison with test results.

Source Zone	Tsunami Source	α [m]	SIFT Max (cm)	Development Max (cm)	SIFT Min (cm)	Development Min (cm)
Mega-tsunami Scenarios						
Kamchatka-Yap-Mariana-Izu-Bonin	A22-A31, B22-B31	25	407.1	400.6	-127.2	-128..1
Aleutian-Alaska-Cascadia	A56-A65, B56-B65	25	226.5	220.7	-129.5	-117.6
Central and South America	A89-A98, B89-B98	25	106.0	105.2	-114.5	-111.3
New Zealand-Kermadec-Tonga	A30-A39, B30-B39	25	242.9	236.0	-129.1	-129.4
Historical Events						
New Britain-Solomons-Vanuatu			20.7	20.7	-26.6	-26.4

Table 1. Table of maximum and minimum amplitudes at Haleiwa, Hawaii warning point for synthetic and historical events tested using SIFT.